ABSTRACT

Title of dissertation: INFULUENCE OF POLYMER NANOPARTICLES ON THE DEWETTING OF POLYMER THIN FILMS

Hongxia Feng, Doctor of Philosophy, 2005

Dissertation directed by: Professor R. M. Briber
Department of Materials Science and Engineering

The influence of polystyrene star based nanoparticles on the dewetting of spun-cast linear polystyrene (PS) films on Si/SiOx surfaces is investigated as a function of temperature, concentration and type of the nanoparticles. The star polymers have polystyrene-benzocyclobutene copolymer arms which can undergo *intra*-molecular crosslinking to form relatively compact nanoparticles. The addition of a small amount of nanoparticles to linear PS thin films can suppress or enhance the dewetting of the films depending on the specifics of the star molecules. The suppression of dewetting in PS films by the nanoparticles is related to strong segregation of the nanoparticles to the polymer/silicon interface as observed by neutron reflection (NR) and atomic force microscopy (AFM). The stronger the segregation, the more effective the suppression of dewetting. Characterization of the hole morphology in the dewet films by AFM indicates there is a layer of polymer left behind on the Si substrate inside the hole which is consistent with the segregation layer observed by NR. Small angle neutron scattering showed that PS is miscible with the nanoparticles and no change in the surface energy was found by contact angle measurement at the polymer/air interface upon addition of nanoparticles. This suggests the segregation of nanoparticles to the Si surface is not due to immiscibility, or

surface energy changes. The segregation of the star polymers at the polymer/Si interface is driven by both an attraction between star molecules and the Si/SiOx surface and possibly a relatively small enthalpic penalty resulting from the unfavorable interactions between the star and linear molecules.

Further investigation on the effects of nanoparticle concentration on the dewetting behavior showed that the lower the concentration, the less effective the dewetting suppression. This suggests a critical coverage of nanoparticles is essential for effective suppression of dewetting.

INFULUENCE OF POLYMER NANOPARTICLES ON THE DEWETTING OF POLYMER THIN FILMS

By

Hongxia Feng

Thesis submitted to the Faculty of the Graduate School of the
University of Maryland, College Park in partial fulfillment
of the requirements for the degree of
Doctor of Philosophy
2005

Advisor Committee: Prof. Robert M. Briber
Dr. Ho-Cheol Kim
Prof. Mohamad Al-Sheikhly
Prof. Peter Kofinas
Prof. Srinivasa R. Raghavan
Prof. Timothy A. Barbari

DEDICATION

To my loving husband Xueli Sun, my lovely daughter Sophia Sun,

my dear mother, Shuyun Ma and Father, Shuhai Feng

for their endless encouragement

and everlasting love

ACKNOWLEDGEMENTS

First, I would like to express my sincere and deep gratitude to my academic advisor, Dr. Briber, for his patience, encouragement and valuable advice. I appreciate the opportunity he gave me to earn my Ph. D. degree.

I am also grateful to Dr. Mohammad Al-Sheikhly, Dr. Peter Kofinas, Dr. Srinivasa R. Raghavan, Dr. Timothy A. Barbari and Dr. Ho-Cheol Kim for serving on the advisory committee.

At last, I wish to thank Bani, Derek, and Young-Soo for their invaluable assistance in demonstrating Rheology and SANS procedures. My love and appreciation extend to my family and all the people who have given me any help throughout my thesis research and throughout of writing my thesis.

TABLE OF CONTENTS

LIST OF TABLES

LIST OF FIGURES

CHAPTER 1 INTRODUCTION

1.1 General background on polymers

Polymers are large molecules made up of repeated small molecules (termed monomers) connected by covalent bands.[1,2,3] The polymers can vary in their bonding, sequence of monomeric units and in their chain architecture.

1.1.1 Chain architecture

Polymers can be classified as linear, ring, branched, crosslinked, etc., based on the polymer chain architecture (Figure 1.1).

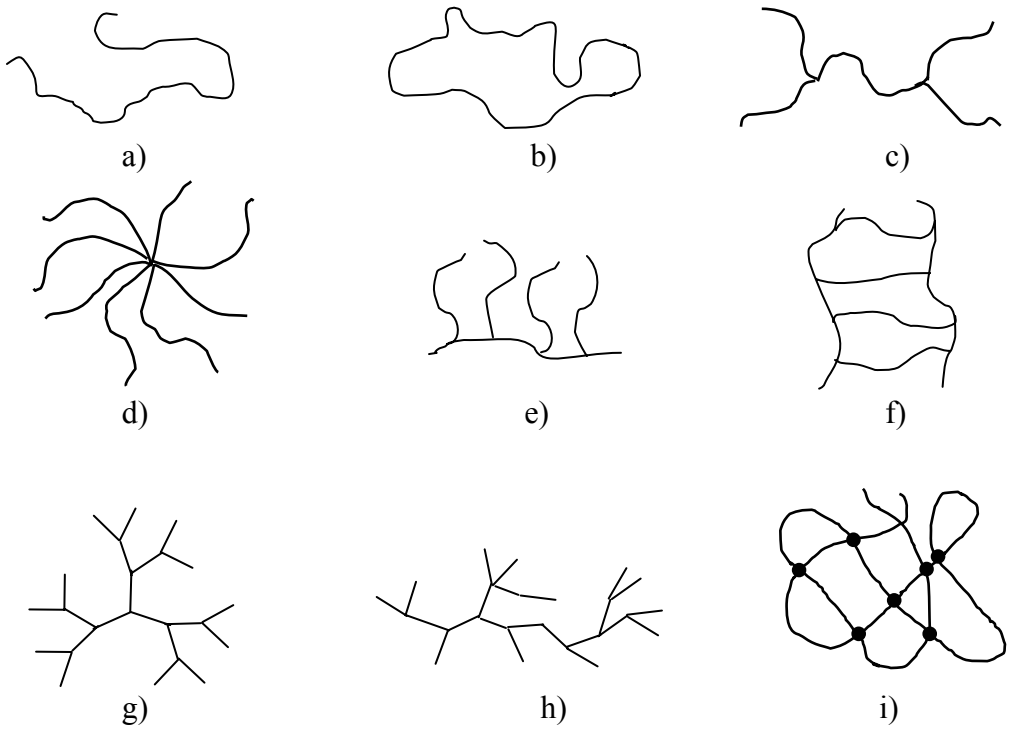

Figure 1.1. Schematic structure of a) linear; b) ring; c) H; d) star; e) comb; f) ladder; g) dendrimer; h) highly branched; i) crosslinked polymer with the dots indicating crosslinks.

A linear polymer is one in which every repeating unit is linked to two other monomers, it may be represented by a chain with two ends. A ring polymer is one in which each repeating unit is linked only to two others with no ends.

Branched polymers include star branched, H-branched, comb, ladder, dendrimer, or randomly branched as sketched in Figure 1.1. They are molecules in which the repeating units are not linked simply in a linear manner, either because at least one of the monomers has functionality greater than two or because the polymerization process itself produces branching points in a polymer that is made from exclusively bifunctional monomers. Special class of branched polymers, which have controlled architectures such as dendrimers, hyperbranched polymers, and star polymers have been developed in recent years[4,5,6]. Many properties of branched polymers are inherently different than their linear polymer analogs and it is this architectural difference that leads to many of the observed changes in their physical properties. For example, the viscosity-molecular weight relation of branched polymers is different from linear chains; branched polymers have a significantly lower viscosity than linear polymers of the same molecular weight[4,5,6]. Crosslinked polymers are interconnected branch polymers through junction points termed as a crosslink. They are characterized by the molecular weight of chains between crosslinked points or the crosslink density, which is the number of junction points per unit volume. Unlike linear chains and branched polymers, crosslinked polymers do not dissolve in a solvent, although they can swell considerably depending on the crosslink density and solvent quality.

1.1.2 Thermodynamics of polymer solutions and mixtures

The most widely used theory to describe the thermodynamic properties of polymer solutions and blends is the Flory-Huggins theory which is formulated in terms of a lattice model.[7] This theory represents a mean field approximation to this lattice model and the thermodynamics of polymer solutions is described by a three dimensional lattice consisting of identical cells. Monomers and solvent molecules each occupy one lattice site and a polymer consists of a chain of adjacent monomers. The chain connectivity precludes the random mixing of the polymer chain segments and solvent molecules. The Flory-Huggins theory is modified relative to the regular solution theory of low molecular weight molecules due to the chain connectivity of the polymers.

For a regular solution which is a mixture of small molecules, the free energy of mixing per volume is given by Hildebrand: [8]

$$\frac{\Delta F}{kT} = X_1 \ln X_1 + X_2 \ln X_2 + \frac{X_1 X_2 \Delta\varepsilon}{kT} \qquad \text{eq. 1.1}$$

Where X_1 and X_2 are the molar fraction of species 1 and species 2, respectively. The molar fraction of species 1 and 2 are given by $X_1 = \frac{n_1}{n_1 + n_2}$ and $X_2 = \frac{n_2}{n_1 + n_2}$, where n_1 and n_2 are number of moles of species 1 and species 2, respectively. The interaction energy is $\Delta\varepsilon = -z\left[\varepsilon_{12} - \frac{1}{2}\left(\varepsilon_{11} + \varepsilon_{22}\right)\right]$, where ε_{ij} is energy of a i-j monomer contact and z is the coordinate number of the lattice.

For a mixture of solvent and polymer the free energy of mixing per volume is given by

$\frac{\Delta F}{kT} = \phi_1 \ln \phi_1 + \frac{\phi_2 \ln \phi_2}{N_2} + \frac{\phi_1 \phi_2 \Delta \varepsilon}{kT}$, where ϕ_i is the volume fraction of species i and N_2 is the degree of polymerization of species 2 which corresponds to the length of polymer chain. The factor $1/N_2$ in the second term of equation 1.1 is due to the connectivity of polymer chain. The volume fraction is given by $\phi_1 = \frac{n_1}{n_1 + n_2 N_2}$ and $\phi_2 = \frac{n_2 N_2}{n_1 + n_2 N_2}$.

For a mixture of two polymers the entropy of mixing per volume is given by:

$$\Delta s_{mix} = \frac{\Delta S_{mix}}{n_T} = -k\left(\frac{\phi_1 \ln \phi_1}{N_1} + \frac{\phi_2 \ln \phi_2}{N_2} \right) \qquad \text{eq. 1.2}$$

where n_T is the total number of moles. The enthalpy of mixing per volume is then given by:

$$\Delta h_{mix} = \frac{\Delta H_{mix}}{n_T} = \phi_1 \phi_2 \Delta \varepsilon \qquad \text{eq. 1.3}$$

By combining equation 1.2 and equation 1.3 the free energy of mixing per volume is given by:

$$\frac{\Delta F}{kT} = \frac{\phi_1 \ln \phi_1}{N_1} + \frac{\phi_2 \ln \phi_2}{N_2} + \frac{\phi_1 \phi_2 \Delta \varepsilon}{kT} \qquad \text{eq.1.4}$$

where $\phi_1 = \frac{n_1 N_1}{n_1 N_1 + n_2 N_2}$ and $\phi_2 = \frac{n_2 N_2}{n_1 N_1 + n_2 N_2}$.

The factors of $1/N_1$ and $1/N_2$ are inserted into equation 1.4 due to the connectivity of polymer chains. This effect of connectivity lowers the entropy of mixing. Since the free energy of mixing generally has a positive value, most polymer blends are immiscible.

The Flory-Huggins interaction parameter is defined as:

$$\chi_{12} = -\frac{z}{kT}\left(\varepsilon_{12} - \frac{1}{2}\left(\varepsilon_{11} + \varepsilon_{12} \right) \right) = \frac{\Delta \varepsilon}{kT}.$$

The stability of a mixed phase is assured only when the second derivative of the free energy with respect to composition is positive. For unfavorable polymer-polymer interactions (i.e., positive values of χ_{12}), instability or phase separation will occur when N_1 and N_2 are increased to a certain critical value. In the limit that N_1, N_2 are infinity, miscibility only exists when the polymer-polymer interactions are favorable (i.e, $\chi_{12} < 0$). If χ_{12} equals zero the polymer blends favors mixing which is termed ideal athermal mixing.

1.1.3 Chain conformation and radius of gyration

Flexible polymers are randomly coiled and entangled with their neighbors. The dimension and conformation of a polymer in solution varies with solvent quality and temperature. In a good solvent the polymer chain expands and has a larger radius of gyration in comparison with a chain in a theta or poor solvent. Two separated chain segments can not occupy the same space and each segment exists within a volume from which all other segments are excluded. This volume is termed the excluded volume and depends on solvent quality and temperature. The chain conformation of a polymer in a good solvent can be studied using a model of a 'self avoiding walk'. In general attractive and repulsive forces compensate as the solvent quality decreases and at some points the excluded volume vanishes. Under these conditions the solvent is called a theta (θ) solvent and this condition is termed the theta condition. In a theta solvent the polymer chain behaves ideally and obeys Gaussian statistics. If polymer-polymer contacts are favored the polymer chain shrinks and the solvent is termed a poor solvent.

The dimensions of linear chains can be characterized by the radius of gyration (Rg). Rg is defined as the mass weighted root mean square (rms) average of the magnitudes of the

vectors leading from the center of mass to the mass of points making up the object in question. The radius of gyration of Gaussian polymer chain is given by[9,10]

$$R_g^{\,2} = \frac{Nl^2}{6} \qquad \text{eq. 1.5}$$

Where l is the length per monomer and N is the number of monomers in the chain. In the general case, the dimension l is not the exact length of the monomer (or bond length) but an effective step length (termed the statistical segment length) per monomer, which is often larger than the actual molecular length. The advantage of radius of gyration (as opposed to the end-to-end length is that it can be also used to characterize the dimensions of branched polymers.

1.2 General background on small angle neutron scattering and neutron reflectivity

Small angle neutron scattering (SANS) and neutron reflectivity (NR) are non-destructive techniques for studying the structure of materials. Using neutrons as scattered radiation also has the advantage of different isotopes having significantly different scattering cross sections allowing the use of the isotopic substitution (ex. deuterium for hydrogen) to enhance contrast.

1.2.1 Properties of neutron radiation

A neutron is an uncharged elementary particle, possessing a mass m equal to 1.675×10^{-24} g and spin ½. Neutrons also exhibit wave like behavior. There are two means of producing neutrons in sufficient quantities for experiments. One is a nuclear reactor which produces neutrons by the fission of Uranium-235. The other approach to neutron production is that used in *spallation* neutron sources. These use particle accelerators to generate an intense high-energy proton beam which is directed at a target composed of heavy nuclei (tungsten, uranium). Provided that the protons have sufficient kinetic energy

they are able to overcome the intrinsic long-range electrostatic and short-range nuclear forces they encounter and effectively blast the target nuclei apart.[11,12]

The most fundamental difference between neutron and electromagnetic radiation is the mechanism by which the incident radiation interacts with matter. Light and X-rays are both scattered by the electrons surrounding the nuclei, but neutrons are scattered by the nucleus itself. This fact has several important consequences. Because atomic nuclei are 10^4-10^6 times smaller than typical neutron wavelengths, the nuclei effectively act as point scatterers. This means the scattering is spherically symmetric.

In addition, the interaction of neutrons with matter is weak and the absorption of neutrons by most materials is correspondingly small. Neutron radiation is therefore very penetrating. It can be used to probe the bulk properties of samples with path lengths of several centimeters. The neutron also has a small magnetic moment; this can interact with the spin and orbital magnetic moments present in a sample containing atoms with unpaired electrons, giving rise to an additional scattering mechanism.

1.2.2 Small angle neutron scattering

Since neutron radiation can be produced to cover a range of wavelengths (0.01-3 nm) and the radius of gyration of a polymer in solution is usually 1-10 nm, SANS is very useful in polymer science.

1.2.2.1 SANS Theory

The objective of a SANS experiment is to determine the differential cross-section, $(\partial\Sigma/\partial\Omega)(q)$, the probability that a photon or a neutron impinging on the sample is scattered into a unit solid angle in the given direction. The differential cross-section is given by:

$$\frac{I(q)}{V} = \frac{d\Sigma}{d\Omega}(q) = \frac{1}{V} k_n P(q) S(q) + B_{inc} \qquad \text{eq. 1.6}$$

where k_n is the contrast factor for neutrons, $P(q)$ is a function known as the form or shape factor, $S(q)$ is the interparticle structure factor, q is the scattering vector and B_{inc} is the (isotropic) incoherent background signal. $(\partial\Sigma/\partial\Omega)(q)$ has dimensions of length^{-1} and is normally expressed in units of cm^{-1}.

Scattering length of a single nucleus

The value of the scattering length is independent of the wavelength incident neutrons. For a particular nucleus it depends on the spin state of the of the nucleus-neutron system. The strength of the neutron-nucleus interaction varies irregularly with Z; not even isotopes of the same element have the same neutron scattering cross-section, s. A selection of neutron scattering cross-sections, s and neutron scattering lengths, b of interest to polymeric samples are given in Table 1[13], where natural isotopic abundance is assumed. The scattering cross-section and scattering length are related by $s = 4\pi b^2$.

Table 1.1. Selection of neutron scattering cross-sections (s) and neutron scattering lengths (b) of interest to polymeric samples

Atomic Nucleus	b_{coh}(fm)	s_{coh}(barns)	s_{inc}(barns)
^{1}H	- 3.74	1.8	80.26
^{2}D	+ 6.67	5.6	2.0
O	+ 5.80	4.2	0.0
Si	+ 0.415	2.2	0.0

An important isotopic variation occurs when Z = 1. Hydrogen has a s_{coh} of 1.8 barns which is roughly the same as that of manganese. On the other hand, for deuterium s_{coh} = 5.6 barns, similar to the value for carbon-12. Thus, and unlike X-rays, not only can neutrons "see" hydrogen isotopes, but they can differentiate between them.

The scattering vector

The scattering vector q is the modulus of the diffrence between the incident, k_i, and scattered, k_s, wavevectors, see Figure 1.2, and is given by:

$$q = /q/ = /k_f - k_i/ = 4\pi\sin\theta/\lambda \qquad \text{eq. 1.7}$$

where q has dimensions of $(\text{length})^{-1}$.

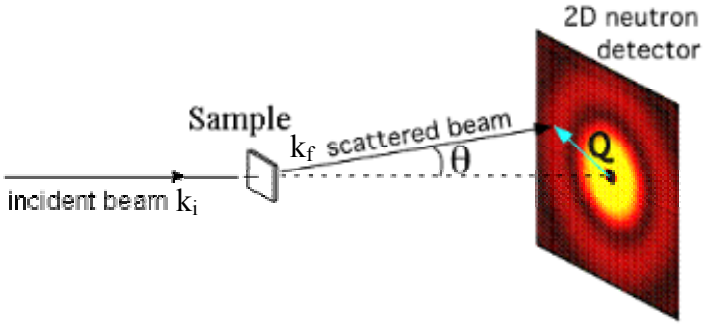

Figure 1.2. Schematic of the small angle scattering geometry

Substituting Equation 6 into Bragg's law of diffraction $\lambda=2d\sin\theta$ yields a useful expression:

$$d=2\pi/q \qquad \text{eq. 1.8}$$

where d is a distance. Through Equations 1.7 and 1.8 it is possible to both configure an instrument (i.e., determining the desired "q-range") and to quickly and rapidly "size" the scattering bodies in a sample from the position of any diffraction peak in q-space.

The contrast term

The neutron scattering length density, (b/v) of a molecule of i atoms may be readily calculated from the expression:

$$\rho = \Sigma_i b_i \cdot \frac{DN_A}{M_w}$$

where D is the bulk density of the scattering molecule and M_w is its molecular weight, N_A is Avogadro constant, b_i is the scattering length of the element. ρ has dimensions of $(\text{length})^{-2}$ and can also be negative.

The contrast factor k_n is defined as $N_A[(\rho_a - \rho_b]^2$ where ρ_a and ρ_b are the scattering length density of the molecule of interest and that of the medium respectively and N_A is Avogadro's number. A selection of neutron scattering length densities for the fully hydrogenated and deuterated forms of common solvents and polymers and some common substrates are shown in Table 1.2.

Table 1.2. Selection of neutron scattering length densities

ρ,10^{10}cm^{-2}							
Solvent	D-form	H-form	Polymer	D-form	H-form	Substrate	
Cyclohexane	- 0.28	+ 6.70	PS	+ 1.42	+ 6.42	Silicon	+ 2.07
Toluene	+ 0.94	+ 5.66	PEO	+ 0.64	+ 6.46	SiO_2	+ 3.15

The form and structure factor

The form factor is a function that describes how $(\partial\Sigma/\partial\Omega)(q)$ is modulated by interference effects between radiation scattered by different parts of the same scattering body. Consequently it is dependent on the shape of the scattering body. Expressions for some common shapes are listed in Table 1.3[12].

Table 1.3. Selections of form factors

Shape	Form factor, P(q)
Sphere of radius R	$\frac{9(\sin qR - qR\cos qR)^2}{(qR)^6}$
Gaussian random coil with radius of gyration R_g, monodisperse and	$x = \frac{2(e^{-x} + x - 1)}{x^2}$

The interparticle structure factor is a function that describes how $(\partial\sigma/\partial\Omega)(q)$ is modulated by interference effects between radiation scattered by different scattering bodies. Consequently it is dependent on the degree of local order in the sample. As the concentration of scattering bodies becomes very dilute $S(q) \rightarrow 1$, the scattering does not depend on the structure factor.

1.2.2.2 SANS equipments used in this thesis

All experiments in this thesis were done on the NIST Center for Neutron Research NG3 or NG7 instruments. The schematic diagrams of NIST NG3 and NG7 are shown in Figure 1.3 & 1.4 respectively. The characteristics of NG3 and NG7 are listed below:

- Source: neutron guide (NG3), 60 mm × 60 mm
- Monochromator: mechanical velocity selector with variable speed and pitch
- Wavelength range: 0.5 nm-2.0 nm
- Wavelength resolution: 10%-30% (FWHM)
- Source to sample distance.: 4 m to 16 m in steps via insertion of neutron guide sections
- Sample to detector distance.: 1.3 m to 13 m
- Collimation: circular pinhole collimation
- Sample size: 0 to 25 mm diameter
- q range: 0.015 nm^{-1} to 6 nm^{-1}
- Detector: 650 mm × 650 mm ^{3}He position-sensitive proportional counters (5 mm resolution.)

NG7 has undergone a number of improvements over the years to remain, along with its near-twin on guide NG3, the best such instruments in the U.S. The improvements, including a higher resolution 2D detector and focusing refractive lenses, have extended

the q-range of the instrument which now goes from 0.008 nm^{-1} to 7.0 nm^{-1} to enable structural features in materials ranging from roughly 1 nm to over 500 nm to be probed.

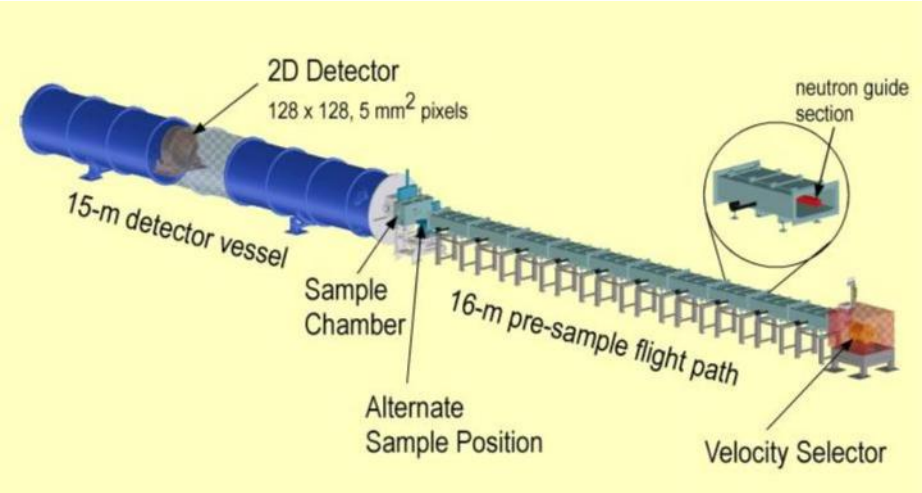

Figure 1.3. Schmetic of the NIST Center for Neutron Research 30 m SANS instrument at NG7 (http://www.ncnr.nist.gov/instruments/ng7sans/)

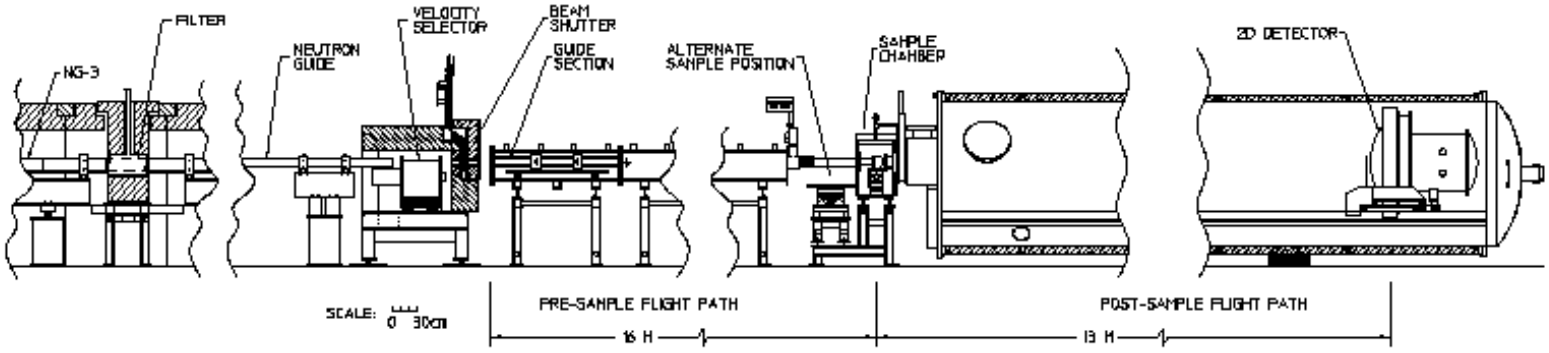

Figure 1.4 Schmetic of the NIST Center for Neutron Research 30 m SANS instrument at NG3 (http://www.ncnr.nist.gov/instruments/ng3ans/)

1.2.3 Neutron reflectivity

Neutron reflection is another technique and is also of particular importance for polymer systems. Specifically, it probes the neutron scattering density at depths of up to several thousand Å, with an effective depth resolution of a few Å. What is measured is the profile of reflectivity as a function of angle beyond the critical angle for total external reflection. The sample must thus present a smooth, flat surface, preferably several cm^2 in area. The method is extensively used for studies of polymer surfaces, Langmuir-Blodgett films, and thin films and multilayers of metals and semiconductors, both magnetic and non-magnetic.

The variation of neutron refractive index normal to a reflecting surface governs the reflection of neutrons by surfaces and interfaces. The neutron refractive index is related to the scattering length density through this equation:

$$\nu = 1 - \lambda^2\left(\frac{\rho_b}{2\pi}\right) + i\lambda\left(\frac{\rho_a}{2\pi}\right) \qquad \text{eq. 1.9}$$

ρ_b and ρ_a are the scattering length density (i.e. the average scattering length per unit volume) and the absorption cross section density (with a similar definition) respectively. For most polymeric materials, ρ_a is negligibly small so that the last term in eq. 1.9 can be dropped.

The neutron reflection technique exploits the same interference phenomenon as reflection of light from films of oil-on-water, but with the much smaller distance scale arising from the smaller neutron wavelength, and with the potential of manipulating ν by varying ρ_b through deuteration. The manipulation of the neutron refractive index by hydrogen-deuterium isotopic substitution is a key feature of the technique.

In neutron reflection experiments a monochromated (and possibly polarized) beam of neutrons is focused onto a plane sample on a substrate and the reflected intensity of neutrons is measured as a function of momentum transfer (Figure 1.4). Reflectivity falls off at a least q^{-4} according to Fresnel's law and even faster for an imperfect surface. For a thin film, interference from the different interfaces results in an oscillatory peaks (corresponding to Bragg reflection of different orders) in the reflectivity (see Figure 1.5) superimposed upon the q^4 decay. The damping of these interference fringes and the decay of the pattern with increasing q are affected by the interfacial roughness.[14]

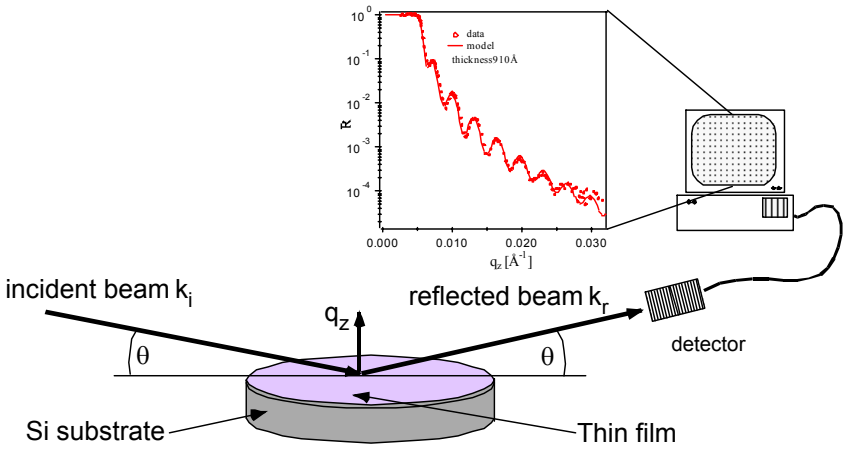

Figure 1.5. Schematic of the neutron reflectivity geometry

The layer thickness that can be observed has a maximum limit, due to instrument resolution, of typically 20-4000Å. The minimum thickness is limited by the maximum Q value that can be measured. It depends on count rate, background. The experimentally determined absolute scaling is obtained by normalization to the straight through beam intensity (used mostly for the liquid-solid interfacial studies), by reference to the region of total reflection (used predominantly for solid films) or by normalization to a standard surface such as D_20.

A schematic diagram of NIST NG7 reflectometer is shown in Figure 1.6[15].

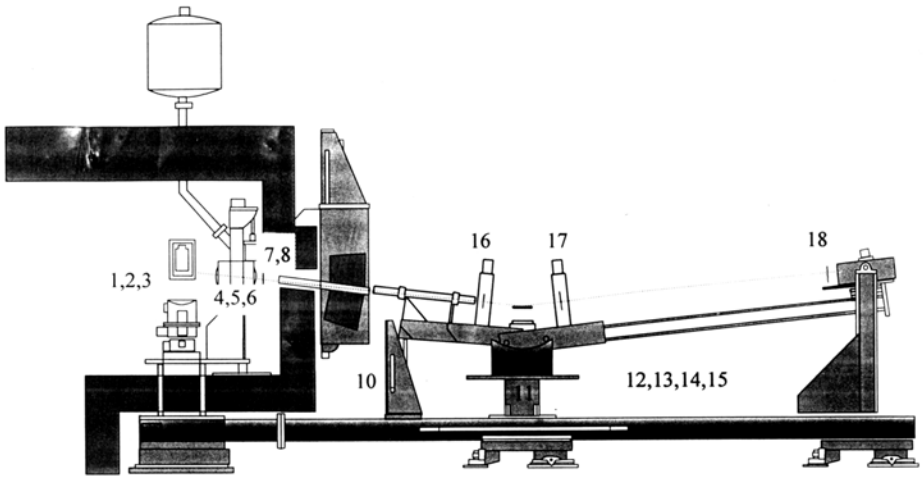

Motor	Function	Remarks
1	Monochromator θ	Do not move
2	Monochromator tilt	Moved only during scan
3	Monochromator translation	Do not move
4	Graphite filter tilt	Do not move
5	Be filter translation	Moved only during scan
6	Graphite filter translation	Do not move
7	Slit 1 translation	Moved only during scan
8	Slit 1 opening	Adjustable, moved during scan
9	Shielding translation	Moved only during scan
10	Flight tube arm translation	Moved only during scan
11	Main elevator	Moved only during scan
12	Independent sample elevator	Adjustable
13	Sample tilt	Adjustable
14	Sample χ	Adjustable
15	Sample translation	Adjustable
16	Slit 2 opening	Adjustable, moved during scan
17	Slit 3 opening	Adjustable, moved during scan
18	Slit 4 opening	Adjustable, moved during scan

Figure 1.6. Schematic of the neutron reflectivity at the NIST Center for Neutron Research

The reflectometer has Pyrolytic graphite monochromator giving an effective wavelength range of 0.235, 0.407, 0.47, and 0.55 nm with wavelength resolution of 2.5% $\Delta\lambda/\lambda$. The other characteristics of NIST NG7 reflectometer are:

- Beam size (continuously variable): 0.05 × 50 mm to 4 × 50 mm
- q range: 0.03 to 4 nm^{-1}
- q resolution: Variable with slits from 0.02 to 0.15 $\Delta q/q$
- Monochromator to sample distance: 2 m
- Sample to detector distance for reflectivity detector: 2 m

1.3 General background on dewetting of thin films

The process by which an initially uniform film of a liquid on a nonwetting substrate breaks up into droplets is known as dewetting. Much experimental and theoretical work has been done to study of the kinetics of dewetting because of the importance of thin films in technology. Much of this work has involved polymer films, both because they are increasingly being used in technological applications involving dielectric coatings, resist layers for lithography, electronic packaging, optical coatings, nonlinear optical devices, lubricating surfaces, etc. and because their high viscosity enables experiments carried out on convenient time scales.

While thick polymer films (greater than micrometers) on inorganic substrates may be stable or metastable due to gravity[16], in thin films specially for films which approach molecular dimensions, intermolecular forces start to govern the system[17]. Producing stable and defect-free films is particularly problematic in very thin films (thickness, L~10 nm) where thermally induced fluctuations of the polymer-air film boundary ("capillary waves") tends to cause film rupture.

1.3.1 Theory of stability of thin liquid films

For a droplet in equilibrium on a solid surface, the equilibrium angle θ is given by the Young's equation: $\gamma_{lv}\cos\theta = \gamma_{sv} - \gamma_{ls}$, where γ is the surface free energy and subscripts v, l, and s stands for gas, liquid and solid, respectively. When $S = \sigma_{sv} - \sigma_{ls} - \sigma_{lv}$ is positive a thermodynamic wetting angle cannot be achieved, the traditional theory concludes that the liquid spreads over the surface of the solid and if the surface of the solid is sufficient large, the spreading leads to a submonolayer. However, all the above quantities imply a macroscopic system to which the traditional thermodynamics can be applied.

For films which approach molecular dimensions, intermolecular forces govern the system. The stability of thin liquid films and subsequent dewetting processes have already been investigated extensively, both theoretically[18] and experimentally[19,20]. In general, film stability is determined by the balance of the free energy per unit area of the film of thickness h, $F(h) = \gamma_{sl} + \gamma_{lv} + \Delta G(h)$, with γ_{sl}, γ_{lv}, being the solid/liquid and liquid/vapor interfacial energies and ΔG(h) is the contribution of the long-range forces which is also called the excess intermolecular interaction free energy (ΔG).[21] For a van der Waals (vdW) liquid in air[22], $\Delta G(h) = -A_{eff}/12\pi h^2$ determined by the effective Hamaker constant, A_{eff}. A negative effective Hamaker constant A signifies a long range apolar van der Waals repulsion which promotes film stability and wetting. However, it must be emphasized that many other components may enter into ΔG(h) at small thicknesses: dipole-dipole, hydrogen bonds etc. Reiter et al. consider a fairly general excess intermolecular interaction free energy (ΔG) composed of long (attractive/repulsive) and relatively short-range interactions, which decay with the local

thickness, h, $\Delta G(h) = \frac{-A}{12\pi h^2} + S^P e^{\frac{-h}{l}}$.[23,24] Here, A is the Hamaker constant, S^P is the polar component of the spreading coefficient S representing short-range polar interactions, and ℓ is the decay length characterizing the range of these interactions. For small thickness $\Delta G(h \to 0) = S = \gamma_{sv} - \gamma_{sl} - \gamma_{lv}$ .Three cases are discussed by Sharma[24] as shown in Figure 1.7.

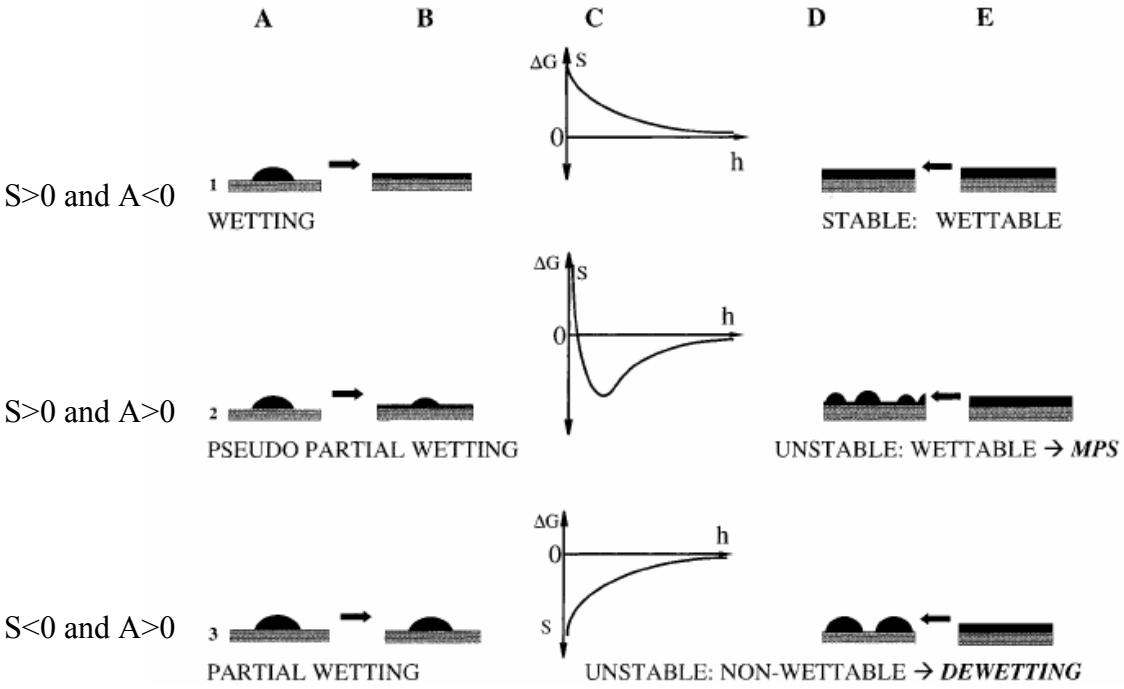

Figure 1.7. Schematic drawing of different possible interactions of a liquid with a solid and its relation to drop spreading and thin film stability. Based on a particular interaction potential C, B and D give the equilibrium state after initial situations A and E, respectively; A describes a drop of finite volume placed on the solid, after possible initial fast relaxations due to the deposition; B reflects the final equilibrium state, on a finite solid surface; C is the thickness (h) variation of the excess free energy (ΔG) of the system with a spreading parameter S=ΔG(h) at h=0; E stands for a thin film forced to spread uniformly on the substrate; and finally, D gives the possible final patterns after relaxation towards equilibrium.

Case 1 is for complete spreading/ wetting for a positive spreading parameter S and purely repulsive interaction forces. In case 2, long-range attractive forces are overcompensated by repulsive short-range interactions near the substrate with an absolute minimum at a finite distance from the substrate, which results in pseudo-partial wetting (A to B) and morphological phase separation (MPS) (E to D) for drops and thin films above a critical thickness, respectively. In case 3, a drop never spreads, and thin films of all thicknesses are intrinsically unstable leading to true dewetting because of purely attractive forces.

London-van der Waals Force and Hamaker constants

The origin of the London-van der Waals force in nature lies in the instantaneous dipole generated by the fluctuation of electron cloud surrounding the nucleus of electronically neutral atoms. Since they are always attractive it seems that long-range van der Waals forces should not cause a film to break up. However if the attractive interaction between a film and surrounding medium is weaker than the substrate and the surrounding medium, then the film will break up.

The interaction energy between two planar surfaces 1 & 2 in the presence of medium 3 (Figure 1.8) is $W_{vdW} = -\frac{A_{132}}{12\pi h^2}$ where h is the distance between the two surfaces; A_{132} is the Hamaker constant for substances "1" and "2" in presence of medium "3"[17].

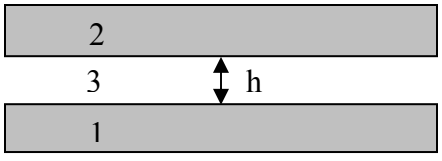

Figure 1.8. Schematic of a two planar surfaces at a separation distance of h.

For contact of two dissimilar materials in the presence of a third media, the effective Hamaker constant[17]:

$$A_{132} \cong \left(\sqrt{A_{11}} - \sqrt{A_{33}}\right)\left(\sqrt{A_{22}} - \sqrt{A_{33}}\right) \qquad \text{eq. 1.10}$$

For a Si/PS/Air system, a negative effective Hamaker constant is reported[20]. However, accurate determination of the Hamaker constant is difficult for our system, Si/SiO/PS/air. We simplify our system to Si/SiO/Polystyrene/Vacuum, Hamaker constants for p-doped Si wafers are unavailable; in this case we use the typical value for Si. Using quoted values[25,26,27] of 5.2 and 6.5 (in units of 10^{-20} J) for the Hamaker constant of the silicon and silica layer, respectively, an estimate of the non-retarded Hamaker constant of the substrate Si/SiO is obtained from the geometric mean rule[17] as 5.8×10^{-20} J. Based on Lifshitz theory which relates the Hamaker constant to dielectric constants of the materials, $A_{33} = \frac{3}{4\pi} h\varpi_{33}$ (where h is plank constant and ϖ is the averaged angular frequency), A_{33} are calculated as 0.73×10^{-19} J with $h\varpi_{PS\text{-}PS}$ of 1.91 eV in vacuum.[28] Since A_{22} is approximately zero, an approximate value of the effective Hamaker constant of our multilayered system (Si/SiO)/Polystyrene/Air is:

$A_{132} = -\sqrt{A_{33}}\left(\sqrt{A_{11}} - \sqrt{A_{33}}\right) = -\sqrt{0.73}\left(\sqrt{0.58} - \sqrt{0.73}\right)\times10^{-19}\,\text{J} = 0.79\times10^{-20}\,\text{J}$. This is consistent with the Hamaker constant of SiO/PS/air found by Israelachvili[17] and Seemann[29] which is also a positive value (~2×10^{-20} J).

1.3.2 Dewetting mechanisms

In the past 10 years, the dewetting of polymer thin films has been investigated intensively; the dewetting kinetics related to substrate, film thickness as well as other factors were thoroughly reviewed in two papers[30,31]. Spinodal and nucleation dewetting

are considered to be two important mechanisms of dewetting of thin polymer films on solid substrates.

Spinodal dewetting

Spinodal dewetting is an intrinsic mechanism leading to film rupture involving amplification of capillary waves by thermal fluctuations, due to the vdW instability[21]. For this mechanism the term "spinodal dewetting" has been coined in analogy to phase separation involved in composition decomposition process[32], where height fluctuations in dewetting corresponds to the composition fluctuation in phase separation.

A thin film represents a system of two parallel interfaces, these interfaces know about their mutual existence, at such large separations, only via long-range interactions such as London-van der Waals force. The dispersive forces driving the dewetting are counterbalanced by the inherent energy cost having a large interface. As a result of the competition between these two terms, a dominant wavelength ℓ emerges, which grows faster than any other unstable wavelength.[33] The spatial-temporal fluctuations of the film thickness was given by: [32,33, 34]

$$Z(\mathrm{x,t}) = h + ue^{iqx}e^{(-t/\tau)} \qquad \text{eq. 1.11}$$

With amplitude u, wave number q, time t, and relaxation time τ and where x is a coordinate parallel to the surface. Eventually the roughening leads to rupturing of the initially smooth and continuous films, at the point where the undulations grow sufficiently to expose the underlying substrate. Films are, however, stable to thickness fluctuations below a critical wavelength, given by $\ell/2$. Should the polymer film be confined to an area smaller than the dominant wavelength, then the spinodal dewetting is suppressed.[35]

For a solid substrate (S), supporting a thin liquid film (F) in an environment (E), eq.1 predicts the time growth of a critical wave vector q_c(wavelength q_c^{-1}), which determines an h^{-4}dependence of the initial hole density, N_i, in the spontaneously dewetting film[32,33,34,36] $N_i(h) \sim q_c^2 \sim h^{-4}$

Nucleation dewetting

Another way a film might break up is by nucleation and growth of holes. The nucleation mechanism considers the dewetting phenomena induced either by defects (contamination, etc) in polymer film, by defects on the solid surface or by thermal fluctuations of the polymer surface. The presence of debris particles or impurities can lower the energy barrier leading to film thinning and holes appear in the film at the sites of particles (which are normally randomly distributed).[37,38] Nucleation dewetting is by far the most common.[39]

Figure 1.9 shows the typical dewetting process in polymer thin films.[19] Dewetting begins with the nucleation of holes in the film followed by the growth of these holes. A narrow size distribution of holes is typically observed. As the holes continue to grow, they impinge on each other forming a ribbon of material between them. Complete dewetting results in the formation of Vornoi patterns composed of liquid droplets. This pattern is formed by the coalescence of the holes followed by breakup of the ribbons into isolated droplets (Figure 1.9).

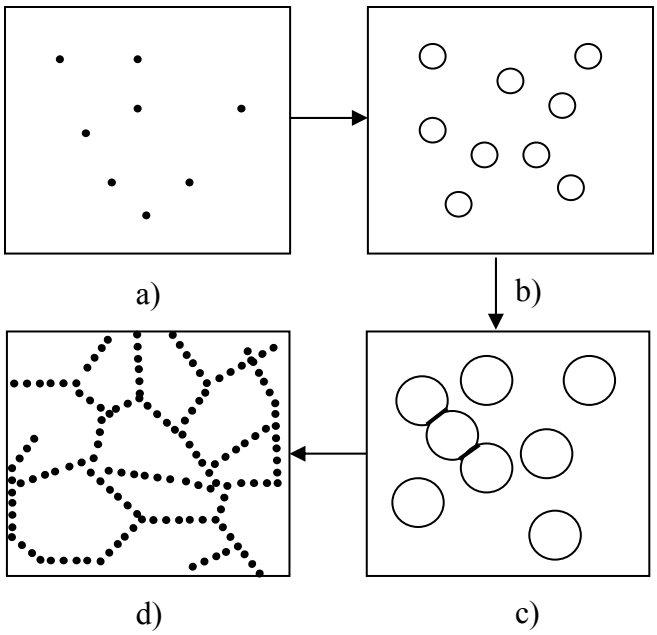

Figure 1.9. Schematic showing the stages of dewetting of a thin liquid film. Dewetting begins with the nucleation of dry patches or holes in the film (a), followed by the growth of these holes (b). A narrow size distribution of holes is typically observed. As the holes continue to grow, they impinge on each other forming a ribbon of material between them. (c). Complete dewetting (d) results in the formation of Voronoi pattern composed of liquid droplets.

Redon et al.[19] has studied the dewetting of poly(dimethylai1oxane) films by nucleation on silanized silicon wafers. They found: (i) in thick films (that is, for film thicknesses, ex., larger than 10 μm), holes open at constant velocity. The radius of the dry patch, R, grows linearly with time, t. (ii) In microscopic films (ex., < 1 μm), R(t) follows $t^{2/3}$ due to a slippage of the polymer chains on the solid surface.

For thin film (ex., <100nm), Brochard-Wyart et al found that if the deformation in the film is assumed to be elastic and the viscous dissipation at the film/substrate interface is negligible, then the radius of the hole should increase as $R(t) = R_0 e^{t/\tau}$, where τ is a function of the film thickness h, S and the viscosity, η.[40] In other theoretical work by Brochard-Wyart et al[18], they found a dry patch should first grow with a radius of $R(t) \propto$

$t^{2/3}$ in a strong slippage regime. This approximation is applicable for very thin liquid "substrate" films or when the substrate is smooth and passive so that the polymers melt slips at the substrate surface. When the size *R* exceeds a critical value, R_c, a nonslip regime occurs and the radius of holes grow linearly with time, t, $R \propto t$.

However, in the dewetting process the energy is dissipated partly by the friction at the substrate and partly by viscous dissipation within the rim, therefore the two limiting cases of full slip and no-slip may need to be considered at the same time. Jacobs et al.[41] combined the two limiting expressions in one equation that accounts for both viscous dissipation in the rim and slippage at the interface at all stages of hole growth (eq. 1.9).

$$t(R) = \frac{K_\upsilon}{S}\left(R - 2\gamma\sqrt{R} + 2\gamma^2 \ln\left(1 + \frac{\sqrt{R}}{\gamma}\right)\right) + \tau_0 \qquad \text{eq. 1.12}$$

Where K_v is the viscous dissipation constant, that express an effective viscosity taking into account a geometric factor dependent on the contact angle at the three phase contact line; and $\gamma = K_v/K_s$, where K_s is the slippage constant, directly proportional to the friction coefficient. The two limiting cases considered by Brochard-Wyart et al. are found here for $\gamma = \infty$, corresponding to the full slippage case, and for $\gamma = 0$, corresponding to the no-slip case. τ_0 is the rupture time which is particular to the hole nucleation process itself and it is therefore unknown a priori. Eq. (1) express the fact in the initial phase of the hole growth, the main dissipation mechanism is slippage and $R \propto t^{2/3}$, while at later times, viscous effects dominate and $R \propto t$.

Other forms of dewetting

There are situations when the polymer would want to dewet itself. Early experiments showed that PS films would dewet a PS brush created by adsorption of a PS-block-PVP

diblock copolymer[42] or PS chemically grafted to the silicon substrate.[43,44] The penetration of the melt chains in the brush is restricted for purely entropic reasons although miscibility is expected for the brush and film of the same chemical species. This phenomenon is known as autophobicity. Autophobic behavior was also observed for a polyolefin film on a cross-linked polyolefin.[45,46] In another study, end-terminated PS with a sulphonate autophobically dewets a densely packed layer of end-terminated PS film on silicon.[47]

Another form of dewetting was observed where polymer films can dewet wettable substrates.[48] In this case, PEP films were observed to dewet silicon substrates, when the films thickness became less than the polymer radius of gyration. This may be due to the conformational entropy of a polymer chain in a thin polymer a film is not the same as that in the bulk.[49,50,51,52,53] Other mechanism includes a Marangoni flow mechanism in a phase separated blends.[54,55]

1.3.3 Stabilization of thin films

Stabilization of thin polymer films against dewetting is a problem of fundamental technological importance. Various strategies have been utilized to "stabilize" thin polymer films. Dewetting can be greatly suppressed in high molecular weight (entangled) or glassy polymer films, (T_g) spun-cast from solution. It is difficult for these films to equilibrate so that surface energies are less of a factor governing surface wetting. A shortcoming of this approach is that dewetting still tends to occur at long time scales. The "aging" of the film structure and associated formation of film defects over time can be detrimental to the applications for which the films were intended. Other previous strategies employed to stabilize thin films include grafting polymer layers to the

substrate[56], modifying substrate chemistry[47], introducing specialized end groups onto the polymer with a high affinity for the inorganic substrate[45], or by sulfonation and metal complexation of the polymer.[57] At present, these films stabilization effects are not well understood theoretically, but it seems clear that a combination of equilibrium (modification of polymer-surface interactions) and kinetic stabilization effects (changes in T_g) are generally involved. Recently a novel strategy based on introducing low concentrations of nanoparticles in the polymer has been shown to be useful in inhibition of dewetting in thin films as reported by Barnes et al.[58] and Mackay et al.[59] These groups utilized fullerene ('buckyballs', C_{60}) and poly(benzyl ether) dendrimers as nanoparticle additives respectively. Both groups found the addition of even a small amount of particles to the spin-casting solution led to a strong inhibition of film dewetting. This novel stabilizing method is striking in comparison to the normal effect of large particles and other film heterogeneities to enhance nucleation and subsequent film dewetting.[37,38]

This thesis examines the dewetting behavior of thin PS films containing polymer nanoparticles (formed mainly from the same material) as function of annealing time, nanoparticle concentration, nanoparticles type, and elucidated the possible mechanism for suppressing of dewetting in this system.

CHAPTER 2 SYNTHESIS OF STAR POLYMERS

2.1 Overview

Star polymers are branched structures with a central core from which emerge the linear chains (branches). If the arms of a star polymer are identical with respect to constitution and degree of polymerization, the macromolecule is termed a *regular* star polymer. If the arms of a star polymer are composed of different monomeric units, the macromolecule is termed a *variegated* star polymer.[60]

The topological constraint imposed by polymer chains attached to the center of the molecule changes configurational and dynamical properties compared to the linear polymer analogs. Because of this, star polymers have received considerable attention in the literature from both experimental[61,62,63,64,65] and theoretical[66,67,68, 69,70,71,72,73] points of view.

2.2 Synthesis of star polymers

Star polymers can be synthesized by group transfer polymerization or anionic polymerization. Most star polymers have been produced by anionic polymerization.[74,75,76,77,78,79,80,81,82] Two different methods of anionic polymerization of such star molecules have been described in the literature: arm first and core first. In the arm first method[75,76,77,78] living polystyrene with a carbanionic end group is copolymerized with a small amount of divinylbenzene resulting in a small densely crosslinked nucleus of poly (divinylbenzene) with the pendant polystyrene chains. In the core first method[79,80], divinylbenzene (DVB) is anionically polymerized in dilute solution by n-tertbutyl lithium, which results in densely crosslinked poly (divinylbenzene) particles. These particles have living cabanionic groups which are then

used to polymerize additional monomers yielding star molecules. Arm first star molecules are characterized by a relatively narrow molecular weight distribution and the number of branches is controlled by a pronounced diffusion control of the reaction. In contrast, core first method allows the desired functionality of the nuclei and any length of the side chains but the products are relatively more polydisperse.

The presence of active sites within the cores of star polymer in arm first molecules allows hetero-arm star polymers exhibiting two sets of branches arising form the same core to be synthesized.[81,82] Once the DVB has polymerized to a tightly cross-linked core, the active sites can be used to grow further branches form the core.

2.3 Synthesis at IBM

Intra-molecular crosslinked and uncrosslinked star molecules decorated with tert-butyldimethyl siloxy functionality or OH end groups were synthesized by the arm first method. The molecules consist of a nucleus of poly (divinylbenzene (DVB)) and arms of linear polystyrene copolymerized with 10 mol% benzocyclobutene (BCB). It has been shown that upon heating the benzocyclobutene (A) is in equilibrium with the very reactive o-quinodimethane species (B)[83] (Figure 2.1). This intermediate can undergo self-polymerization to give poly (o-xylylene) (C) or dimerize to yield a bisbenzocyclooctadiene derivative (D). The intra-molecular cosslinking of PS-BCB arms is carried out by the thermal rearrangement of the benzocyclobutene monomer to form the reactive intermediate ortho-quinodimethane, which can react with the orthoquinodimethane group on another arms and results in intra-molecular crosslinked star molecules.

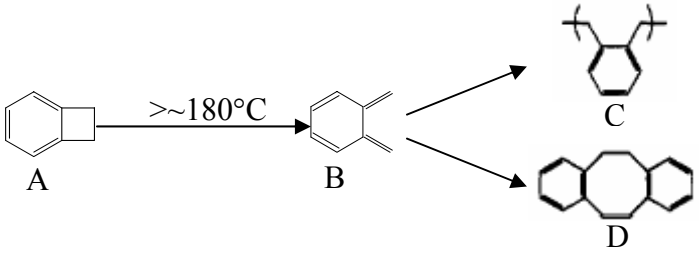

Figure 2.1. Chemical structure of Benzocyclobutene

The initiator was 3-tert-butyldimethylsiloxy-2, 2-dimethyl propyl lithium (shown below) available from FMC Corporation.

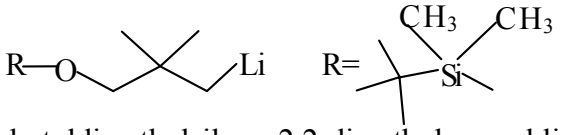

3-tert -butyldimethylsiloxy-2,2-dimethyl propyl lithium

OH end group can be formed by deprotecting the tert-butyldimethylsiloxy (BDMS) group. The schematic structure of both uncrosslinked and crosslinked star polymers are shown in Figure 2.2.

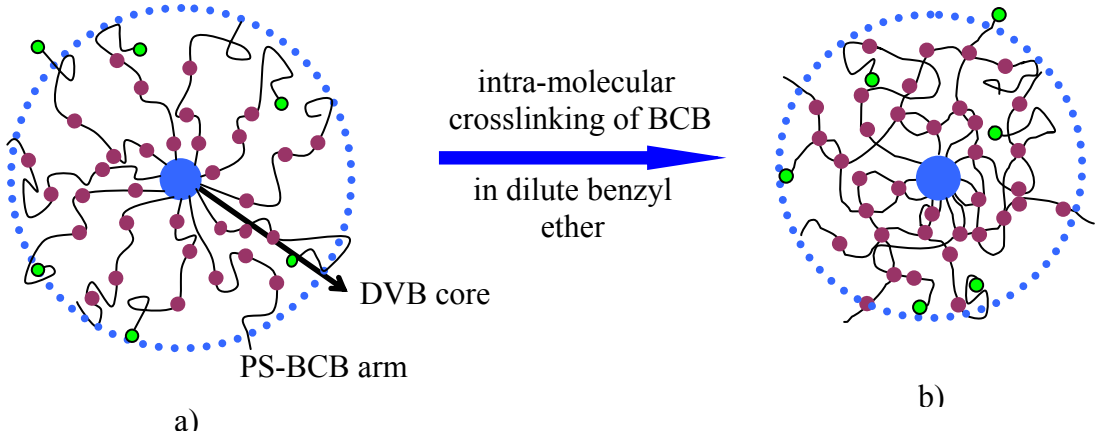

Figure 2.2. Schematic of star polymers: a) uncrosslinked, b) crosslinked.
● BCB; ● BDMS or OH.

The synthesis of these stars may be conveniently separated into five steps (Fig. 2.3)[84]. First is the copolymerization of PS and 10 mol% PS-BCB initiated by 3-t-butyldimethylsiloxy-2, 2-dimethyl propyl lithium. The second step is living polystyrene initiated polymerization of p-divinylbenzene to form the core. In the second step, the

pendant double bonds from divinylbenzene are crosslinked, where each crosslinking reaction necessarily implies one polystyrene branch. However, with increasing number of polystyrene chains, the crosslinking becomes increasingly sterically hindered because the primary chains have to move through a shield of polystyrene branches before crosslinking to the core can take place. This results in particles with a limited number of branches. At this point, a polyanionic star with f linear polymer arms from a small polyanionic core is produced.

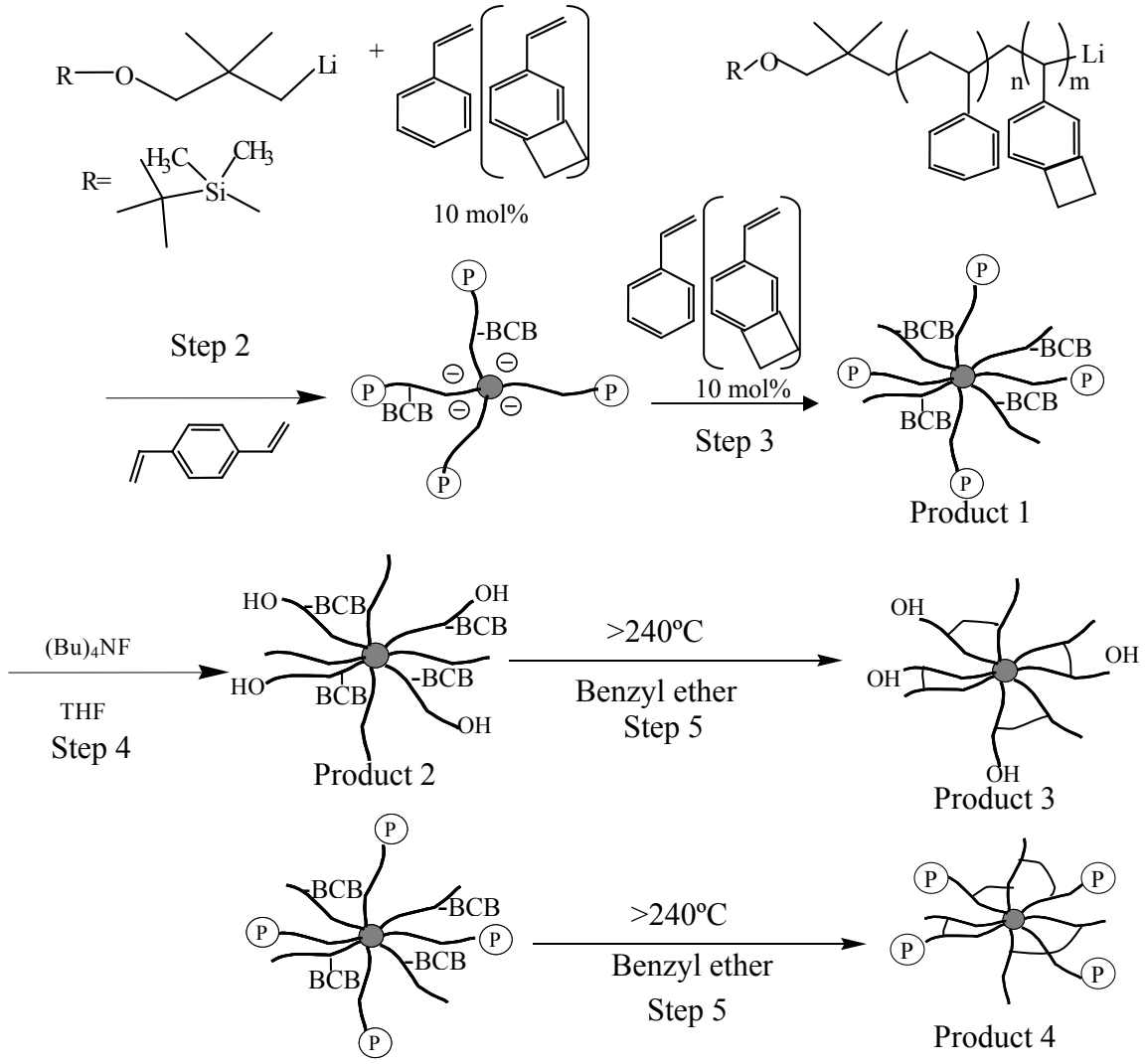

Figure 2.3. The schematic of the process of polymerization of star polymers

In the third step, taking the advantage of the remaining active sites within polyanionic core, subsequent addition of styrene/BCB (10mol %) monomer leads to the growth of additional f arms (without BDMS) from the core (product 1). In step 4, the t-butyldimethyl siloxy protecting groups were removed with tetrabutyl ammonium fluoride (1M in THF) to produce OH groups (product 2). In step 5 the intra-molecular crosslinking of the stars occurs through ring opening of BCB on the arms in dilute benzyl ether solution by heating above 240°C (product 3, 4). The star molecules studied in this thesis are list in Table 2.1.

Table 2.1. Characteristics of star molecules

Samples	Mw	f	PDI
35-BDMS (uncrosslinked)	488,000	50	1.10
32-BDMS (crosslinked)	526,000	50	1.09
35-OH (uncrosslinked)	530,000	50	1.09
32-OH (crosslinked)	530,000	50	1.11
36-BDMS (uncrosslinked)	506,000	50	1.10
31-OH (crosslinked)	524,000	50	1.17
16-OH (uncrosslinked)	215,000	46	1.14*
29-OH (crosslinked)	247,000	46	1.19*

*: PDI was measured at University of Maryland, College Park.

CHAPTER 3 CHARACTERIZATION OF NANOPARTICLES IN SOLUTION

3.1 Overview

As part of understanding of the influence of nanoparticles on the dewetting behavior of polymer thin films, it is important to examine the conformation and size of the nanoparticles in solution and in bulk blend. The conformation of nanoparticles in solution will be studied in this chapter.

SANS was used to study the radius of gyration (R_g) of polystyrene based star polymers before and after intra-molecular crosslinking to test how well the scattering of star molecules that have a large number of relatively short arms fit the Daoud-Cotton model.[85] Dynamic Light scattering (DLS) also known as "photon correlation spectroscopy" (PCS) or "quasi-elastic light scattering" (QELS) is another important way to characterize macromolecules.[86] By determining the autocorrelation function, which relates the correlation of the system at one time with itself at a different time, the diffusion coefficients of the particles doing the scattering can be determined. The hydrodynamic diameter, R_h is then obtained from the diffusion coefficient, D, through the Stokes-Einstein relationship (eq. 3.6)[87].

$$D = \frac{kT}{6\pi\eta R_h} \qquad \text{eq. 3.6}$$

where k is Boltzman's constant, T is absolute temperature in K and η is solvent viscosity. DLS was used to measure the hydrodynamic radius of both crosslinked and uncrosslinked star polymers.

Combining the information from SANS and DLS, the ratio of the radius of gyration to the hydrodynamic radius provides insight into the polymer segment density profile.[88] The ratio for star molecules should be within the range of value for linear unperturbed

polymer (1.25-1.37)[89] and value for uniform-density hard sphere 0.77[90]. With increasing number of arms it is expected that the segment density of star polymers will increase and the ratio of R_g/R_h will approach to the value for a hard sphere.[91]

3.2 Small angle neutron scattering

3.2.1 Materials

Deuterated toluene (toluene-d_8) with 99.6% isotopic enrichment min. atom% and cyclohexane (cyclohexane-d_{12}) with 99.5% isotopic enrichment min. atom% were purchased from C/D/N isotopes Inc. Star molecules PS-BCB consisting of a nucleus of polydivinylbenzene and arms of linear polystyrene copolymerized with benzylcyclobutene were synthesized by IBM Almaden Research Center as described in Chapter 2 in this thesis.

3.2.2 Sample preparation

Solutions for small angle neutron scattering were prepared by dissolving the nanoparticles in deuterated solvent: toluene-d_8 or cyclohexane-d_{12} to obtain concentrations in the range of 0.15-4% by weight.

3.2.3 SANS measurements

The scattering experiments were carried out as a function of temperature and concentration at the National Institute of Standards and Technology Cold Neutron Research facility (NCNR) using the 30m NG7 or NG3 SANS spectrometer. The data was corrected for scattering from the empty cell, detector sensitivity, sample transmission, and circularly averaged to produce I(q) vs. q plots. The final scattering data is obtained by extrapolating to zero polymer concentration.

3.2.4 Results and discussion

Radius of gyration

A typical set of SANS data for star polymers as a function of concentration in cyclohexane-d_{12} is shown in Figure 3.1 (T=55°C, 35-BDMS). To eliminate interparticle effects, the scattered intensities were extrapolated to the limit of zero concentration at every value of q using equation 3.1[92,93]:

$$\phi/I(q) = B + A\phi \qquad \text{eq. 3.1}$$

where ϕ is the volume fraction of polymer of interest, I(q) is the scattered intensity, q is the scattering vector and the intercept, $B=\lim_{\phi\to 0}\left[\phi / I(q)\right]$ is the limiting zero concentration scattering. Based on linear least squares fit, A & B should satisfy:

$$3B + (\Sigma\phi_i) \times A = (\Sigma\phi_i/I(q)) \qquad \text{eq. 3.2}$$

$$(\Sigma\phi_i)\times A + (\Sigma\phi_i^2) \times A = (\Sigma\phi_i \times \phi_i/I(q)) \qquad \text{eq. 3.3}$$

Solving equations 3.2 and 3.3, gives

$$B=\lim_{\phi\to 0}\left[\phi / I(q)\right] = \frac{(\Sigma\phi_i^2) \times (\Sigma\phi_i/I(q)) - (\Sigma\phi_i \times \phi_i/I(q)) \times (\Sigma\phi_i)}{3(\Sigma\phi_i^2) - (\Sigma\phi_i) \times (\Sigma\phi_i)}.$$

Volume fraction was calculated with the constant density of 0.94g/cm^3 for toluene-d8, 0.89 g/cm^3 for cyclohexane-d_{12}, and 1.05 g/cm^3 for the star polymers which is equivalent to the value for pure polystyrene.

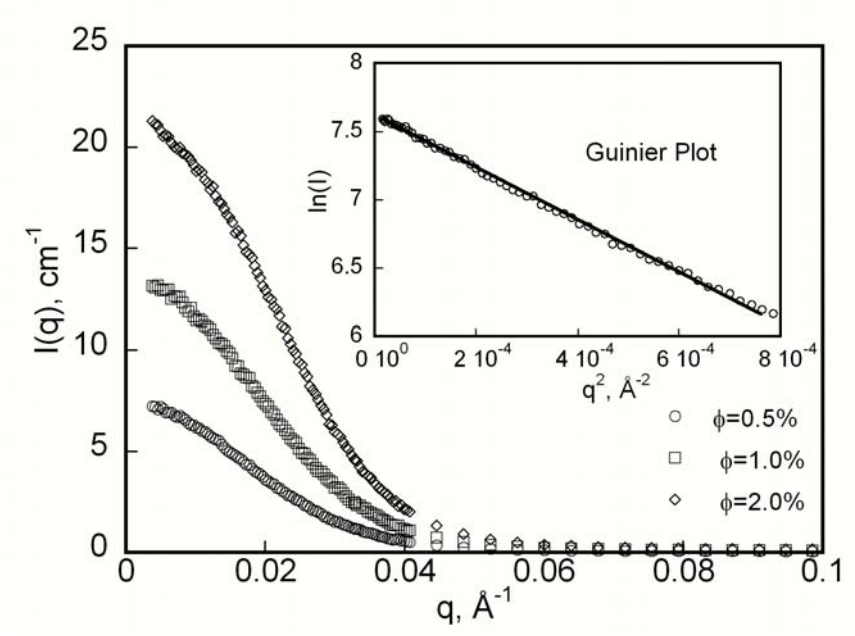

Figure 3.1. I(q) as a function of concentration for 35-BDMS at 55°C. Inset shows a typical Guinier plot used to obtain R_g.

All radii of gyration for star polymers were measured using Guinier plots[94,95] at small q as given by eq. 3.4:

$$I(q) = I(0) \exp(-R_g^2 q^2/3) \qquad \text{eq.3.4}$$

where I(0) is the scattering intensity at q = 0. The Guinier plot of ln I(q) versus q^2 for 35-BDMS is displayed as an inset in Figure 3.1 which clearly shows a Guinier region. The variations in R_g obtained from Guinier plots as a function of temperature for 35-OH, 35-BDMS and 32-BDMS were shown in Figure 3.2. The error bars in Figure 3.2 represent the standard deviation calculated form the linear least squares fit of the Guinier plot data.

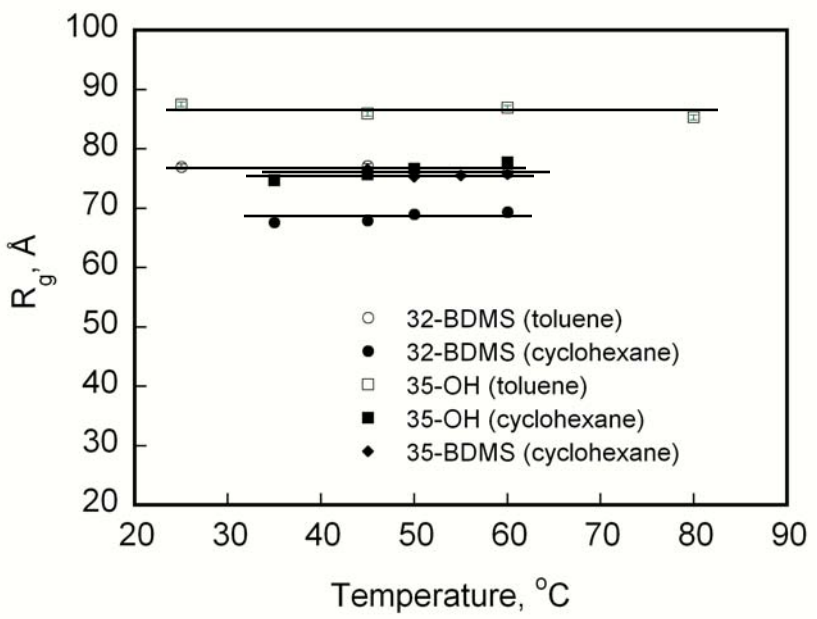

Figure 3.2. Radii of gyration of nanoparticles as function of temperature.

As can be seen from Figure 3.2, the sizes of uncrosslinked and crosslinked star shaped polymers are independent of temperature in the range investigated. This is consistent with the temperature dependence of Rg for aboresent graft polystyrene observed by Choi et al.[96].

Table 3.1 shows the radii of gyration from Guinier plots in two different solvents: cyclohexane-d_{12} and toluene-d_8. All radii of gyration in cyclohexane-d_{12} were acquired at 45°C and radii in toluene-d_8 were obtained at 25°C. In general, SANS data on solutions of uncrosslinked and crosslinked star molecules show values of R_g in the range of 5-9 nm depending on solvent and the type of nanoparticles. A decrease of 8-14% for the R_g of the star polymers was observed in going from toluene-d_8 to cyclohexane-d_{12}. This indicates deuterated toluene is a better solvent for PS-BCB based star polymers than deuterated cyclohexane which is consisted with the fact that cyclohexane is a θ solvent with a θ

temperature of 40°C and toluene is a good solvent for linear polystyrene.[97] Upon crosslinking, there is a 6-14% decrease in the R_g of star polymers.

Table 3.1. Radius of gyration from Guinier plots in two different solvents

Samples	Cyclohexane, 45°C			Toluene, 25°C		
	R_g, Å	R_h, Å	R_g/R_h	R_g, Å	R_h, Å	R_g/R_h
16-OH	56.0	63.0	0.89	60.7	100.0	0.61
29-OH	51.5	56.0	0.92	56.8	94.0	0.60
36-BDMS	76.6	116.0	0.66	87.4	138.0	0.63
31-OH	-	-		77.5	124.0	0.63
35-BDMS	76.6	99.0	0.77	82.7	134.0	0.62
32-BDMS	67.9	91.0	0.75	77.0	114.0	0.68
35-OH	75.7	104.0	0.73	87.5	138.0	0.64
32-OH	-	95.0		75.4	-	

Scaling prediction of star polymers

The scaling relation for size of star polymers in solution has been studied by the Daoud-Cotton model which shows R_g dependence on f and N as[85]:

$$R_g^2 \sim N^{2\nu} f^{1-\nu} \qquad \text{eq.3.5}$$

where ν denotes the Flory exponent, f is the functionality and N is the number of monomers per arm. The model divides the star into three different regions. In the case of long arms, the swollen (good solvent) regime dominates, and ν=0.6; for shorter arms, the unswollen regime dominates and ν=0.5 and for even shorter arms, the stars behave like uniform dense objects and ν=1/3. Figure 3.3 shows plot of R_g^2/f as a function of $(N^2/f)^{\nu}$ for uncrosslinked and crosslinked stars in toluene. The solid line represents the expected Daoud-Cotton scaling behavior in good solvent toluene-d_8 at 25°C (ν=0.6). It can be seen that in the case of uncrosslinked stars with longer arms the predicted scaling is well

verified, while deviation was observed for stars with relatively short arms (first data point for polymer with f = 46, Mw=215000), indicating the stars with shorter arms in the study are not long enough and the swollen regime doesn't dominate. Similar deviation was found by Willner et al. for polyisoprene and polybutadiene stars with relatively fewer arms (for example, f=18, Mw=134000).[98] The inset in this diagram is the linear least squares fit of Daoud-Cotton scaling model. The scaling exponent ν was 0.44±0.01 for uncrosslinked stars and the uniform dense objects like behavior was observed for crosslinked stars with ν=0.32±0.07 due to intra-molecular crosslinking. This is consistent with the common concept that crosslinking will make the star behaves more like a core with a constant density.

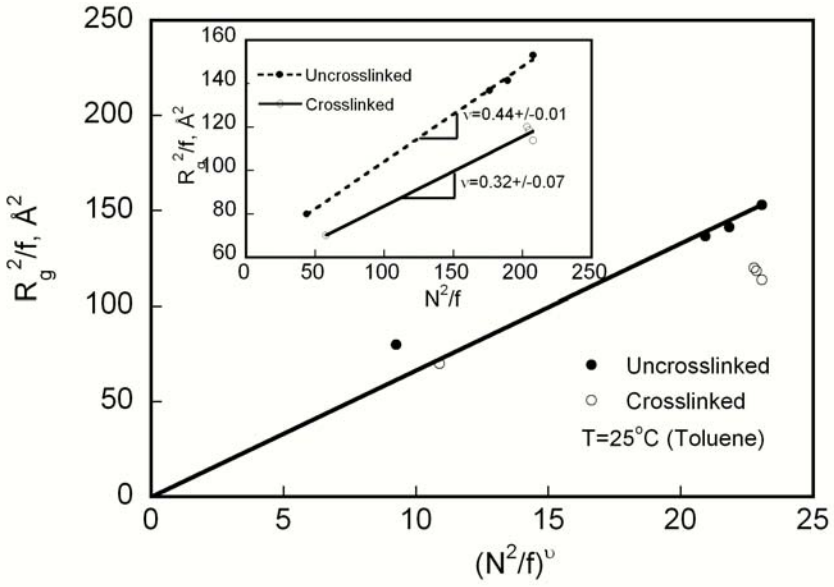

Figure 3.3. Plot of Rg^2/f as a function of $(N^2/f)\nu$ for uncrosslinked and crosslinked stars in toluene.

The value of ν=0.32±0.05 was observed for star molecules in cyclohexane (Figure 3.4) which also signifies a dense objects like behavior region (ν=1/3) since cyclohexane is a good solvent for linear polystyrene.

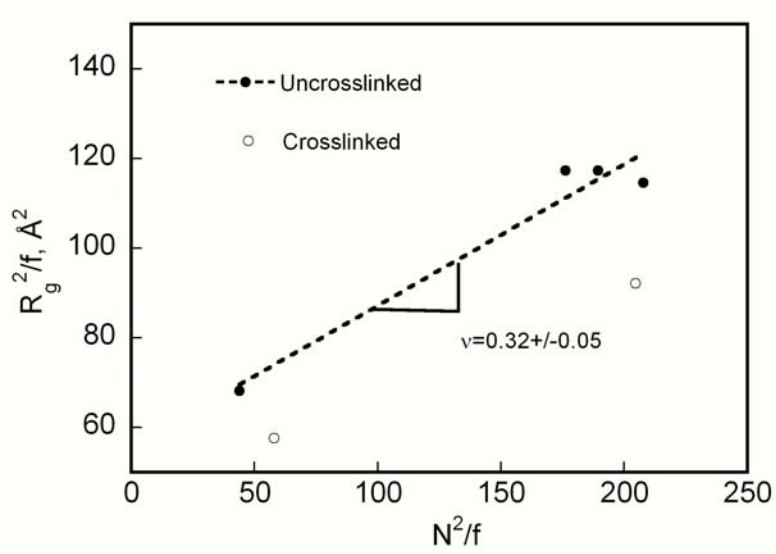

Figure 3.4. Plot of Rg^2/f as a function of N^2/f for uncrosslinked and crosslinked stars in cyclohexane. The solid line is fitting for Daoud-Cotton model with $\nu=0.32\pm0.05$.

3.3 Dynamic light scattering

3.3.1 Sample preparation

Samples for dynamic light scattering were prepared as 0.25 wt% nanoparticles in cyclohexane and toluene and measured at 45°C and 25°C respectively.

3.3.2 Dynamic light scattering

Samples were prepared as 0.25 wt% star molecules in cyclohexane and toluene and measured at 45°C and 25°C respectively. Dynamic light scattering measurements were performed at a 90° scattering angle on a DynaPro-LSR (Protein Solution Inc.) at a wavelength of 781.8 nm. During the measurements, the temperature was maintained using a built-in temperature controller. The hydrodynamic radius was obtained from the autocorrelation function, using the DYNAMICS V6 software.

3.3.3 Results and discussion

All hydrodynamic radii were obtained from the autocorrelation function using the DYNAMICS V6 software which gave good fits for the autocorrelation functions for all samples. As an example, the autocorrelation function and the fit for 35-BDMS in toluene at 25° C is shown in Figure 3.5.

The hydrodynamic radii R_h of the star molecules are summarized in Table 3.1 and R_h values obtained from DLS were compared to the R_g values from SANS of the corresponding nanoparticles in the same solvent. It was found that the ratio of the radius of gyration to the hydrodynamic radius for crosslinked and uncrosslinked star molecules ranged between 0.92 and 0.60. R_g/R_h for nanoparticles with 50 arms was between 0.78 and 0.60, which is close to (but deviates from) the value for a constant density sphere (0.77)[90]. Trollsas et al. found a similar deviation of R_g/R_h for dendrimer-like star polymers (R_g/R_h in the range 0.70 to 0.53)[99]. This deviation is due to the non-uniform segment density distribution in the stars with a denser core[70,99,100].

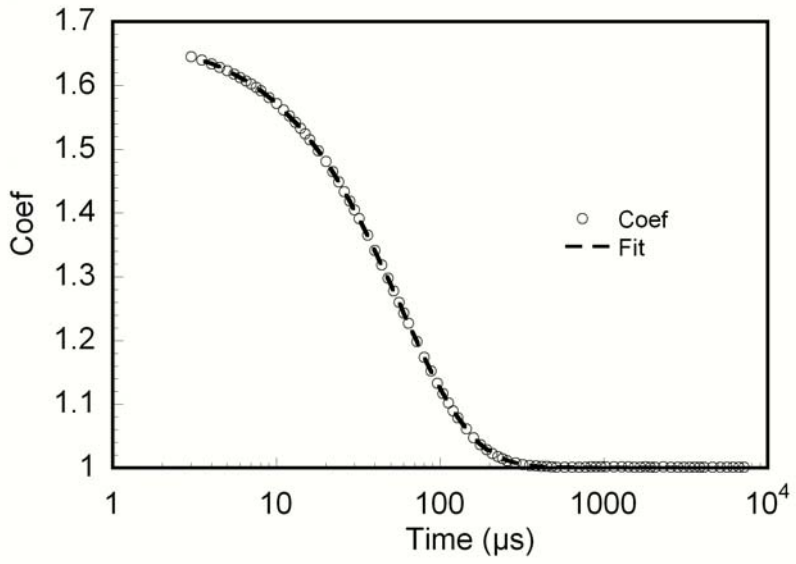

Figure 3.5. Autocorrelation function in toluene at 25 °C for 35-BDMS.

Roovers et al.[101,102,103]studied star polymers in solution by intrinsic viscosity and SANS. They found the conformation of star molecules with 64 or 128 arms in good solvent was in good agreement with the Daoud-Cotton model and a ratio of R_g/R_h close a hard sphere value (0.77) was observed[101,102]. For star molecules with 46-50 arms and weight average molecular weight of 200,000-550,000, a ratio of R_g/R_h close a hard sphere value (0.77) may be expected.[101,102,103]

Figure 3.6 shows both uncrosslinked and crosslinked nanoparticles exhibit a peak in the Kratky plot (Iq^2 vs q), which is indicative of particle-like behavior; yet a high wavevector plateau is present for both uncrosslinked star and crosslinked stars after the low q maximum, which is suggestive of both particle and Gaussian chain behavior.[101]

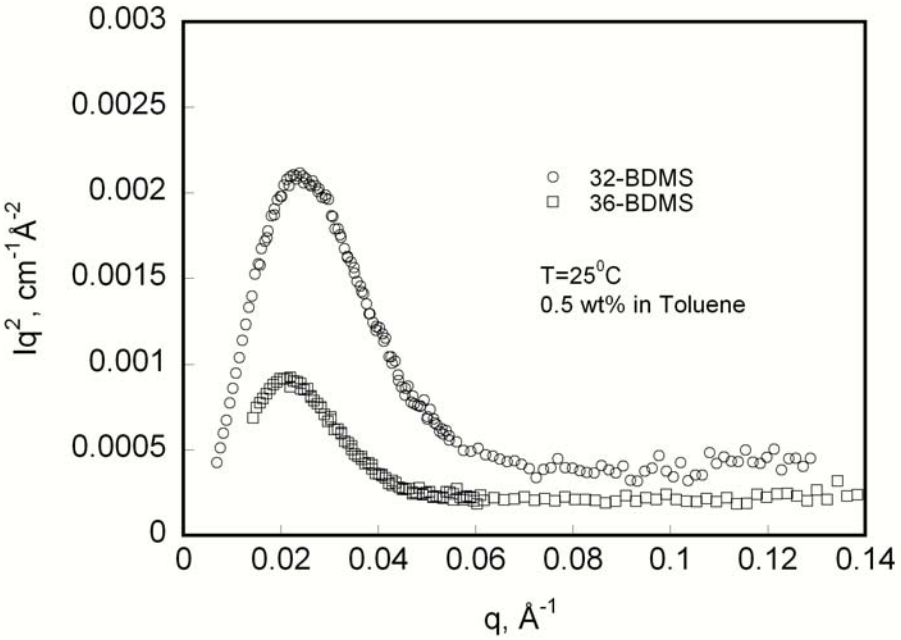

Figure 3.6. Kratky plot of SANS data for 0.5 wt% of 35-BDMS and 32-BDMS in toluene at 25 °C. The maximum in the curve indicates particle-like behavior.

In conclusion, the radius of gyration of star polymers studied is in the range of 5-9 nm, and it was found that the temperature has no effect on the size of radius of gyration of polystyrene based stars over the experimental range investigated. In going from toluene-d_8 to cyclohexane-d_{12}, the R_g of the star polymers was observed to decrease 8-14%. The R_g of crosslinked polymers is 6-14% smaller than the corresponding uncrosslinked polymers in the two solvents studied. The chain configuration of uncrosslinked long arm star polymers in toluene follows the Daoud-Cotton scaling prediction for good solvents ($\nu = 0.6$), while crosslinked star polymers in toluene and uncrosslinked star polymer in cyclohexane showed uniform dense objects like behavior ($\nu = 1/3$). The R_g/R_h values for both crosslinked stars and uncrosslinked stars are close to the value for a hard sphere, indicating the particle-like characteristic of the star polymers.

CHAPTER 4 CONTACT ANGLE MEASUREMENTS

4.1 Overview

Surface energy potential is an important factor that affects the wetting behavior of polymers on Si substrate. Any surface energy changes due to the addition of the PS based nanoparticles were evaluated by contact angle measurement. One method of measuring the surface energy of solids is based on the measurement of the contact angle with water and methylene iodide.[104,105] Wu[105] proposed an equation based on "reciprocal" mean and force additivity for calculating the interfacial tension between polymers or between a polymer and an ordinary liquid:

$$\gamma_{12} = \gamma_1 + \gamma_2 - \frac{4\gamma_1^{\,d}\gamma_2^{\,d}}{\gamma_1^{\,d} + \gamma_2^{\,d}} - \frac{4\gamma_1^{\,p}\gamma_2^{\,p}}{\gamma_1^{\,p} + \gamma_2^{\,p}} \qquad \text{eq. 4.1}$$

where γ_{12} is the interfacial tension; γ_i is the surface tension; γ_i^d and γ_i^p the dispersion and polar components of γ_i, respectively. This equation is shown to predict accurately the interfacial tension between polymers or between a polymer and an ordinary liquid. The above equation can also be used to calculate the surface tension and polarity of polymers or organic solids from contact angle data by two simultaneous equations, 1 for water and 2 for methylene iodide:

$$(b_1 + c_1 - a_1)\,\gamma^p\gamma^d + c_1(b_1 - a_1)\,\gamma^d + b_1(c_1 - a_1)\,\gamma^p - a_1b_1c_1 = 0 \qquad \text{eq. 4.2}$$

$$(b_2 + c_2 - a_2)\,\gamma^p\gamma^d + c_2(b_2 - a_2)\,\gamma^d + b_2(c_2 - a_2)\,\gamma^p - a_2b_2c_2 = 0 \qquad \text{eq. 4.3}$$

Where γ^d and γ^p are the components of the surface tension of the solid polymer; $a_1=(1/4)(\gamma_1)(1+\cos\theta_1)$, $b_1=\gamma_1^d$, $c_1=\gamma_1^p$, $a_2=(1/4)(\gamma_1)(1+\cos\theta_2)$, $b_2=\gamma_2^d$, $c_2=\gamma_2^p$; θ_1=contact angle of liquid 1, and θ_2=contact angle of liquid 2 on the polymer. The properties of liquids used for the calculations of the surface energy of PS are given in Table 4.1[104,106].

Table 4.1. Properties of liquids at 20°C

Liquids	γ_l^d	γ_l^p	γ_s (ergs/cm^2)
Water	21.8±0.7	51.3	72.8
Methylene iodide	49.5	1.3	50.8

4.2 Experiment

Contact angle was estimated by dropping ≈10 μL of solvent on the film surface with values averaged from 4-5 droplet readings using a Rame-Hart contact angle goniometer.

4.3 Results and discussion

Table 4.2 shows results of deionized water contact angle measurements for the crosslinked 32-OH filled and unfilled PS films. A contact angle of 90° was observed at the surfaces of three different films: pure PS, pure crosslinked 32-OH and 5 wt% crosslinked 32-OH filled PS. Complementary contact angle measurements with methylene iodide under the above identical conditions showed similar results with contact angle of 33-34° for all the three different surfaces. This is consisted with Wu's contact angle measurements of pure polystyrene as 91° with deinoized water and 35° with methylene iodide[105]. No contact angle change by adding nanoparticles suggests that any surface energy changes at the air/polymer surface are small since the end group to the monomer ratio in the whole molecule is small (~1:200) or end groups may be completely buried below any surface polystyrene chains.

Table 4.2. Contact angle on different thin films

	Contact angle, º		ergs/cm^2		
Surface	Water	Methylene iodide	γ_s^d	γ_s^p	γ_s
Pure PS	90±1	33.7±2.0	40.5	4.4	44.9
Nanoparticles filled PS	90±1	34.5±4.0	40.1	4.4	44.5
Nanoparticles film	90±1	33.9±1.1	40.4	4.4	44.8

Based on the measured contact angle values of PS with demonized water and methylene iodide, the surface tension γ_s, the dispersion and polar components γ_i^d and γ_i^p of PS are calculated according to equation 4.2 and 4.3 (Table 4.2). The surface tension γ_s, the dispersion and polar components γ_i^d and γ_i^p of PS are ~44.7, ~40.3, and ~4.4 ergs/cm^2 respectively. If use the same parameters in Table 4.1, the surface tension γ_s, the dispersion and polar components γ_i^d and γ_i^p of PS based on contact angle of 91 with deionized water and 35 with Methylene iodide are ~44.0, ~40.0, and ~4.0 ergs/cm^2 respectively, very close to data obtained by our measurements.

CHAPTER 5 BULK MISCIBILITY OF BLENDS OF PS AND NANOPARTICLES

5.1 Overview

As part of understanding of the influence of nanoparticles on the dewetting behavior of polymer thin films, it is important to examine the conformation and size of the nanoparticles in solution and in bulk. The conformation of nanoparticles in bulk blends and the miscibility of the nanoparticles with pure PS will be studied in this chapter.

Bulk immiscibility of the linear polystyrene with the nanoparticles has the potential to strongly affect the distribution of nanoparticles in the thin films. One of the most powerful methods for establishing miscibility in polymer blends is small angle neutron scattering. If the mixture is miscible them the scattering should obey the random phase approximation scattering for a polymer blend[9].

Many factors affect the bulk miscibility in binary blends of polymers, such as differences in molecular weight, in chemical microstructure[107,108,109], tacticity[110], deuterium labeling[111], and chain architecture. There have been a few recent theoretical studies for stars[112,113,114] as well as some experimental work on the thermodynamics of blends of linear and regularly star branched polymers[115,116,117]. It is suggested that the thermodynamic interactions due to architecture are present, and for the first time Greenberg et al.[118] experimentally determined the magnitude of these effects and compared it to the theory.

Miscibility in polymer blends of linear PS and star polymers is a delicate balance between the small enthalpies of mixing, ΔH, which are generally unfavorable for mixing and small mixing entropy due to the large size of the molecules, ΔS (generally favorable for mixing). It is reasonable to expect that the star molecules prior to crosslinking may be

miscible with the linear PS. An interesting question is whether linear chains will swell the crosslinked stars. The swelling process gives rise to an elastic energy contribution to the free energy of mixing, ΔF_{elas}, which generally adds in an unfavorable manner to total mixing free energy.[119] The intra-molecular crosslinking could potentially result in immiscibility and phase separation of the star molecule with the linear chains.

SANS experiments were performed on blends of the linear polymer with the star molecules as a function of temperature to establish compatibility of the linear matrix with the star molecules and measure the effective Flory interaction of linear chains with the star molecules.

5.2 Experiment

Sample preparation

Sample blends containing nanoparticles in linear PS were prepared for SANS by dissolving the two polymers in toluene (~2 wt% of total solids), followed by evaporation in a Teflon pan. The dried films were pressed in 1 mm thick brass rings at 140°C to create bubble free films.

SANS measurement

The scattering experiment were carried out as a function of temperature (25 to 175°C) for star polymer blends at NCNR Facility using the 30m NG3 or NG7 SANS spectrometer with a wavelength of 6 Å. The data was corrected for scattering from the empty cell, detector sensitivity, sample transmission, and circularly averaged to produce the I(q) vs. q plots.

5.3 Results and discussion

5.3.1 Form factor of star polymers

It was shown that the scattering for a uniform star polymer with monodispersed arms which follow Gaussian statistics was first calculated by Benoit[120], and later by Burchard in terms of number of arms, f, R_g.

$$P(q) = \frac{2}{x^2}\left[\frac{x}{f} - \frac{(1-\exp(-x))}{f} + \frac{(f-1)}{2f}(1-\exp(-x))^2\right] \qquad \text{eq. 5.1}$$

Where $x = \frac{f}{3f-2} R_g{}^2 q^2$.

Alessandrini and Carignano[121] introduced a simple formula for the scattering in the self avoiding walk limit. [18] This formula represents a best nonlinear fit of an equation derived by renormalization group techniques, which was developed for stars in order to incorporate the excluded volume effects of monomers in a good solvent. However, Willner et al.[98] showed that both theories are limited in describing the experimental star form factors. In order to arrive at an approximation for the form factor of a star polymer, they consider that two different length scales govern a star: the overall size R_g and the correlation length or blob size, ξ where the granular polymer structure becomes important. At length scales $r \sim R_g$ the star is described by its average monomer density distribution p(r), while at scales $r < \xi$, the correlation within a single chain in a good solvent dominate. Thus the overall pair correlation function may be written as:

$$G(r) = \begin{cases} \sim \int \rho(r')\rho(r-r')d^3r' & r \approx R_g \\ \sim \sigma^{-1/\nu} r^{1/\nu - 3} & r \le \xi \end{cases} \qquad \text{eq. 5.2}$$

Where σ is the segment length and ν is Flory-Huggins parameter.

Dozier et al.[122] presented an approximation to eq 5.2. In order to assure the correct behavior in the Guinier regime, they described the long-range correlations by a Gaussian, giving rise to the proper radius of gyration. The polymer type short range correlations were taken into account by the correlation function of a swollen chain including a cut off function exp (-r/ξ). Since both contributions exhibit their decay on well-separated length scales, the total correlation function was written as a sum of both:

$$G(r) = c_1(\frac{\pi}{R_g})^3 \exp(-\frac{3r^2}{4R_g}) + c_2 \exp(-r/\xi)(\frac{r}{\sigma})^{1/\nu} r^{-3} \qquad \text{eq. 5.3}$$

c_1 and c_2 are numerical constants. Fourier transformation leads to the scattering function: Where

$$P_b(q) = \exp(\frac{q^2 R_g^{\ 2}}{3}) + \frac{\alpha}{V_w q\xi}\frac{\sin[\mu \tan^{-1}(q\xi)]}{(1+(q\xi)^2)^{\mu/2}} \qquad \text{eq. 5.4}$$

Where $V_w = \upsilon Nf, \mu = 1/\nu - 1, and\ \alpha \sim \upsilon(\xi/\sigma)^{1/\nu}$, N is the number of monomers per arm and υ is the molar volume of the monomer.

Figure 5.1 shows the Benoit fit (eq. 5.1) and Willner fit (eq. 5.4) for scattering of 35-BDMS and 32-BDMS in deuterated toluene at 25°C. It can be seen that Willner equation shows a better fit than the Benoit equation. The R_g values of 35-BDMS and 32-BDMS given by Willner fit are 83.7 and 76.7 Å respectively, which are close to the values obtained from the Guinier fits (82.7, 77.0 Å, Chapter 3, Table 3.1) compared to the R_g values from Benoit fit (89.6 and 85.3 Å respectively).

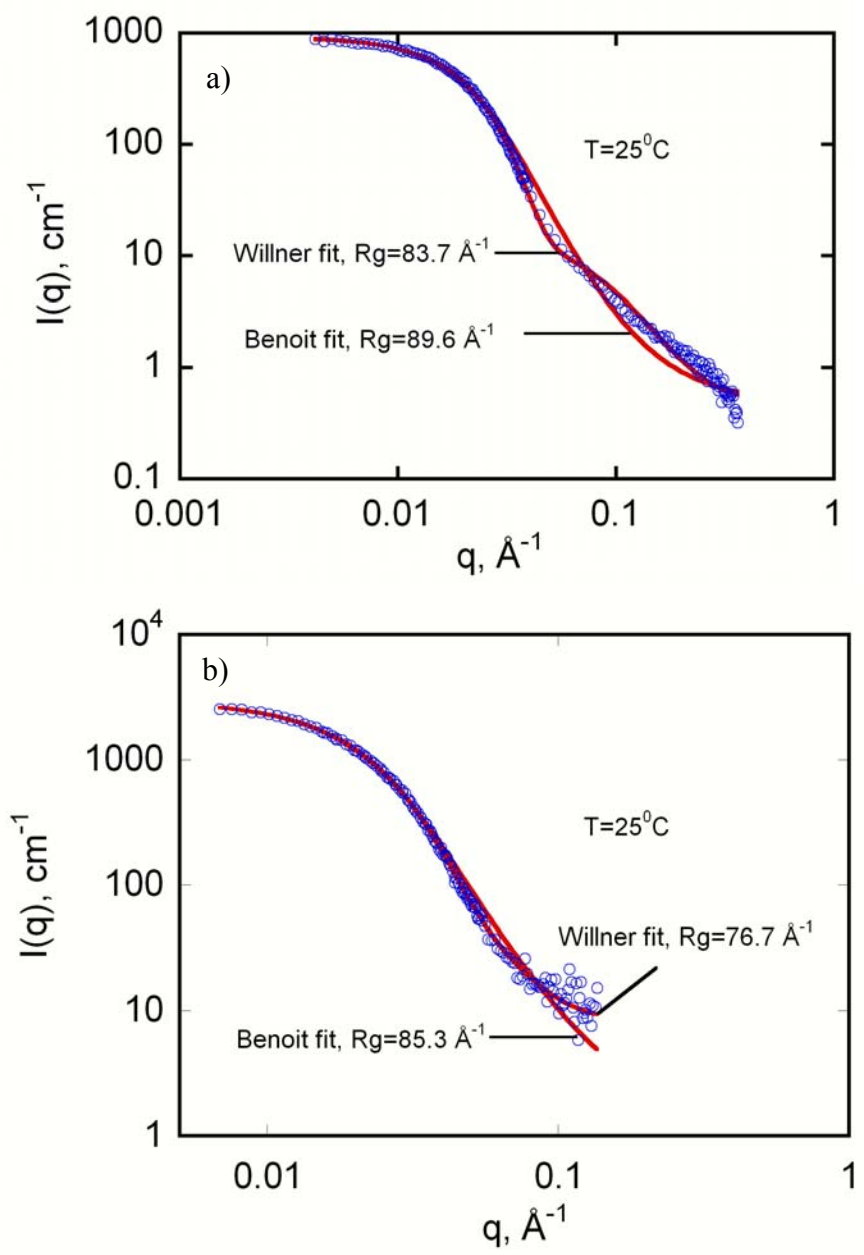

Figure 5.1. Benoit fit and Willner fit for a) 35-BDMS and b) 32-BDMS in deuterated toluene at 25 °C extrapolated to ϕ=0.

5.3.2 Miscibility

Bulk miscibility of blends of linear PS with 5 wt% star molecules was studied by small angle neutron scattering at 25, 140, 175 °C. SANS curves for 5 wt% uncrosslinked 35-BDMS and crosslinked 32-BDMS filled blends at 25 °C were shown in Figure 5.2. The

inset is the plot of 1/I(q) versus q^2 at low q, the solid line is the linear fit with a positive intercept indicating the blend is miscible[107,123]. Similar results were obtained at the other temperatures. SANS curves for blends filled with other star molecules shows the same results. It is not surprising that uncrosslinked 35-BDMS is miscible with its linear matrix as Fredrickson et al. theoretically predicted that phase separation in a mixture of linear and stars with modest number of polymeric arms (degree of polymerization, N>100) due to the architecture difference only is unlikely.[124] OH end group and intra-molecular crosslinking can contribute to the unfavorable interaction parameter χ between the molecules; however this system is still in one phase under the experimental condition studied here.

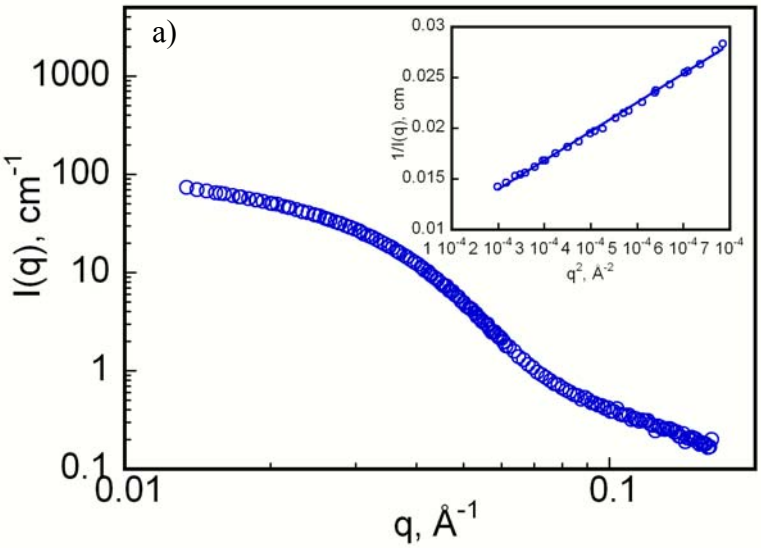

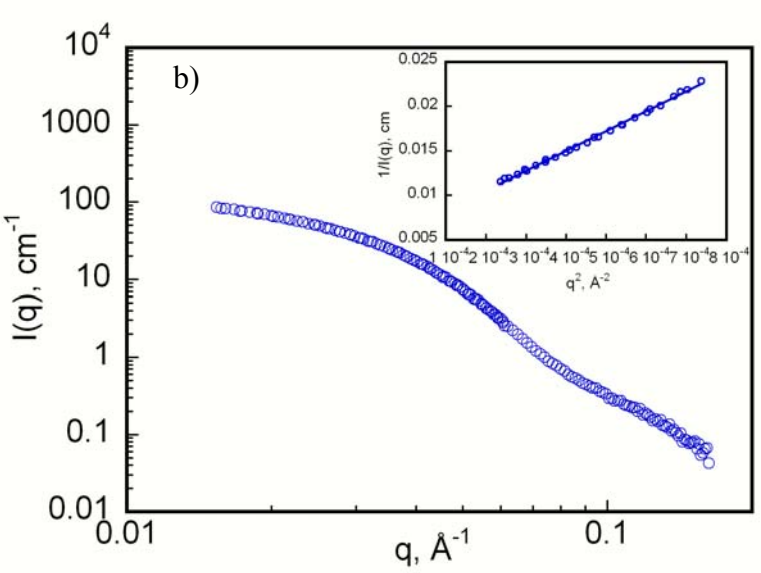

Figure 5.2. SANS curves for blends at 25°C filled with 5 wt% a) uncrosslinked 35-BDMS and b) crosslinked 32-BDMS.The inset is the plot of 1/I(q) versus q2 at low q, the solid line is the linear fit with a positive intercept.

5.3.3 RPA fitting

de Gennes[9] calculated the total coherent scattering from binary (miscible) mixture of polymers using the random phase approximation (RPA) as:

$$\frac{k_n}{I(q)} = \frac{1}{< X_a > \upsilon_a < P_a(q) >} + \frac{1}{< X_b > \upsilon_b < P_b(q) >} - 2\frac{\chi}{\upsilon_0} \qquad \text{eq.5.5}$$

Where $P_a(q)$ and $P_b(q)$ are the single chain form factor for species a and b respectively. The value ϕ is the volume fraction of each component and χ is the Flory interaction parameter, υ_i is the monomer molar volume of species i, υ_0 is the reference volume $(\upsilon_a \upsilon_b)^{1/2}$, and X_i is number average degree of polymerization. k_n is the contrast factor for neutrons defined as $N_A[(b_a/\upsilon_a)-(b_b/\upsilon_b)]^2$ where b_i is the scattering length per mole of monomer and N_A is Avogadro's number.

For a monodisperse linear polymers P(q) can be described by the Debye function[125]:

$$< P(q) >= \frac{2}{x^2}[\exp(-x) - 1 + x] \text{ where } x = (N\ell^2/6)q^2. \qquad \text{eq. 5.6}$$

Radii of gyration

We use eq. 5.6 for linear PS with Rg (dPS) of 39 Å with ℓ=6.9 Å, and eq. 5.4 for P_b (q) with ξ of 26 Å, ν of 1/3 to match the shape of the curve using three floating parameters, χ and α and R_g of star polymers. A correction scaling factor of order unity was used to account for random and systematic errors in the determination of the absolute intensity, including loss of intensity due to the formation of bubbles in the cell at higher temperatures. SANS curves for linear PS (Mn, 21k) blended with 5 wt% 35-BDMS and 32-BDMS nanoparticles at 100^{o}C were shown in Figure 5.3a and 5.3b respectively. The solid lines are the RPA fits based on equation 5.5 with Rg (dPS) of 39 Å, ξ of 26 Å, ν of 1/3. The variations of Rg with temperature determined for different star/linear blends are summarized in Table 5.1.

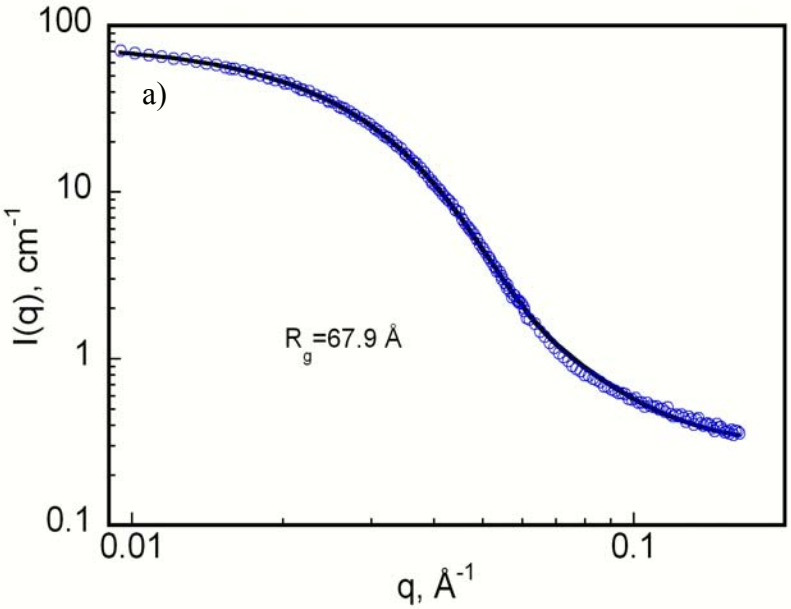

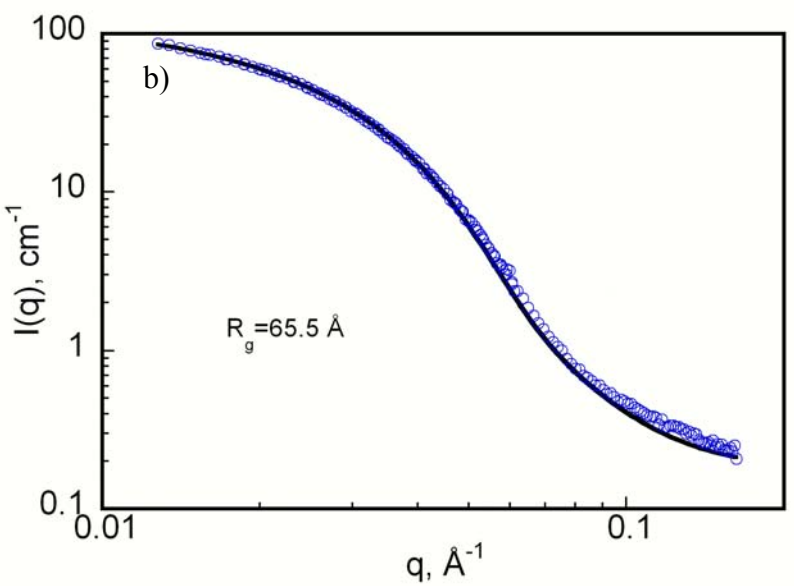

Figure 5.3. SANS curves for 5 wt% a) 35-BDMS and b) 32-BDMS nanoparticles blended with linear PS (Mn, 21k) at 100 ^{o}C. The solid lines are the RPA fits by equation 5.5 with Rg(dPS) of 39 Å, ξ of 26 Å, ν of 1/3 .

Table 5.1. Size of nanoparticles from RPA and Guinier fitting

Nanoparticles	$R_{Collapse}$ ($Rg_{collapse}$), Å	$R_{g\ Bulk\ blends}$, Å (5wt %)		
			Guinier	RPA
35-BDMS	57.8 (44.8)	25 °C	60.3±1.0	65.8±1.0
		100 °C	59.6±1.0	67.9±1.0
		120 °C	60.0±1.0	68.5±1.0
		140 °C	60.3±1.0	68.9±1.0
32-BDMS	59.3 (45.9)	25 °C	63.5±1.0	63.6±1.0
		100 °C	64.1±1.0	65.5±1.0
		120 °C	64.1±1.0	66.9±1.0
		140 °C	64.5±1.0	65.3±1.0
		175 °C	66.2±1.5	68.1±1.0
35-OH	59.5 (46.1)	25 °C	60.0±1.0	67.0±1.0
		100 °C	59.5±1.0	71.9±1.0
		120 °C	59.7±1.0	70.4±1.0
		140 °C	59.9±1.0	71.4±1.0
32-OH	59.5 (46.1)	-	-	-
16-OH	44.0 (34.1)	25 °C	53.1±1.0	48.1±2.0
		100 °C	52.5±1.0	49.5±2.0
		120 °C	51.9±1.0	49.6±2.0
		140 °C	51.5±1.0	50.6±2.0
29-OH	46.1 (35.7)	-	-	-

Flory interaction parameter

Flory interaction parameter, χ was originally assumed to arise from purely enthalpic interactions, namely from differences in the energy of interactions between segments of the two species. However significant composition dependencies in χ are often measured experimentally. Moreover, the temperature dependence is usually not consistent with a purely enthalpic excess free energy. Fredrickson et al.[112] have studied the entropic corrections to the Flory-Huggins theory of polymer blends of chemically identical linear and star homopolymers. They found out that when $(f-3)(R_{linear}/R_{arm})^2 >> 1$, i.e., for large numbers of short arms or large homopolymers, and for composition not close to $\phi = 1$, the interaction density, α_E equals:

$$\alpha_E = \frac{1}{64\pi\sqrt{2}} \frac{(f-3)^{3/2}}{(1-\phi)^{1/2} R_{arm}{}^3} \qquad \text{eq. 5.7}$$

Where α is invariant to the choice of segment volume, is related to the more commonly used interaction parameter χ by $\chi = \alpha_E (v_1 v_2)^{1/2}$, where the v_i are the statistical segment volumes for the two blend component and R_{linear} and R_{arm} are the radii of gyration for the linear polymer and individual arm, respectively.

From this expression, it is clear that the entropic contribution to the interaction density for a linear/star blend increases as the 3/2 power of the number of arms of the star (for large f) and is inversely proportional to the cube of the arm radius of gyration. Londono et al.[126] studied the deuterium labeling contribution to χ, and found χ HD for polystyrene is $0.2/T - 2.9\times10^{-4}$ over the range of 158-215 ºC. Based on this equation at 140 °C, the χ value for H/D is ca. 1.9×10^{-4} for the linear/linear blend.

In our case, the star/linear blend is (7-20) $\times 10^{-3}$ suggesting contributions due to chain architecture and molecular weight differences is significantly higher than the effective χ value due to isotopic substitution. The contribution to χ ascribable to architecture effects is in good agreement with the value calculated based on Frederickson theory which is 5.3×10^{-3} with number of arms f=50, Mw=530000 g/mol, ℓ =6.9Å, v_0=99.05 cm^3/mol.

Table 5.2. SANS data for miscibility study of 21k PS with 5 wt% nanoparticles

Nanoparticles	χ at different temperature, °C				
	23	100	120	140	175
35-BDMS	0.0084	0.0117	0.0119	0.0122	-
35-OH	0.0085	0.0124	0.0127	0.0127	-
32-BDMS	0.0065	0.0077	0.0075	0.0078	0.0079
16-OH	0.0169	0.0181	0.0190	0.0198	-

5.3.4 Conclusions

Although the model results are not conclusive, as the BDMS and OH end group contributions to χ were not considered, it is clear that the contribution of chain architecture to χ for the star/linear blends is significantly larger than the isotopic substitution and is in surprisingly good agreement with an approximate prediction from a mean field theory. The value of χ for a blend of hydrogenous 50 arm star (Mw~500000 g/mol) with deuterated linear polystyrene (Mw~20000 g/mol) is in the range of (7-20) $\times 10^{-3}$ over 25–175°C for a segment volume of 99.05 cm^3/mol.

CHAPTER 6 DEWETTING OF PURE POLYSTYRENE THIN FILMS AND POLYSTYRENE THIN FILMS CONTAINING NANOPARTICLES

6.1 Overview

Both Barnes[58] and Mackay[59] have shown that nanoparticles can stabilize polymer films against dewetting due to the segregation of the nanoparticles to the Si surface. Fullerenes[58] have radius of about 1nm, while dendrimers[59] have a radii on the order of 1-2.5 nm. The nanoparticles in this work have a radius of gyration less than 10 nm. In order to investigate the general nature of the suppression of dewetting by nanoparticles, polystyrene films on silicon wafers were chosen as a model system, since polystyrene is an ideal polymer for the study of dewetting (as it is easy to work with and widely studied). The dewetting kinetics of pure PS and PS containing nanoparticles were studied by optical microscopy as function of temperature, annealing time, concentration and type of nanoparticles. A novel aspect of this system is that one type of nanoparticles is formed by intra-molecular crosslinking the star molecules at high temperature (~240 °C) in dilute benzyl ether solution. The crosslinked star polymer nanoparticles can be directly compared to the uncrosslinked nanoparticles in terms of miscibility with the linear polystyrene matrix by SANS, in terms of interfacial segregation as monitored by NR and in terms of dewetting behavior by optical microscopy. In a similar way, the effects of end groups were also investigated by these characterization techniques.

6.2 Experiment

Materials

Linear PS (Mn = 21000, PDI = 1.05) and deuterated PS (Mn = 21000, PDI = 1.03) were obtained from Polymer Source Inc. Toluene (DriSolv®) was purchased from EM

Science. Silicon wafers were purchased form Silicon Inc. Star molecules were synthesized by IBM Almaden Research Center as described in Chapter 2. Star polymers used for dewetting experiment were listed in Table 6.1.

Table 6.1. Lists of star molecules for dewetting experiments

Samples	*Mw*	f	R_g, Å in Toluene, 25 °C
35-BDMS (uncrosslinked)	488,000	50	87.5
32-BDMS (crosslinked)	526,000	50	75.4
35-OH (uncrosslinked)	530,000	50	82.7
32-OH (crosslinked)	530,000	50	77.0

Sample preparation

Linear polystyrene containing star polymer nanoparticles was dissolved in toluene (1% w/w), filtered using a 0.2 μm polytetrafluoroethylene filter, and spin-coated onto Si wafers at 3000 rpm for 30s. The resulting films have an approximate thickness of 30 nm. The coated films were then annealed at 160, 175 and 190 °C under N_2 for different time intervals. All the Si wafers were purchased from Silicon Inc. and used as received without any treatment.

Optical microscopy (OM)

The dewetting kinetics of thin films annealed in a Mettler FP-90 hot stage were studied *in-situ* using an Olympus microscope with a Pulnix TMC-7 CCD camera. The magnification was calculated using a MGP-80 standard grating (Newport Corporation) with 80 line pairs per mm.

6.3 Results and discussion

In this chapter, the dewetting of unmodified PS films (for control), the accelerated dewetting by 35-BDMS and the suppressed dewetting behavior by 32-BDMS, 35-OH and 32-OH will be discussed. Due to the repetition of data for 32-BDMS, 35-OH and 32-OH, the suppressed dewetting behavior will be discussed mostly based on 32-BDMS, the others are moved to Appendix A.

The average hole radius can be only measured at the beginning of the dewetting process for many samples due to impingement of hole at longer annealing time. It is true that for some nanoparticles containing samples, there is no problem of impingement due to much slower dewetting kinetics, for consistency, the radial growth of hole was measured on single holes (using ImageJ software; NIH website: http://rsb.info.nih.gov/ij) and was normalized to the averaged radius of holes at the beginning of dewetting to minimize objective error of selection of the different single hole. The averaged radii of holes at the beginning of dewetting as function of concentration of nanoparticles are summarized in Table 6.2 for all samples.

Table 6.2 Averaged radii of holes (R) at the early stage of dewetting

Concentration of nanoparticles, wt%		Radius of holes, Å			
		35-BDMS	32-BDMS	35-OH	32-OH
0	190 °C		35.4±9.0		
	175 °C		22.8±8.0		
	160 °C		16.4 ±5.1		
1	190 °C	26.8±6.0	13.6±3.5	5.8±3.8	2.8±0.9
	175 °C	9.0±4.5	10.1±3.6	3.6±0.6	1.9±1.3
	160 °C	10.5±4.0	7.7±4.2	1.1±0.5	0.9±0.3
2	190 °C	15.5	6.6±4.8	0.9±0.3	1.0±0.3
	175 °C	11.1±5.0	4.1±3.4	0.8±0.5	0.9±0.3
	160 °C	3.3±1.1	1.6±1.1	0.7±0.1	0.8±0.3
5	190 °C	23.0	3.4±0.7	2.6±1.0	2.4±0.3
	175 °C	10.8±3.7	1.8±1.1	1.0±0.4	0.8±0.3
	160 °C	6.6±3.9	0.7±0.3	0.9±0.5	0.8±0.3

6.3.1 Dewetting of unmodified PS films

Figures 6.1a-f are optical images of 30 nm thick pure PS films on silicon annealed at two different time scales at three different temperatures, 160, 175 and 190 °C. Figures 6.1a & 6.1b are optical images of pure PS films annealed for 3 min and 25 min at 190 °C, respectively. Circular holes were formed at the early stages of the annealing (Fig. 1a), the holes then grew and impinged on another, eventually forming the Vornoi pattern characteristic of a fully dewet sample (Fig.6.1b). This is typical scenario of dewetting of pure polystyrene[19].

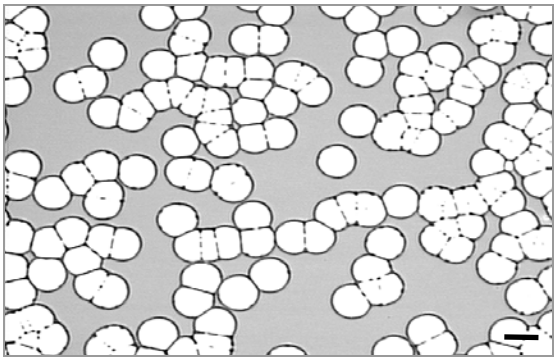

a) 190 °C-3min-(5X)

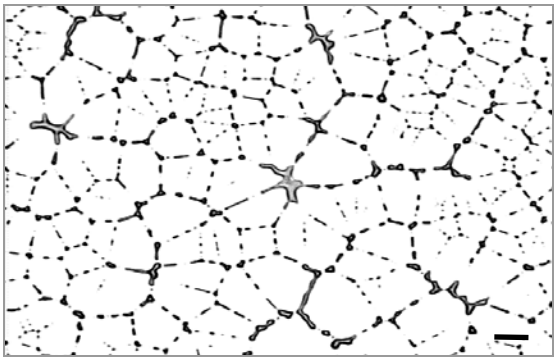

b) 190 °C-25min-(5X)

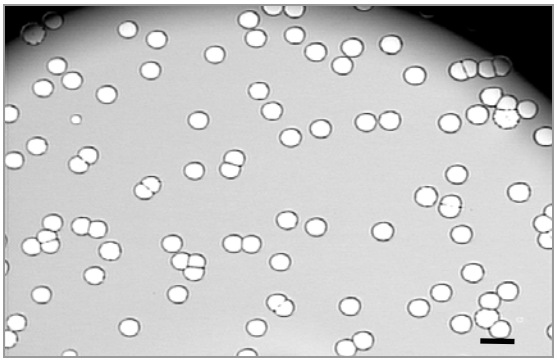

c) 175 °C-3min-(5X)

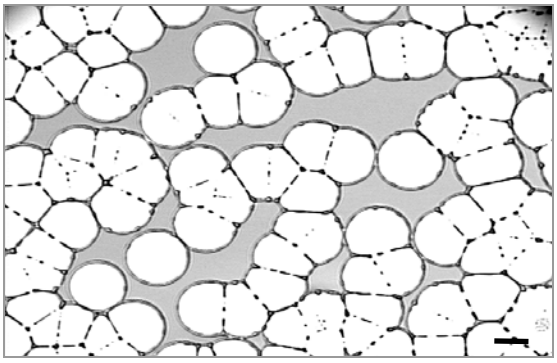

d) 175 °C-25min-(5X)

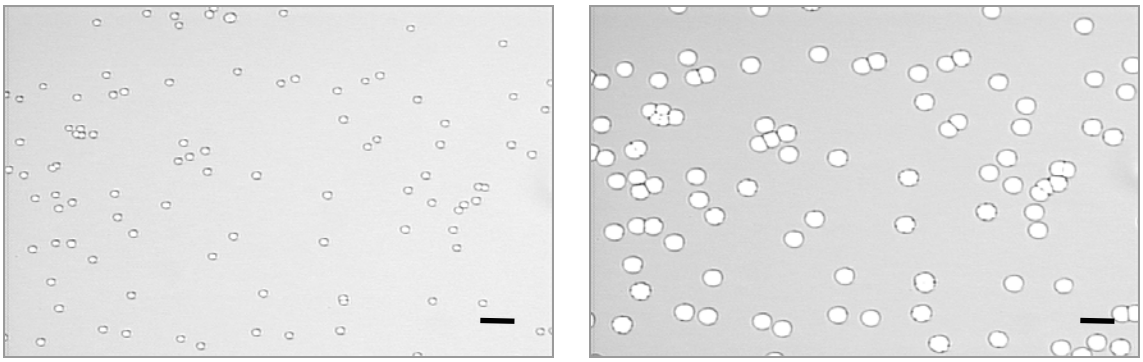

e) 160 °C-3min-(5X) f) 160 °C-25min-(5X)

Figure 6.1. Optical micrographs showing dewet and partially dewet thin polystyrene films at a) 190 °C annealed for 3 min; b) 190 °C annealed for 25 min; c) 175°C annealed for 3 min, d) 175 °C annealed for 25 min; e) 160 °C annealed for 3 min; f) 160 °C annealed for 25min (scale bar = 100μm). The light color areas are the holes.

At lower annealing temperatures, 175 °C, 160 °C, the dewetting process is significantly slower. The dewetting kinetics of pure polystyrene thin films at different annealing temperatures is shown in Figure 6.2.

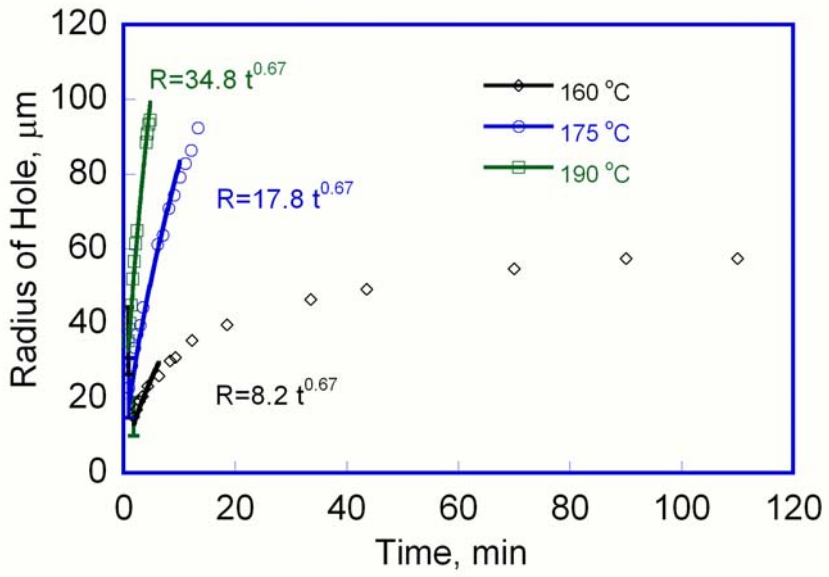

Figure 6.2. Hole growth as function of time for linear PS at different annealing temperatures.

The growth of hole radius (R) in pure polystyrene thin films shows the dependence on annealing time as $t^{2/3}$. This is consistent with theoretical predictions and other experimental observations[18] which showed hole radius growth as $R \propto t^{2/3}$ in a strong slippage regime. This approximation is applicable for very thin liquid "substrate" films or when the substrate is smooth and no strong interaction between substrate and polymers exists so that the polymers melt slips at the substrate surface. Films annealed at lower temperatures show a slower dewetting velocity. Within 5 min, holes in films annealed at 190 °C increased to ~100 μm, while holes in films annealed at 160 °C only increased to ~20 μm. The slower kinetics at the lower annealing temperature is due to the higher viscosity (see Chapter 9).

6.3.2 Dewetting of films containing nanoparticles

6.3.2.1 Accelerated dewetting

Under the same experimental conditions as that for pure PS, 35-BDMS promotes the dewetting process at 2 and 5 wt% (Figure 6.3a-f, 6.5a-f).

Figures 6.3a-f are optical images of 30 nm thick PS films containing uncrosslinked 35-BDMS on silicon annealed at two different time scales, three different temperatures, 160, 175 and 190 °C. Figures 6.3a & 6.3b are optical images of films annealed for 3 min and 25 min at 190 °C, respectively. After 3 minutes at 190 °C, the 35-BDMS filled PS films are almost fully (Figure 6.3a) dewet (as well as films annealed for longer times (10 min) (Figure 6.3b)).

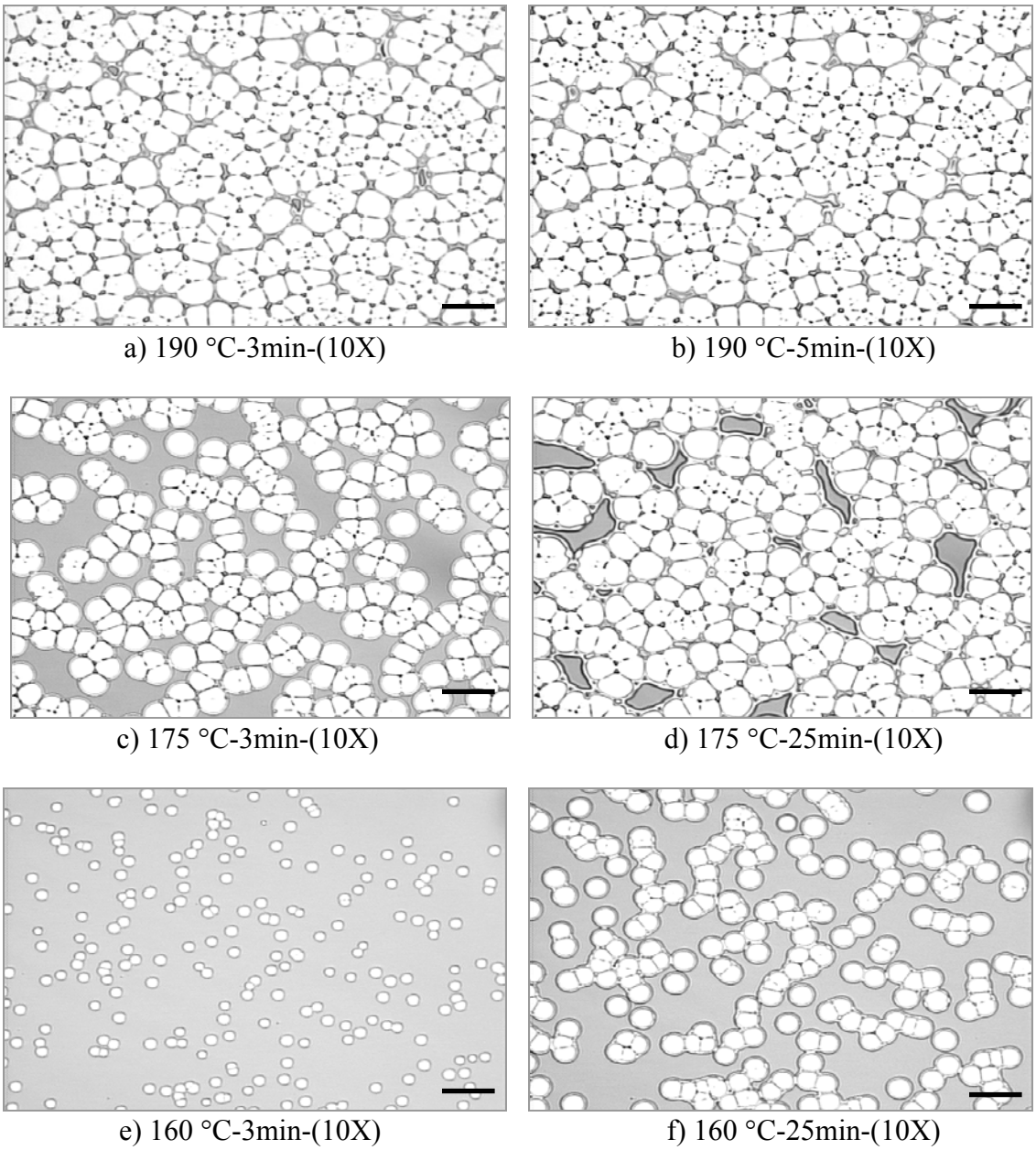

a) 190 °C-3min-(10X) b) 190 °C-5min-(10X)

c) 175 °C-3min-(10X) d) 175 °C-25min-(10X)

e) 160 °C-3min-(10X) f) 160 °C-25min-(10X)

Figure 6.3. Optical micrographs showing fully and partially dewet thin polystyrene films with 5 wt% 35-BDMS at a) 190 °C annealed for 3 min; b) 190 °C annealed for 25 min; c) 175 °C annealed for 3 min, d) 175 °C annealed for 25 min; e) 160 °C annealed for 3 min; f) 160 °C annealed for 25min. (scale bar = 100μm)

The promotion of the dewetting process by uncrosslinked 35-BDMS is consistent with particles enhancing nucleation and subsequent film dewetting[37,38]. The uncrosslinked 35-BDMS probably behaves as a nucleation center and thus enhances the dewetting process.

The hole density in the films containing 35-BDMS (Table 6.3) was increased 10-fold compared to that in pure PS films.

Table 6.3. Number of holes in pure PS films and films containing 5 wt% 35-BDMS

Annealing temperature, °C	Hole density per reference area (0.446 mm^2)	
	PS films	5 wt % uncrosslinked PS-BCB filled PS films
190	44	360
175	25	332
160	24	226

Additional experiments on the dewetting kinetics of uncrosslinked PS-BCB (Figure 6.4) showed a similar dependence of growth of hole on the annealing time ($t^{2/3}$) compared to the dewetting kinetics of pure polystyrene. The increased hole density and the similar dewetting kinetics confirmed the assumption that the uncrosslinked 35-BDMS may act as nucleation center and thus enhance the dewetting process.

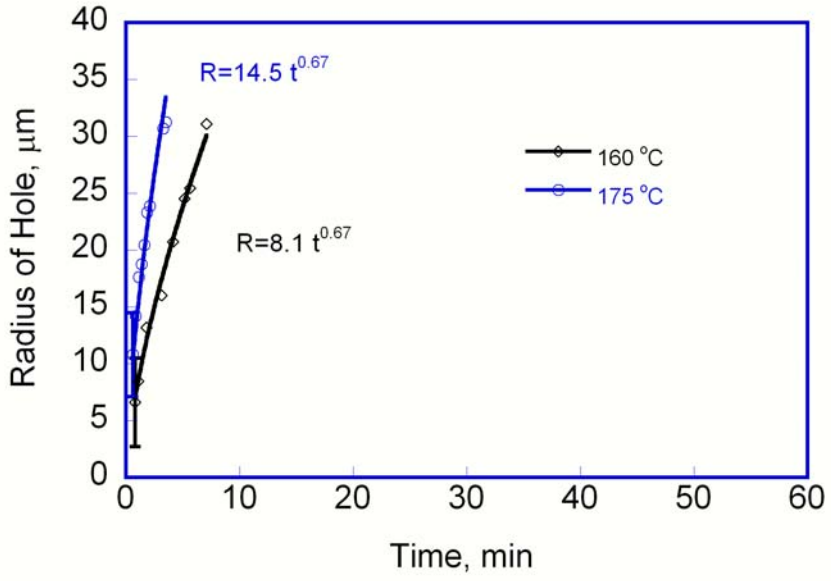

Figure 6.4. Hole growth as function of time for blends with 5 wt% 35-BDMS.

Films with 2% uncrosslinked 35-BDMS showed a similar enhanced dewetting behavior (Figure 6.5 a-f) as the one with 5% 35-BDMS under the same annealing condition. The dewetting kinetics (Figure 6.6) also showed power law dependence of R on t as $t^{2/3}$.

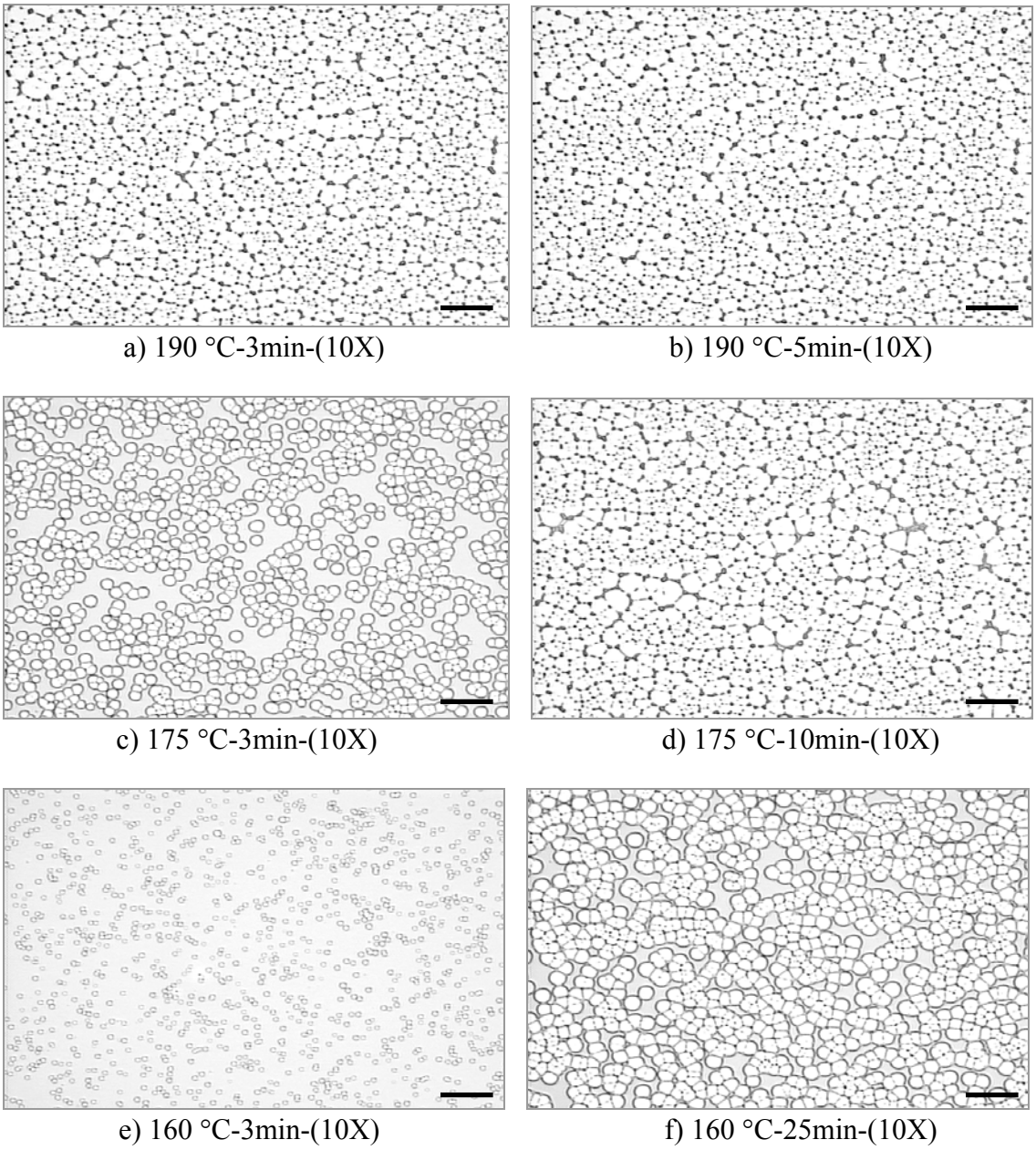

a) 190 °C-3min-(10X) b) 190 °C-5min-(10X)

c) 175 °C-3min-(10X) d) 175 °C-10min-(10X)

e) 160 °C-3min-(10X) f) 160 °C-25min-(10X)

Figure 6.5. Optical micrographs showing fully and partially dewet thin PS films with 2 wt% 35-BDMS at a) 190 °C annealed for 3 min; b) 190 °C annealed for 5 min; c) 175 °C annealed for 3 min, d) 175 °C annealed for 10 min; e) 160 °C annealed for 3 min; f) 160 °C annealed for 25min. (scale bar = 100μm)

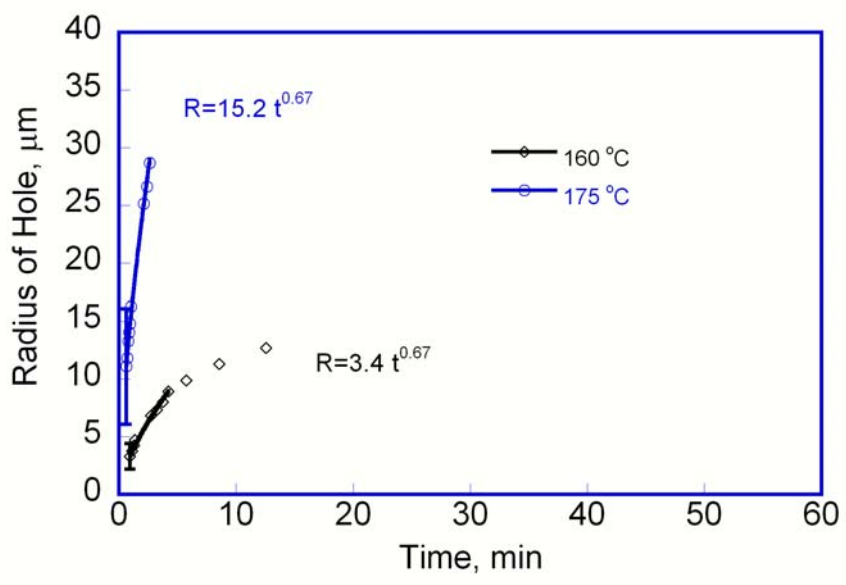

Figure 6.6. Hole growth as function of time for blends with 2% 35-BDMS.

Films with 1% uncrosslinked 35-BDMS did not show obvious suppression or enhancement of dewetting (Figure 6.7 a-f). The dewetting kinetics (Figure 6.8) also showed power law dependence of R on t as $t^{2/3}$ which is similar to that of pure PS.

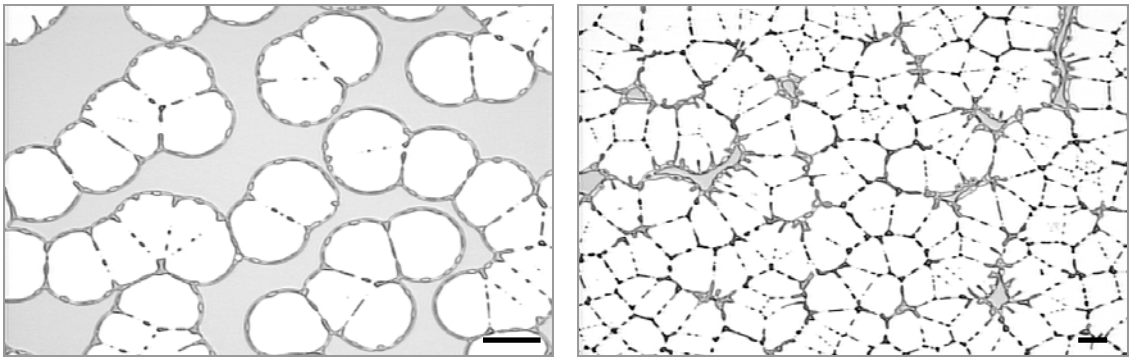

a) 190 °C-3min-(10X) b) 190 °C-25min-(5X)

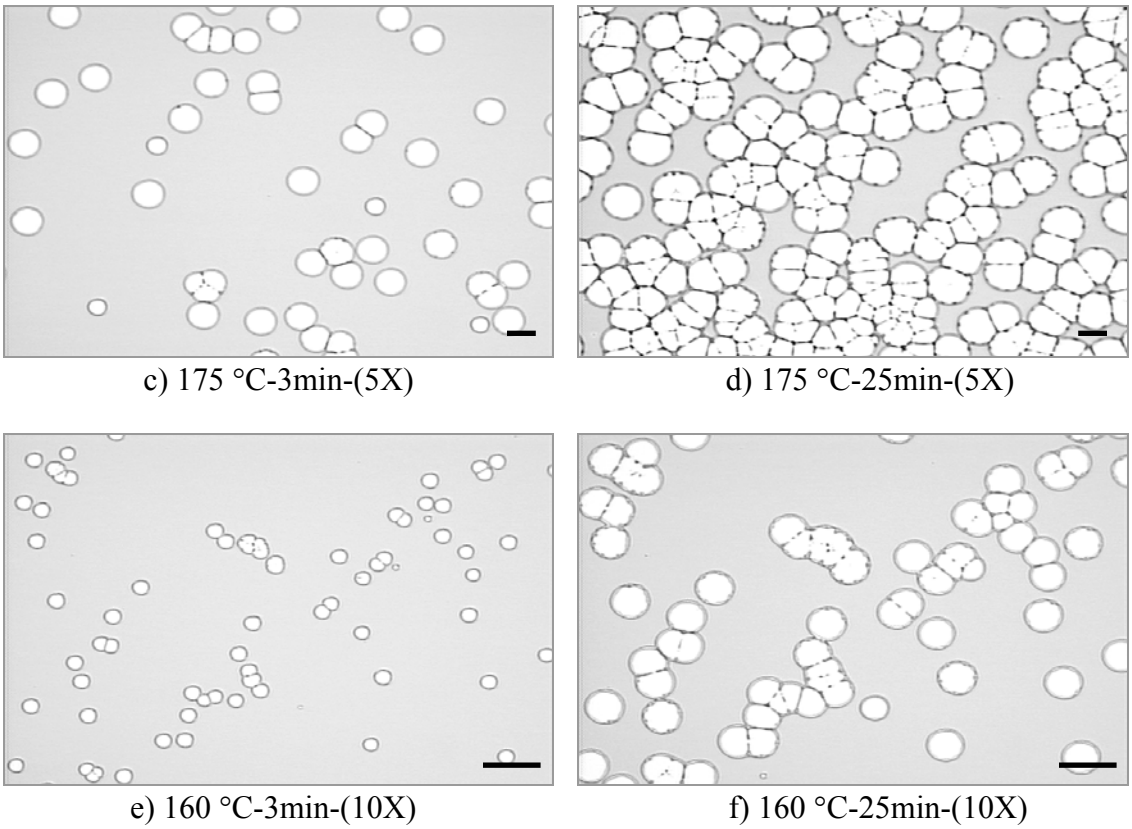

c) 175 °C-3min-(5X) d) 175 °C-25min-(5X)

e) 160 °C-3min-(10X) f) 160 °C-25min-(10X)

Figure 6.7. Optical micrograph showing partially dewet thin polystyrene films with 1 wt% 35-BDMS at a) 190 °C annealed for 3 min; b) 190 °C annealed for 25 min; c) 175°C annealed for 3 min, d) 175 °C annealed for 35 min; e) 160 °C annealed for 3 min; f) 160 °C annealed for 25min. (scale bar = 100μm).

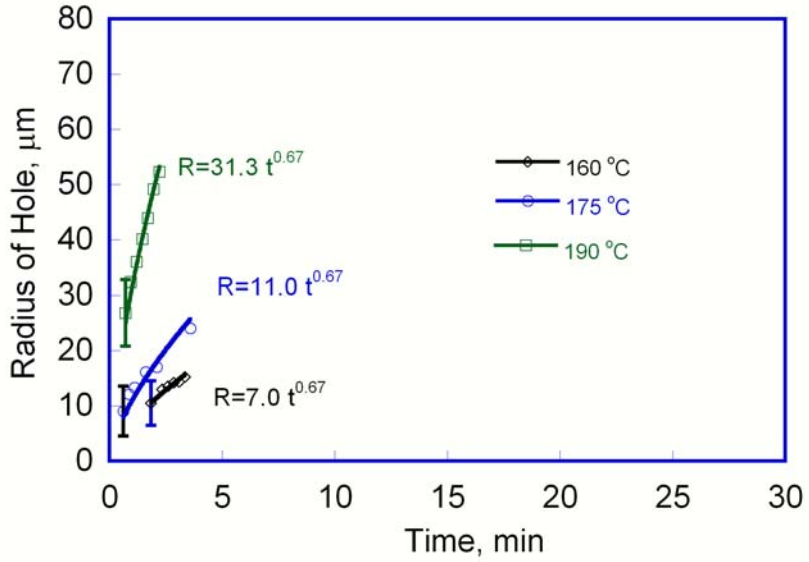

Figure 6.8. The growth of hole as function of time for blends with 1 wt% 35-BDMS.

6.3.2.2 Suppressed dewetting

All films with the other nanoparticles 32-BDMS, 35-OH and 32-OH showed similar suppression dewetting behavior. Here in this section only representative data (mostly 32-BDMS) are discussed.

Figures 6.9a-f are optical images of 30 nm thick PS films containing crosslinked 32-BDMS on silicon annealed at two different time scales, three different temperatures (160, 175 and 190 °C). Compared to uncrosslinked 35-BDMS which showed an acceleration of dewetting, crosslinked 32-BDMS showed obvious suppression of dewetting compared to pure PS.

Optical microscopy of thin films of linear PS blended with 5% crosslinked 32-BDMS showed clear suppression of dewetting behavior. Figures 6.9a & 6.9b are optical images of pure PS films annealed for 3 min and 25 min at 190 °C, respectively. After 3 minutes at 190 °C, the pure linear PS film showed obvious dewetting with the appearance of large circular holes on the order of 50 μm (Fig. 6.1a); the film with 5% crosslinked 32-BDMS also shows the onset of dewetting but with much smaller holes (~4μm) (Figure 6.3a). Further annealing of the linear PS films at 190 °C for 25 min resulted in a Vornoi pattern characteristic of a fully dewet film (Fig. 6.1b), while the film containing 5% crosslinked 32-BDMS only shows a slow growth of holes (~6 μm)(Fig. 6.9b) under the same conditions. In addition, the holes did not continue to evolve and became pinned after reaching a radius of about 14 μm.

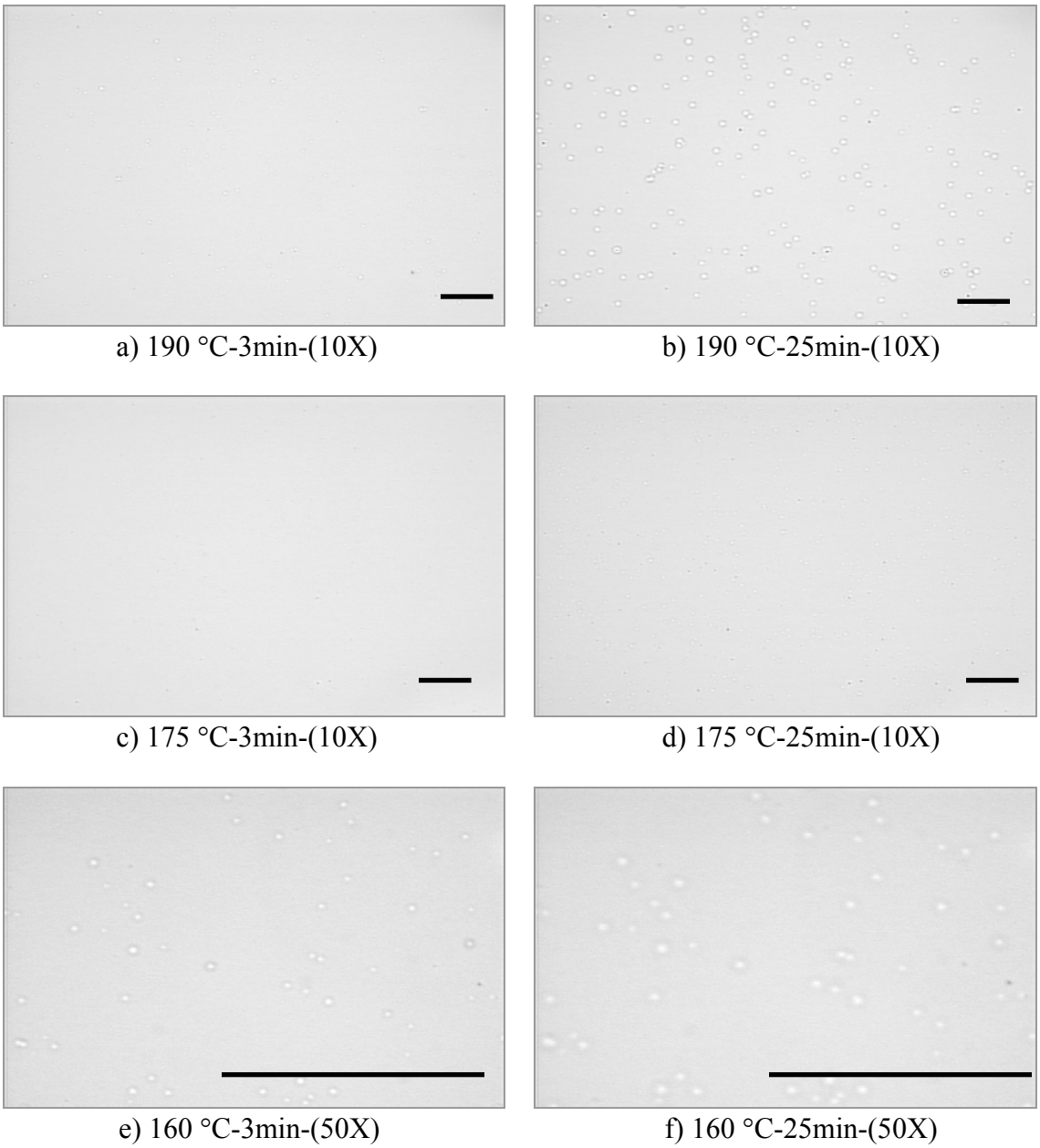

a) 190 °C-3min-(10X) b) 190 °C-25min-(10X)

c) 175 °C-3min-(10X) d) 175 °C-25min-(10X)

e) 160 °C-3min-(50X) f) 160 °C-25min-(50X)

Figure 6.9. Optical micrograph showing partially dewet thin polystyrene films with 5 wt% crosslinked 32-BDMS at a) 190 °C annealed for 3 min; b) 190 °C annealed for 25 min; c) 175 °C annealed for 3 min, d) 175 °C annealed for 25 min; e) 160 °C annealed for 3 min; f) 160 °C annealed for 25min. (scale bar = 100μm)

The dewetting kinetics at different annealing temperatures is shown in Figure 6.10. The kinetics with 5% nanoparticles can also be described by power law. However, it follows the power ranges from 0.10 to 0.36 depending on temperature. This indicates a strong

slippage of the polymer melt at the substrate surface is not applicable for this condition. This may be due to the nanoparticle layer remaining on silicon surface after dewetting as measured by atomic force microscopy (AFM) on the morphology of dewet holes (discussed in Chapter 8). The same suppressed dewetting behavior was observed for films with 35-OH and 32-OH (see Appendix A1 and A2).

Films annealed at lower temperatures also show a slower dewetting velocity. At 190 °C, the hole increased from 4μm to 12 μm within 2 hour, while at 160 °C, the hole growth is barely measurable. Films with low concentration of 32-BDMS annealed at 175, 160 °C also show a slower dewetting velocity (Appendix A3).

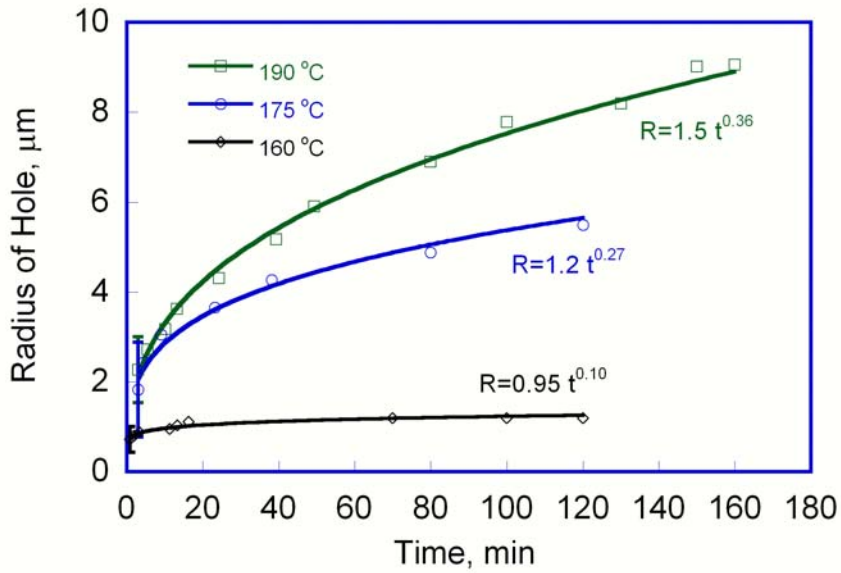

Figure 6.10. Hole growth as function of time for blends with 5 wt% crosslinked 32-BDMS.

In summary, compared to 35-BMDS which enhanced the dewetting of thin films, 32-BDMS suppressed the dewetting of thin films and the dewetting kinetics is different from that of pure PS. This indicates intra-crosslinking of nanoparticles favors the suppression of dewetting. Both Barnes[58] and Mackay[59] indicated that stabilizing polymer films

against dewetting by nanoparticles was due to the segregation of the nanoparticles to the Si surface. Our neutron reflectivity (NR) results also indicate the inhibited dewetting behavior results from strong interfacial segregation of nanoparticles at the polymer/substrate interface. Intra-molecular crosslinking enhanced the segregation of 32-BDMS to the silicon surface and thus 32-BDMS showed a totally opposite dewetting behavior than 35-BDMS which showed only a minor segregation to the silicon surface. This will be discussed in Chapter 7.

Films with the other nanoparticles 35-OH and 32-OH also showed the suppression dewetting behavior (see Appendix A1 and A2).

6.3.2.2.1 Concentration effect

In order to evaluate the concentration effect of nanoparticles on the suppression of dewetting, the dewetting behavior of films containing 1, 2wt% 32-BDMS was also studied. Figure 6.11 and 6.12 are micrographs showing dewetting of PS films containing 2 and 1 wt % 32-BDMS annealed at 190 °C respectively.

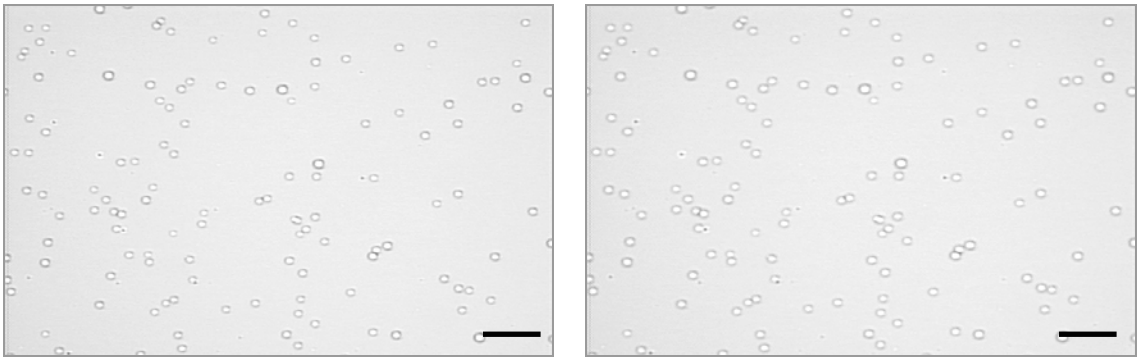

a) 190 °C-3min-(10X) b) 190 °C-25min-(10X)

Figure 6.11. Optical micrographs showing partially dewet thin PS films with 2 wt% crosslinked 32-BDMS at a) 190 °C annealed for 3 min; b) 190 °C annealed for 25 min. (scale bar = 100μm)

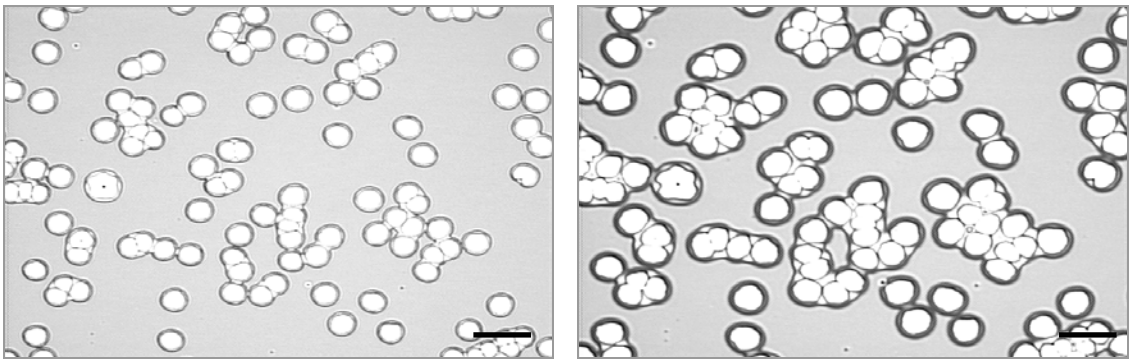

a) 190 °C-3min-(10X) b) 190 °C-25min-(10X)

Figure 6.12. Optical micrographs showing partially dewet thin PS films with 1 wt% crosslinked 32-BDMS at a) 190 °C annealed for 3 min; b) 190 °C annealed for 25 min. (scale bar = 100μm)

Optical microscopy shows films with lower concentration of nanoparticles were less effective in suppressing the dewetting in PS films. The growth of hole as function of time at different concentrations of nanoparticles is shown in Figure 6.13.

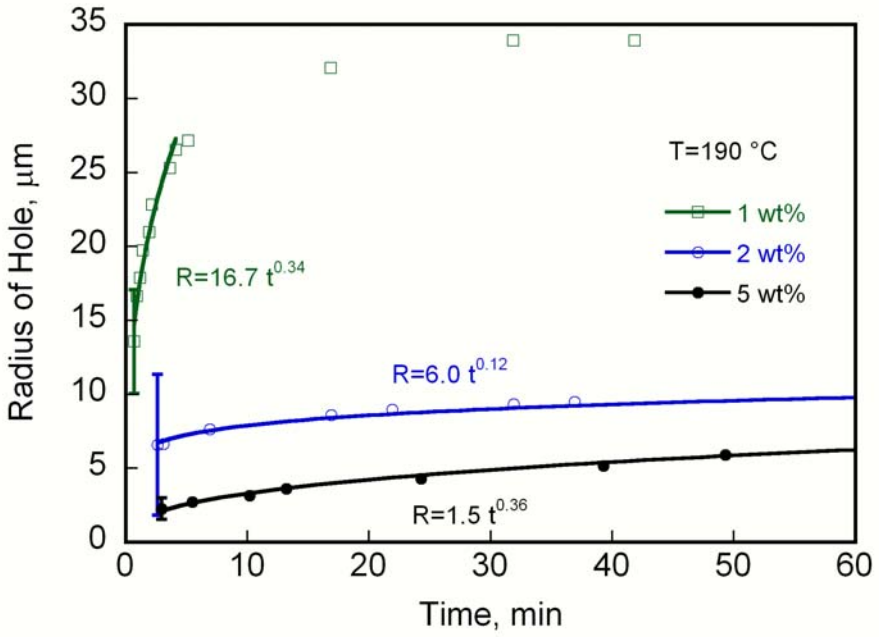

Figure 6.13. Hole growth as function of time for films containing different concentrations of 32-BDMS at 190 °C.

The trend is obvious in Figure 6.13: the lower the concentration, the faster the hole growth. Holes inside films containing 5% 32-BDMS shows a growth of hole up to ~3 μm within 15 min, while holes in films with 1% 32-BDMS increased up to 30 μm. Films with 2% 32-BDMS showed kinetics close to that of films with 5% 32-BDMS. This suggests a critical nanoparticle concentration is essential for effective suppression of dewetting, possibly correlating with either full or partial monolayer coverage (see Chapter 8). Films with the other nanoparticles 35-OH and 32-OH showed the same concentrating effect on dewetting: the lower the concentration, the faster the hole growth (Appendix A1 and A2).

6.3.2.2.2 End group effect

It has been shown that 32-BDMS suppressed the dewetting of thin films. Films with the other nanoparticles 35-OH and 32-OH also showed the suppression dewetting behavior (Appendix A1 and A2). In order to understand the effect of end groups, the dewetting kinetics of films containing 32-OH and 32-BDMS are compared in Figure 6.14.

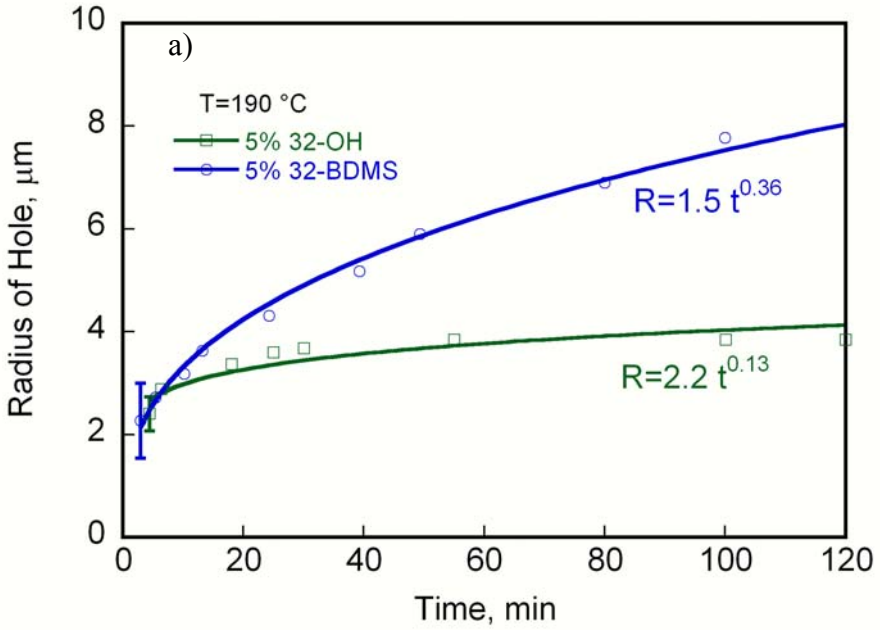

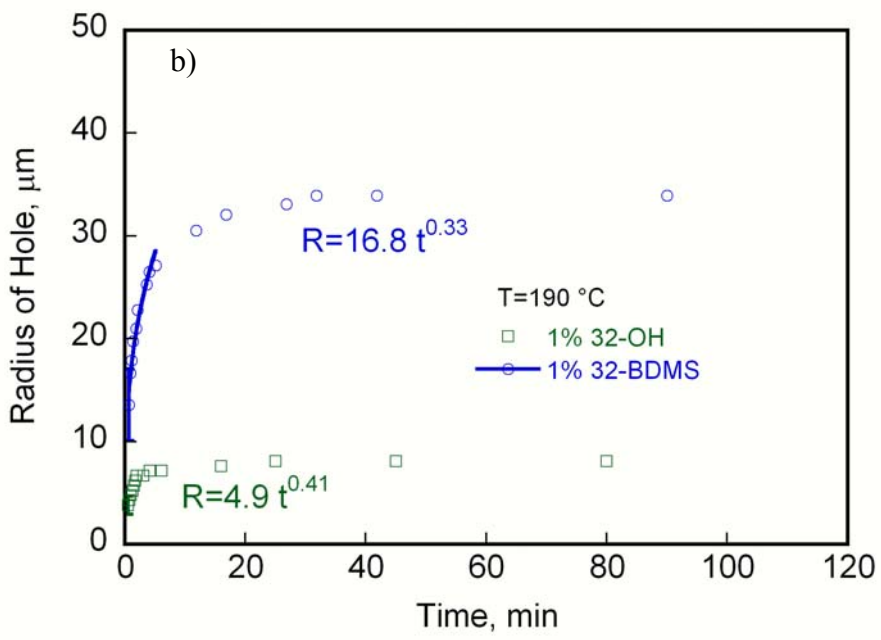

Figure 6.14. Hole growth as function of time for films containing 32-BDMS and 32-OH a) with 5wt% concentration; b) with 1wt% concentration annealed at 190 °C.

At 5wt% (Figure 6.14a), the kinetics for films with 32-OH are slower than that of 32-BDMS. Within 2 hours, the holes only increase from 2 μm to ~4μm, while the hole in the films containing 32-BDMS increases from 2 μm to ~8μm. This indicates 32-OH is more effective in suppression of dewetting that 32-BDMS. The same results were observed at lower concentrations; see for example at 1 wt% (Figure 6.14b). The observed suppression dewetting behavior resulted from the segregation of nanoparticles at the Si/polymer interface as shown by neutron reflectivity in Chapter 7. The observation that 32-OH is more effective is due to the fact that it has a stronger segregation than 32-BDMS as will be discussed in Chapter 7: the stronger segregation of nanoparticles resulted in more effective suppression of dewetting.

6.3.3 Discussion and conclusions

Since the overall dewetting extent depends on the size and number density of holes, the dewetting area fraction, f at a certain dewetting time was used to characterize the dewetting extent. The dewetting percentage f, at a fixed time t was determined by image analysis (using ImageJ software) and is shown in Table 6.4. In order to evaluate the dewetting behavior, the suppression factor, γ (at fixed time) is defined as: $\gamma_{time} = \frac{f_{\text{pure PS}} - f_{\text{PS + PS-BCB}}}{f_{\text{pure PS}}}$ and is used to describe the suppression behavior. For inhibition γ is positive with $\gamma = 1$ for total inhibition of dewetting, for enhanced dewetting behavior γ is negative. The suppression factor at 10 min of dewetting as function of concentration of nanoparticles at 175 °C is shown in Figure 6.15.

Table 6.4. Dewetting percentage for films with different concentration of nanoparticles at 175 °C

Nano%		35-BDMS	32-BDMS	35-OH	32-OH
0 (pure PS)	190°C		95.0		
	175°C		61.0		
	160°C		10.8		
1	190°C	86.0	44.0	16	1
	175°C	65.0	22.0	19	2.2
	160°C	20.4	13.5	2.0	1
2	190°C	100	4.3	1	1
	175°C	100	10	1	2.2
	160°C	62.2	1	1	1
5	190°C	100	1.5	2.4	1
	175°C	80	1.3	1	1
	160°C	48.1	1.2	1	1

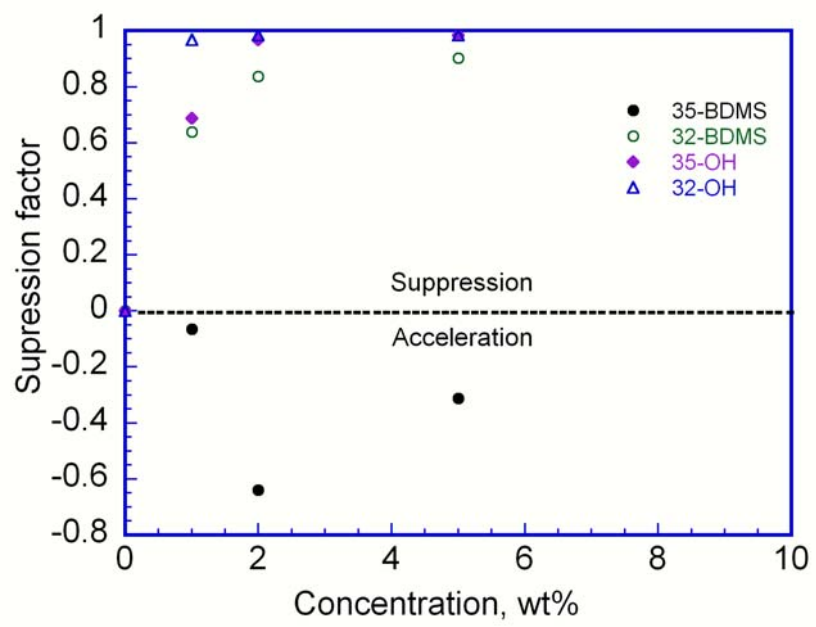

Figure 6.15. Suppression factor as function of concentration of nanoparticles for 10min of dewetting at 175 °C

OH end group and intra-molecular crosslinking favor the suppression of dewetting behavior. Films containing 35-BDMS (uncrosslinked) showed negative suppression factors which means it enhanced dewetting, while films containing 32-BDMS (crosslinked) exhibit a positive suppression factor which means it inhibited the dewetting. Among those three nanoparticles (32-BDMS, 35-OH and 32-OH) which showed suppression dewetting behavior, 32-OH is most effective. It showed obvious suppression even at 1 wt% concentration while 35-OH (uncrosslinked) with 2% and 5% and 32-BDMS with 5 wt% concentration showed similar suppression behavior.

With increasing nanoparticle concentration, the suppression factor is also increased for all three nanoparticles exhibiting suppression dewetting behavior. This suggests the existence of critical concentration for different nanoparticle for the effective suppression of dewetting. This will be discussed in Chapter 8.

CHAPTER 7 NEUTRON REFLECTIVITY

7.1 Overview

Both Barnes and Mackay concluded that the observed suppressed dewetting behavior upon adding nanoparticles was related to the segregation of the nanoparticles to the polymer/Si interface. Neutron reflectivity is a logical experiment to determine the details of any interfacial layer that may form at the silicon surface. Potential questions include whether it forms during the spin casting process or whether there is a diffusion and segregation process that occurs during annealing.

In polymer blends segregation of one component to the surface is often found even if the bulk blend is miscible. A number of factors control the enrichment of the component to the surface. Classic thermodynamic implies the difference in surface energy is the driving force for the segregation.[127] The component with lower surface energy will be enriched at the free surface[128,129,130,131,132]. From a microscopic prospective both enthalpy and entropic factors contribute to this phenomena. The component with lower monomer-monomer attraction is favored at a free surface, since there is less penalty for lack of neighbors at the surface[133]; the species that has strong attraction to a surface will segregate to the surface due to the lowered interfacial energy[134]; the more flexible chain tends to segregate at the surface because of a lower conformational entropic penalty[135,136,137], while the stiffer chain will segregate to surface when surface induced ordering exists[138,139,140]; lower molecular weight polymer will enrich the surface due to the lower entropy loss[141,142,143,144] and localization of chain end groups[145,146,147] at the surface.

Only a few papers have been published on experimental studies of the segregation of star molecules in linear polymer matrices. Foster et al. showed that a six arm star polystyrene with M_w of 157K in linear polystyrene with M_w of 230K preferably segregated to both air and silicon surface due to the branching.[148] This is consistent with the theoretical prediction by Yethiraj[133] for blends of branched and linear polymers where for an athermal system the linear polymers favor at the surfaces. However Wu and Fredrickson argued that the relative molecular weights of the components should also play a significant role in determining which species was segregated to the surface when there is no specific interaction between polymer and the surface.[112]

Neutron reflectivity was used to map the concentration profile through the film thickness of blends of linear PS and crosslinked and uncrosslinked star PS and elucidate the effects of crosslinking, end groups and chain architecture.

7.2 Experiment

Materials

The nanoparticles for NR study are listed in Table 7.1.

Table 7.1. Lists of star molecules for neutron reflectivity

Samples	*Mw*	f	R_g, Å in Toluene, 25 °C
16-OH (uncrosslinked)	215,000	46	60.7
29-OH (crosslinked)	247,000	46	56.3
35-BDMS (uncrosslinked)	488,000	50	82.7
32-BDMS (crosslinked)	526,000	50	77.0
35-OH (uncrosslinked)	530,000	50	87.5
32-OH (crosslinked)	530,000	50	75.4

Sample preparation

Deuterated linear polystyrene (dPS) with 5 wt% crosslinked/uncrosslinked star polystyrene were dissolved in toluene to obtain a 1 wt% solution. Neutron reflectivity samples were prepared by filtering the solution using a 0.2 μm polytetrafluoroethylene filter, and followed by spin-coating onto 100 mm silicon wafers (with native oxide layer) at 3000 rpm for 30s. The resulting films have an approximate thickness of 30 nm as evaluated by ellipsometry.

Neutron reflectivity measurements

NR measurements were performed on the NCNR NG7 reflectometer at NIST. A fixed wavelength of 4.768 Å was used. The intensity of reflected neutrons is measured as a function of momentum transfer ($q = 4\pi\sin\theta/\lambda$, where θ is the angle of incidence and λ is the wavelength). The reflectivity of the as-prepared samples, samples annealed at 140 °C with continuous annealing at 175 °C for another 5 min were measured at room temperature. The scattering length density (SLD) profiles were obtained using Reflfit program provided by NIST website[149].

7.3 Results and discussion

In this section, the reflectivity profiles for blends, the density profile at the film/Si interface, the density profile at the film-air interface and the shape of the nanoparticle in the segregation layer will be discussed. Due to the repetition for reflectivity profile and the scattering length density profile for its fitting for all the nanoparticles, only reflectivity profiles and their fittings for 29-OH, 35-BDMS are shown in this chapter, the others are in Appendix B.

7.3.1 Reflectivity profile

Films containing 29-OH

Reflectivity profiles for samples with 5 wt% crosslinked 29-OH as prepared, annealed 5 min at 140 °C with additional annealing at 175 °C for 5 min are shown in Figure 7.1. The shape of the reflectivity profile is related to neutron scattering length distribution and can be used to calculate spatial distribution of the deuterium[14]. The overall neutron reflectivity curve in Figure 7.1 did not change with additional annealing which indicates there is no much change of the distribution of nanoparticles within the experimental annealing conditions. The periodic fringes (oscillations) in the profile arise from of the reflection from the air/polymer and polymer/Si interfaces and analysis of the fringes allows for determination of the total polymer film thickness, neutron scattering length profile and the roughness of the two interfaces. The dampening of fringes at higher q implies increased roughness at the interfaces.

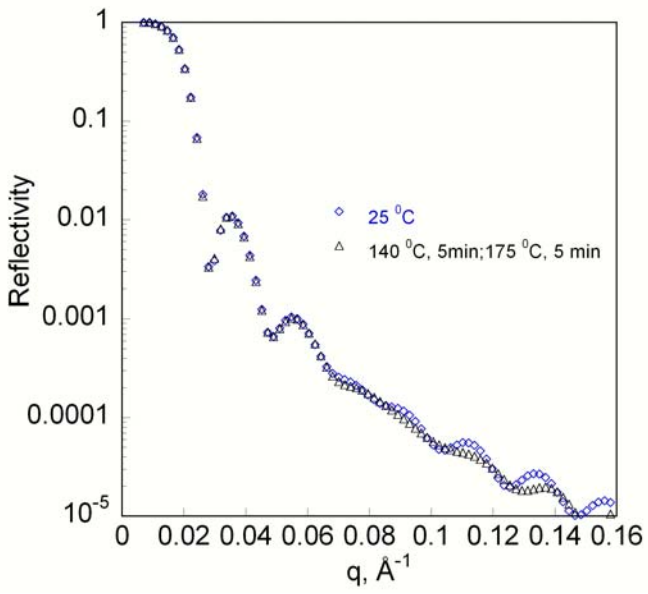

Figure 7.1. Neutron reflectivity for PS blends with 5 wt% crosslinked 29-OH under different annealing conditions.

The solid line in Figure 7.1 is the fit to the NR data for the as-prepared film with the scattering length density profile shown in Figure 7.2 which shows a 3.9 nm segregation layer of crosslinked 29-OH nanoparticles in thicknesses at Si/SiO surface. The SLD values for deuterated PS (dPS), silicon, silicon oxide are (6.65×10^{-6} Å^{-2})[150], (2.10×10^{-6}) Å^{-2} and (2.80×10^{-6}) Å^{-2} respectively, and the stars are assumed to have the same scattering length density as PS (1.42×10^{-6} Å^{-2}). The volume fraction in the segregation layer was calculated as ~41% which was obtained by the SLD difference between segregation layer and pure dPS divided by SLD difference between dPS and PS.

The segregation percentage which is the ratio of the weight of stars in segregation layer to the total weight in the whole film was calculated as 100%. This indicates a strong and complete segregation of crosslinked 29-OH to the Si/SiO surface during spin casting. No detectable segregation to the polymer/air interface was observed.

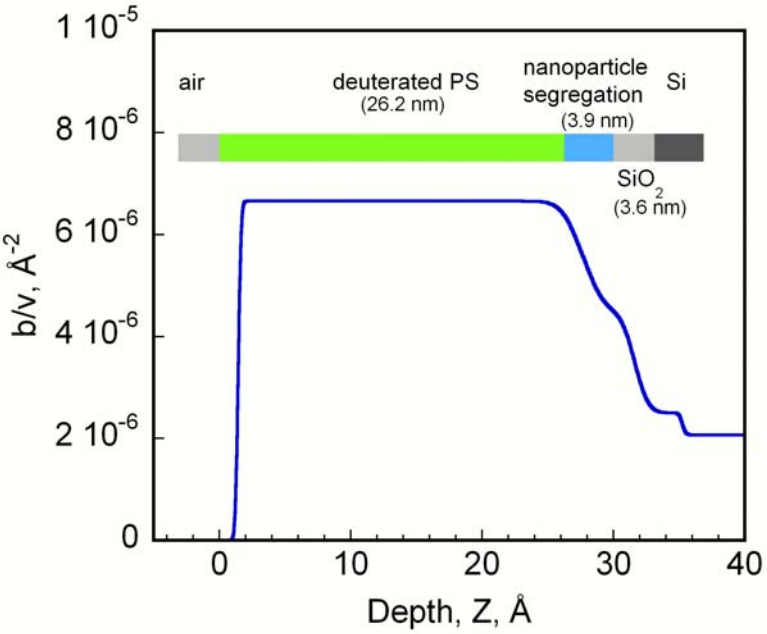

Figure 7.2. Scattering length density profile for neutron reflectivity of as-cast PS film (30 nm) with 5 wt% crosslinked 29-OH showing a 3.9 nm segregation layer of the star at the Si/polymer interface. There was no detectable segregation to the polymer/air interface.

Strong segregation for were observed for the other samples except for 35-BDMS (see Appendix B).

Films containing 35-BDMS

Reflectivity profiles for samples with 5 wt% uncrosslinked 35-BDMS as prepared, annealed 5 min at 140 °C with additional annealing at 175 °C for 5 min are shown in Figure 7.3. The overall neutron reflectivity curve in Figure 7.3 did not change much with additional annealing which indicates there is no much change of the distribution of nanoparticles within the experimental annealing conditions. The dampening of fringes at higher q implies increased roughness at the interfaces.

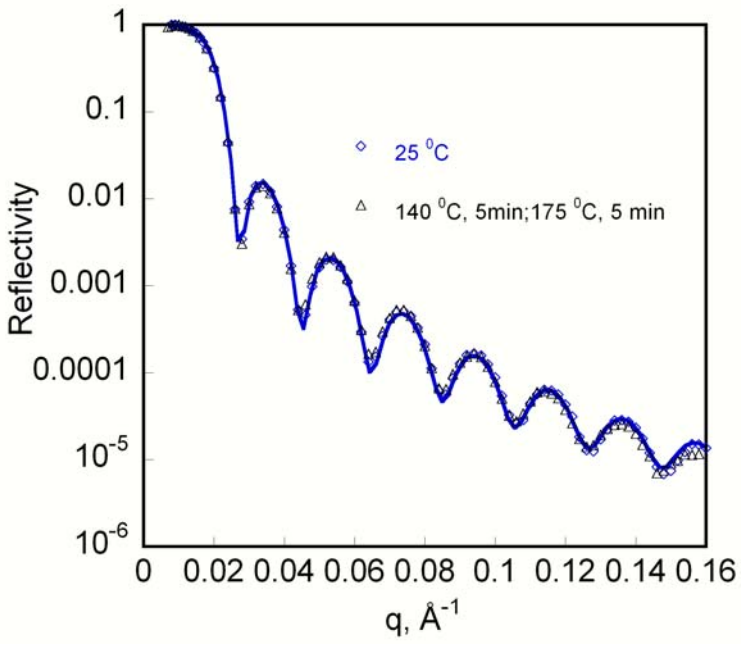

Figure 7.3. Neutron reflectivity for PS blends with 5 wt% uncrosslinked 35-BDMS under different annealing conditions.

The solid line in Figure 7.3 is the fit to the NR data for the as-prepared film with the scattering length density profile shown in Figure 7.4 which shows a 11.4 nm segregation layer of crosslinked 35-BDMS nanoparticles in thicknesses at Si/SiO surface. The SLD

values for deuterated PS (dPS), silicon, silicon oxide are (6.65×10^{-6} Å^{-2}), (2.10×10^{-6}) Å^{-2} and (2.80×10^{-6}) Å^{-2} respectively, and the stars are assumed to have the same scattering length density as PS (1.42×10^{-6} Å^{-2}). The volume fraction in the segregation layer was calculated as ~7% and the segregation percentage was calculated as 49%. This indicates a very weak segregation of uncrosslinked 35-BDMS to the Si/SiO surface during spin casting. No detectable segregation to the polymer/air interface was observed.

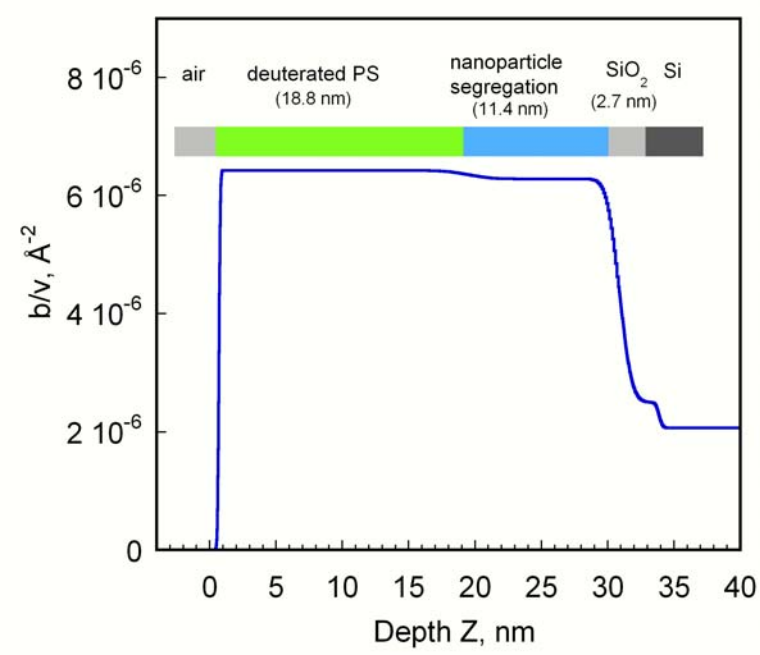

Figure 7.4. Scattering length density profile for neutron reflectivity of as-cast PS film (30 nm) with 5 wt% uncrosslinked 35-BDMS showing an 11.4 nm segregation layer of the star at the Si/polymer interface. There was no detectable segregation to the polymer/air interface.

The segregation layer thickness, L, the volume fraction of stars within this layer, and segregation percentage at different annealing conditions for all samples are listed in Table 7.2.

Table 7.2. Characteristics of segregation layers

Nanoparticles	25 ºC			175 ºC		
	L, nm	v%	Segregation %	L, nm	v%	Segregation %
35-BDMS	11.4	7.1	49	9.7	9.8	59
32-BDMS	6.2	21.5	83	5.7	27.3	100
35-OH	6.2	23.5	91	6.1	23.5	91
32-OH	5.2	32.7	100	5.3	32.6	100
16-OH	4.6	33.8	100	4.6	33.8	100
29-OH	3.9	41.7	100	3.9	41.7	100

Clearly, all films containing stars shows a strong segregation (~21-41v%) of stars during spin casting except uncrosslinked 35-BDMS which shows only minor segregation (~7 v%). With more annealing, films filled with stars containing BDMS show minor enhanced enrichment, while segregation of other samples did not change since complete segregation (100%) most likely occurs during spin casting.

7.3.2 Density profile at the film/Si interface

All star molecules in Table 7.2 show segregation to the Si/SiO surface. The polar nature of the BDMS/OH end group probably provides an attractive interaction between the star molecules and the Si surface. In addition to a positive χ at room temperature due to deuteration[126], the Flory interaction parameter between linear and star molecules also has contributions from the end groups, the chain architecture difference[124] between the molecules as well as any crosslinking in crosslinked stars filled blends[119,151]. The surface segregation favoring the star polymers at polymer/Si interface is driven by both the

attraction between Si surface and star molecules and any penalty resulting from the unfavorable interaction parameter χ. Thought it should be noted that the system is still single phase in bulk under the experimental conditions as shown by SANS.

The magnitude of surface segregation will depend on the relative strength of polymer-polymer interaction and polymer-surface attraction[133]. The uncrosslinked 35-BDMS (no OH end groups) showed weakest segregation (7%) to the Si/SiO surface. This indicates the segregation of stars due to architecture alone is small since a minor positive effect of BDMS on the segregation is expected. However, 35-OH (uncrosslinked, OH groups) showed a much stronger enrichment (23%) at the Si/SiO surface. This is consistent with a prediction by Freed for a system with asymmetric surfaces where a relatively stronger substrate-polymer attraction will give rise more surface enrichment of this component.[134] Compared to uncrosslinked 35-BDMS, the corresponding crosslinked 32-BDMS also showed a stronger segregation at the Si/SiO surface. Again, this observation follows the prediction that higher positive value of the effective interaction parameter χ due to crosslinking will result in higher surface enrichment of the preferentially absorbed component to the surface[152,153]. In summary, OH end group and intra-molecular crosslinking enhanced the segregation of the stars to the silicon surface.

7.3.3 Density profile at the film-air interface

No star enrichment was observed at the film-air interface (Table 7.2). The deuterium labeling of the linear polystyrene lowers the surface energy of the polymer and thus favors deuterated linear PS enrichment at the air surface[154,155]. Molecular weight disparity can also give rise to segregation of lower molecular weight polymer to the air surface if both polymers are linear.[141-144] It is worthwhile to mention that although our

results are contrary to Foster's finding[148], which showed the star molecules segregated to the air surface, it does follow Wu and Frederickson's prediction[124] for a blend with stars having arms of the same molecular weight as its linear matrix. They studied the surface segregation behavior of star-linear blends composed of the same type of monomer which eliminates the local packing effects as all species have the same segment stiffness. They found that both branching and molecular weight play an important role in determining which species will segregate to the air surface. In particular when the arms of star are the same size as the linear polymer, they predicted that the linear molecules are enriched at the air surface which is consistent with our observations.

7.3.4 Shape of nanoparticles in segregation layers

The thickness of segregation layer (L) in the films (Table 7.2) is almost 50 % smaller than the size of the stars ($2R_g$) based on Guinier fitting from SANS curve of blends with 5 wt% stars (see Chapter 5), except for the film with uncrosslinked 35-BDMS (Table 7.3). This implies a strong interaction between stars and the Si/SiO surface exists and the star molecules within the segregation layer are compressed. This is consistent with the finding of Sheiko et al.[156] which showed an ellipsoidal shape for arborescent graft polystyrenes in monomolecular films cast on mica due to the interaction of the molecules with the substrate. Based on the assumption that the segregation layer is a monolayer, the percent compression, $100L/(2\times R_g)\%$ is calculated (Table 7.3). Molecules show a compression percent in the range of 50-60% except for uncrosslinked 35-BDMS (9%) with no OH group.

Table 7.3. Size of nanoparticles and percent of compression*

Nanoparticles	R, nm	R_g, nm	Percent of compression, %
	Collapse	Guinier	
35-BDMS	5.8	6.0	9
32-BDMS	5.9	6.4	52
35-OH	6.0	6.0	49
32-OH	6.0	-	58
16-OH	4.4	5.3	57
29-OH	4.6	-	61

*Same radii of gyrations in bulk as their corresponding uncrosslinked ones were assumed for crosslinked 32-OH and 29-OH.

In summary, segregation of the star polymers to the silicon surface was observed upon spin casting a mixture of star polymers and linear polystyrene. The segregation is not due to either the bulk immiscibility of the system (as indicated by SANS, see Chapter 5) or surface energy change at the air/polymer interface (as shown by contact angle measurements, see Chapter 4). The surface segregation favoring the star polymers at polymer/Si interface is due to the attraction between Si surface and star molecules and the enthalpic penalty resulting from any unfavorable interaction parameter χ. OH group and crosslinking play an important role in controlling the magnitude of segregation while the chain architecture difference only plays a minor role on the segregation. Detailed analysis shows molecules in the segregation layer are squeezed which implies relatively strong interactions between the molecules and the Si/SiO surface.

7.3.5 Discussion and conclusions

Based on the above information, strong segregation was observed for both OH and BDMS nanoparticles at the Si/polymer interface for as-cast PS films containing 5 wt% nanoparticles (except 35-BDMS which showed only minor segregation).

Dewetting experiments showed that 35-BDMS showed enhanced dewetting behavior, while all the other three nanoparticles showed obvious suppression dewetting behavior. This indicates strong segregation is essential for the observed suppression dewetting behavior which is consistent with the findings by Barnes and Mackay where the observed suppression of dewetting is due to the segregation of the nanoparticles to the interface of polymer/Si. Based on dewetting experiment results in Chapter 6 and the NR results in this chapter, it also suggests the stronger the segregation, the more effective the suppression of dewetting.

From the NR experiments (Table 7.2), in terms of both the segregation percentage and the volume fraction of nanoparticles in the segregation layer, the order of segregation extent is 32-OH, 35-OH and 32-BDMS. Among those three nanoparticles, 32-OH shows the strongest segregation with a volume fraction of ~33% in the segregation layer for complete (100%) segregation, while 32-BDMS shows the weakest segregation with a volume fraction of ~22% of nanoparticles in the segregation layer for 83% segregation. In between, the volume fraction of 35-OH in the segregation layer is ~24% for 91% segregation. The dewetting experiment also shows the order of suppression behavior is also 32-OH, 35-OH and 32-BDMS in terms of suppression factor (Figure 6.15). 32-OH is the most effective in suppression of dewetting among those three nanoparticles (32-BDMS, 35-OH and 32-OH) which showed suppression dewetting behavior. It showed obvious suppression even at 1 wt% concentration while 35-OH (uncrosslinked) at and above 2% concentration and 32-BDMS at 5 wt% concentration showed similar suppression behavior.

CHAPTER 8 ATOMIC FORCE MICROSCOPY

8.1 Overview

Atomic force microscopy (AFM) can provide surface morphology information with a resolution in Å in the direction perpendicular to the surface and in nm in plane. The morphology of the film and the hole structure after dewetting was studied by AFM.

Henn et al[47] studied the dewetting of thin films of end-functionalized polystyrene (ω and α,ω-barium sulfonato-polystyrene-PS$(SO_3)_2$Ba) on silicon, and showed that after dewetting the silicon surface was still covered by a monolayer of chains due to adsorption via their ionic end groups. The segregation layer at the polymer/Si interface as observed by NR in this work suggests that after dewetting there may be also a layer of polymer on the Si surface. AFM was employed to visualize the hole morphology and the depth of hole in the dewet films.

8.2 Experiment

A molecular Imaging PicoPlus AFM (Figure 8.1) was used to study the surface features of the polymer films. The measurements were performed with silicon tips with an apex radius 10 nm in tapping mode.

Figure 8.1. Digital picture of Molecular Imaging AFM

The resonance of the frequency of the tips was 60-90 kHz, and the force constant was 1.2-5.5 N/m.

8.3 Results and Discussion

8.3.1 Surface morphology before dewetting

Figures 8.2a-d showed typical AFM scans for a 4 by 4 μm^2 area for samples of pure PS and PS with 1, 5, 18% 35-OH. It was observed that rms (root mean square) value of the roughness did not increase upon addition of nanoparticles. The average rms value is approximately 6-8 Å which means that the surfaces of spin cast films are very flat.

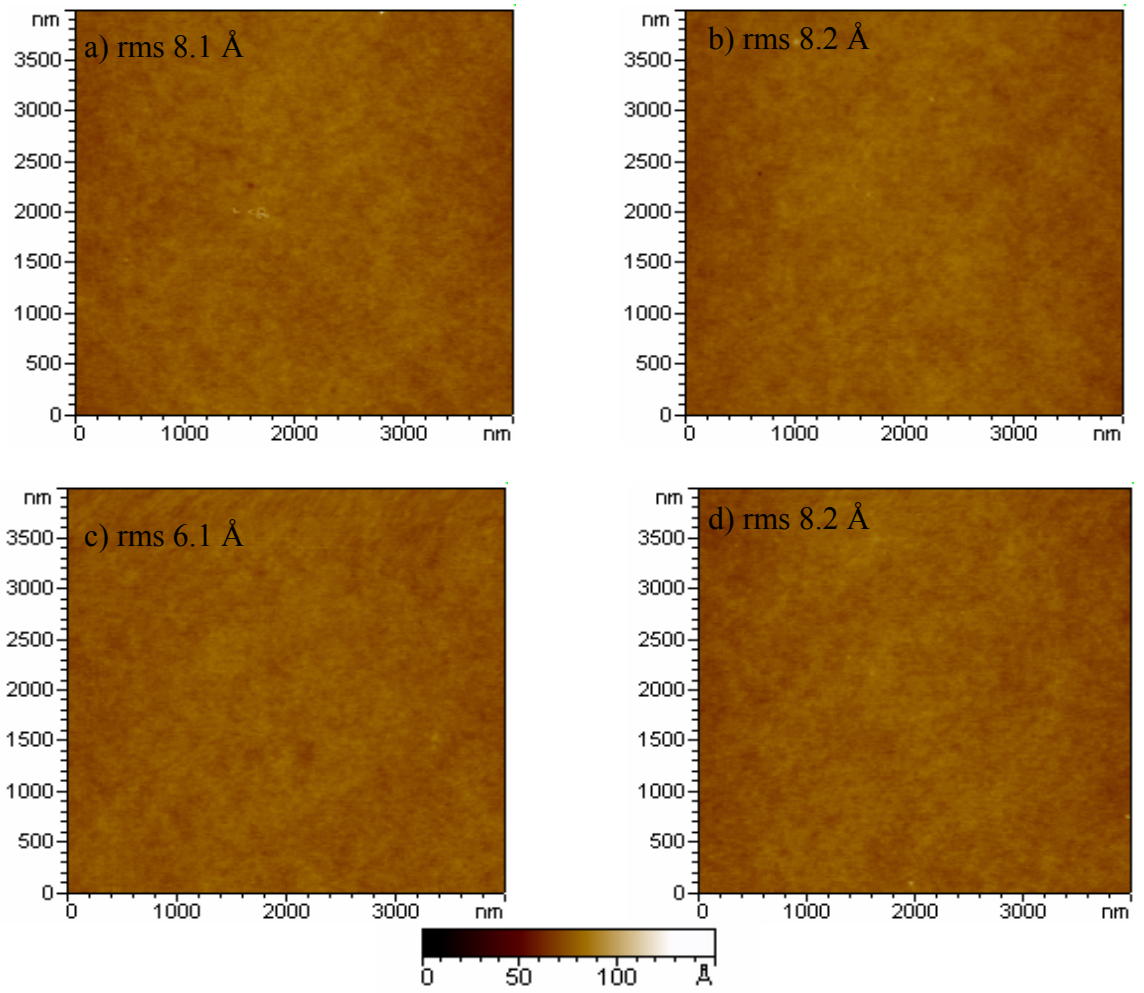

Figure 8.2. Surface morphology of a) pure PS; b) PS with 1 wt% 35-OH; c) PS with 5 wt% 35-OH; d) PS with 18 wt% 35-OH.

8.3.2 Hole morphology after dewetting

In this section, the morphology of pure PS film, the hole morphology in films with enhanced dewetting behavior and the hole morphology in films with suppressed dewetting behavior as function of nanoparticles concentration will be discussed. Due to the repetition of data for films with suppressed dewetting behavior (32-BDMS, 32-OH, 35-OH), only data for 32-BDMS is shown here, the others are moved to Appendix C.

8.3.2.1 Pure PS film

Figure 8.3a shows a 15 μm diameter hole in a pure PS film at the early stage of annealing. The line scan analysis of this hole (Figure 8.3b) shows the hole depth is 30 nm (same as film thickness). This indicates the hole goes through to the Si substrate.

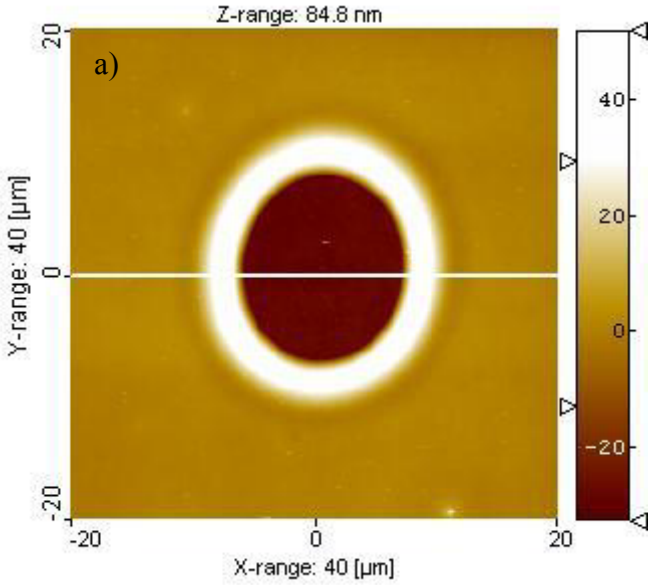

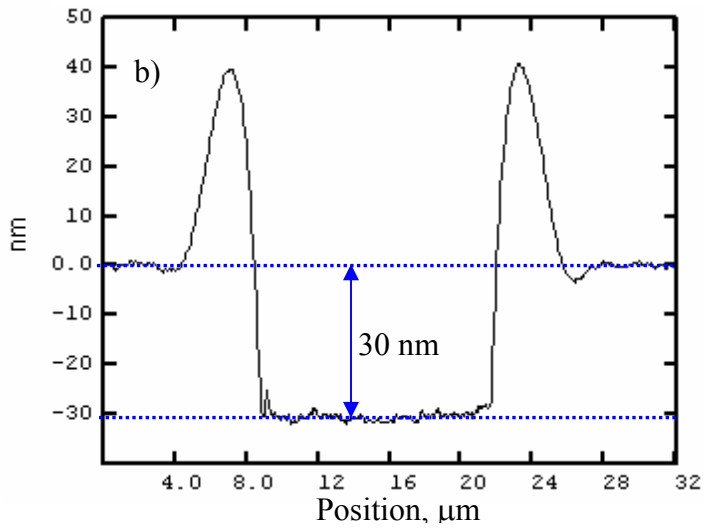

Figure 8.3. a) AFM topography image showing a 15 µm diameter hole in a 30 nm PS film at the early dewetting stage; **b)** section analysis of the hole in Figure 8.3a showing the hole depth of ~30 nm.

8.3.2.2 Films containing nanoparticles

Films with enhanced dewetting behavior

Films containing 5% 35-BDMS showed enhanced dewetting behavior. The same hole morphology is expected due to the fact that same dewetting kinetics as that of pure PS was observed (Chapter 6). Figure 8.4a shows a 20 µm diameter hole in a PS film containing 5% 35- BDMS at the early stage of annealing.

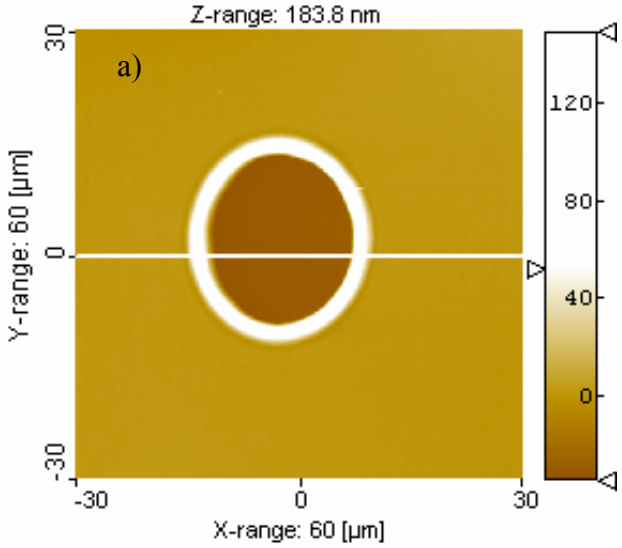

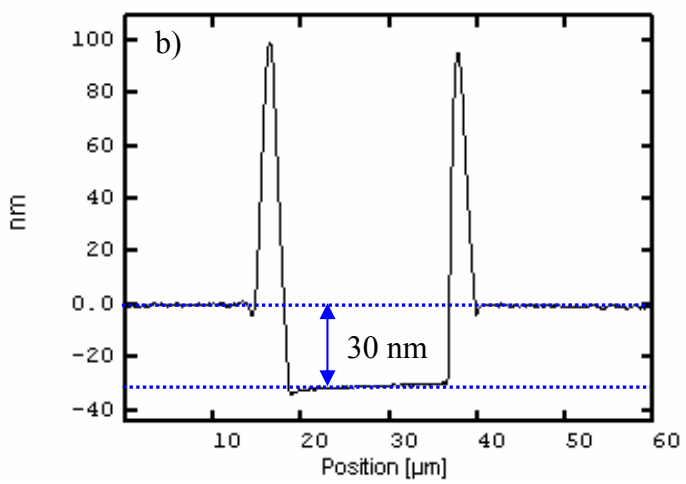

Figure 8.4. a) AFM topography image showing a 18 µm diameter hole in a 30 nm PS film with 5% 35-BDMS at the early dewetting stage; **b)** the line scan analysis of the hole in Figure 8.4a showing the hole depth of ~30 nm.

The line scan analysis of this hole shows the hole depth is ~30 nm (Figure 8.4b) indicating the hole goes through to the Si substrate. This is consistent with the fact that the dewetting kinetics of films containing 35-BDMS is the same as that of pure PS film with strong slippage of the polymer melt on the silicon.

Films with suppressed dewetting behavior

Films containing 32-BDMS, 35-OH and 32-OH showed suppressed dewetting behavior as discussed in Chapter 6.

Figure 8.5a shows a ~30 µm diameter hole in a PS film containing 5% 32-BDMS annealed at 190 °C for 160 min. The line scan of this hole shows a hole depth of 24 nm (Figure 8.5b). This indicates there is still a ~6 nm layer of polymer on the Si substrate, which is in good agreement with the segregation layer observed by NR in Chapter 7.

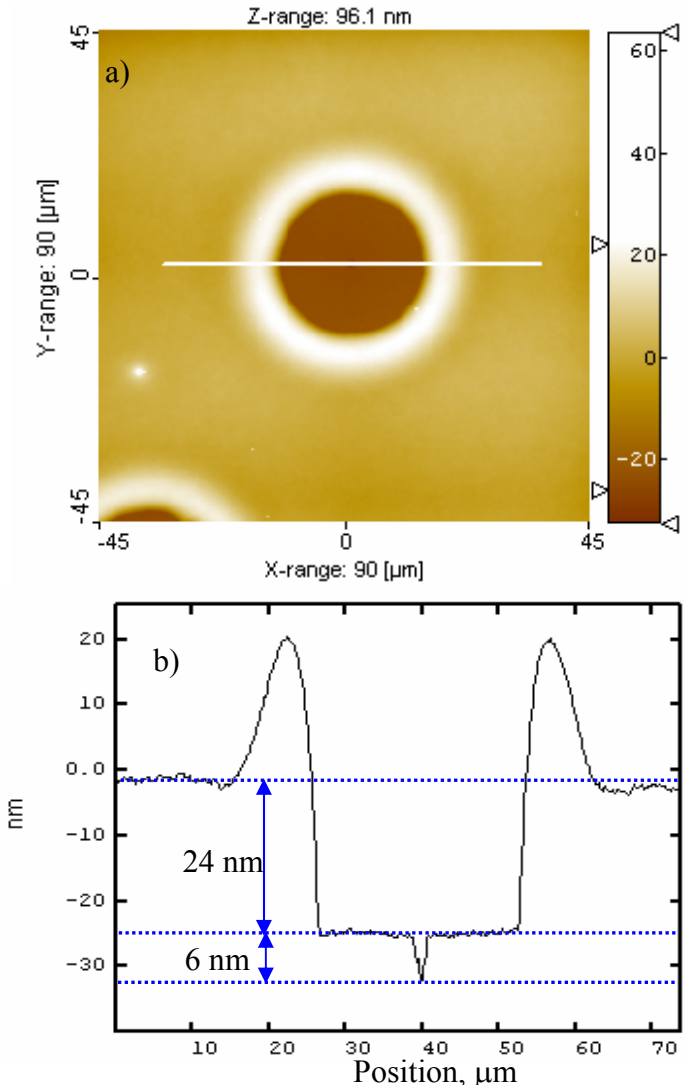

Figure 8.5 a) AFM topography image showing a 18 µm diameter hole in a 30 nm PS film containing 5 wt% of crosslinked annealed at 190°C for 160 min; **b)** the line scan analysis of the hole in Figure 8.5a showing a hole depth of 24 nm and a 6 nm layer of polymers still covering the Si substrate.

This observation is consisted with Henn et al's finding[47] who studied the dewetting of thin films of end-functionalized polystyrene on silicon. They showed that after dewetting the silicon surface was still covered by a monolayer of chains due to adsorption via their ionic end groups. In our case, the adsorption of nanoparticles is probably due to the interaction between the OH group at the Si surface and the polar group BDMS in nanoparticles. In addition, the positive unfavorable contributions to Flory interaction

parameter for linear and star molecules due to the chain architecture difference[112] between the molecules and crosslinking effect in crosslinked stars filled blends[119,151] should also be a factor controlling the interfacial segregation of nanoparticles.

AFM images of films with lower concentration (1, 2 wt%) of 32-BDMS showed a much larger hole with a ~30 nm hole depth under the same annealing conditions (Figure 8.6-8.7). This indicates the hole goes through to the Si substrate.

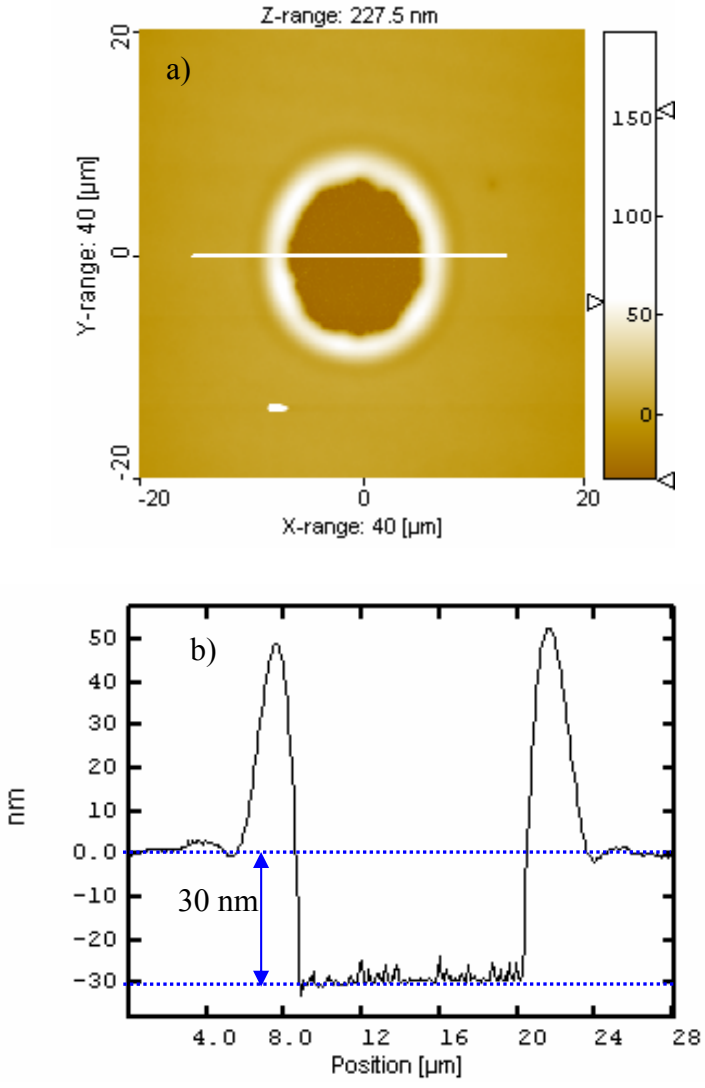

Figure 8.6. a) AFM topography image showing a 18 µm diameter hole in a 30 nm PS film containing 2 wt% of crosslinked 32-BDMS annealed at 190 °C; **b)** the line scan analysis of the hole in Figure 8.6a showing a hole depth of 30 nm.

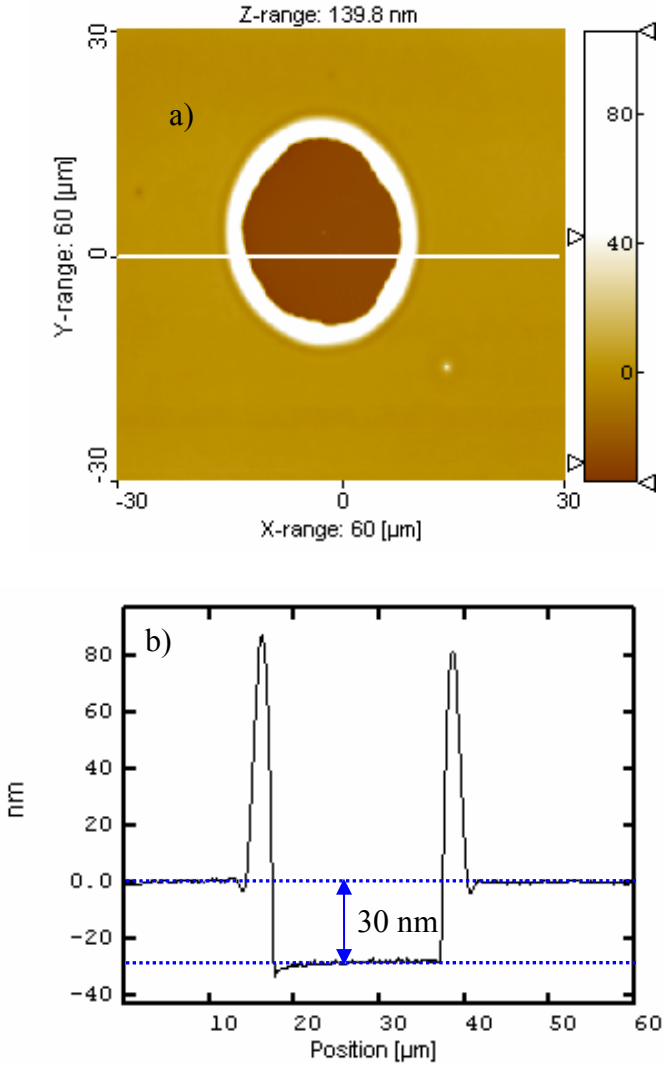

Figure 8.7 a) AFM topography image showing a 20 µm diameter hole in a 30 nm PS film containing 1 wt% of crosslinked 32-BDMS annealed at 190 °C for a short time; **b)** the section analysis of the hole in Figure 8.7a showing a hole depth of 30 nm.

Hole morphology in films with 32-OH or 35-OH showed similar AFM results (see Appendix C). The hole depth as function of concentration for all nanoparticles for are summarized in Table 8.1. A trend was observed in Table 8.1: the less the nanoparticles, the deeper the hole. For nanoparticles which showed suppression dewetting behavior, at 1 wt% all nanoparticles showed a hole depth of 30 nm (same as film thickness), while at

2wt % only 32-OH showed a hole depth less than 30nm. At 5wt%, 32-OH and 32-BDMS showed a depth of 20 and 24 nm respectively. Although 35-OH showed a maximum depth (the lowest point inside the hole to the top flat surface) of 30 nm, there appears to be some polymer remaining inside the hole (Figure C2.1). This indicates a critical concentration was essential for forming a polymer layer, which remains behind inside the growing hole.

Table 8.1. Hole depth in the dewetting films as function of nanoparticle types and concentrations (nm)

	Concentration, wt%			
	0 (Pure PS)	1	2	5
35-BDMS	30	30	30	30
32-BDMS	30	30	30	24
35-OH	30	30	30	30
32-OH	30	30	27	20

8.3.3 Discussion and conclusions

8.3.3.1 Autophobicity dewetting

The remaining polymer layer after dewetting indicates the dewetting of thin film containing 5% nanoparticles (35-OH, 32-BDMS and 32-OH) occurred not on the surface of silicon but on the surface of a polymer layer. Since nanoparticles are mainly PS based with some BCB groups and a DVB core, this is an indication of a type of autophobic behavior whereby a liquid does not spread on itself.[18,19] Since the nanoparticles within this segregation layer are compressed (as shown by NR), the resulting interfacial tension at the interface between chemically identical macromolecules from the free energy difference between the compressed and the free chains due to entropic reasons should account for the observed autophobic phenomena.[19]

8.3.3.2 Contact angle at the hole edge by AFM

The contact angles at the hole edge for pure PS, films containing 5% 35-BDMS and 32-BDMS were measured by AFM based on Figures 8.3b-8.5b. The other samples were not measured due to the surface inside holes being too rough. The contact angles are about 32°, 33° and 7° for PS, 5% 35-BDMS and 5% 32-BDMS samples, respectively. The similar contact angles of PS and PS with 5% 35-BDMS are consistent with the observation that the dewetting kinetics is essentially the same. The decreased contact angle of 32-BDMS (~7°) again confirms the observed segregation layer by NR and the polymer film is undergoing a type of autophobic dewetting.

8.3.3.3 Concentration vs. remaining layer

The results of hole depth as function of concentration and type of nanoparticles in Table 8.1 indicates a critical concentration was essential for forming a mono-polymer layer, which remains behind inside the growing hole.

Weight fraction of non-squeezed nanoparticles for hexagonal packing

Area coverage for a hexagonal packing of nanoparticles with radius of gyration R_g on a surface is calculated as:

$$\frac{3\times\pi\times R_g{}^2}{6\times\frac{1}{2}\frac{\sqrt{3}}{2}(2R_g)\times(2R_g)}=0.906$$

If the nanoparticles are spherical and hexagonally packed at the silicon surface, it should satisfy:

$$\frac{\rho\times L\times area\times x\%}{\frac{4}{3}\pi R_g{}^3\times\rho}\times\pi R_g{}^2=area\times 0.906 \qquad \text{eq. 8.1}$$

Where ρ is the density of the film (1.05 g/cm^3), L is the thickness of the film (30nm), x is weight fraction of nanoparticles in the film. The calculated weight fraction for a whole coverage is $x = (4.03 \times R_g)/100$. For example, x equals 0.242 for nanoparticles with a radius of 6 nm.

Weight fraction of squeezed nanoparticles for hexagonal packing

It is known that the nanoparticles are squeezed upon spin casting and are close to be collapsed. Assuming a constant volume during squeezing process and the shape of squeezed nanoparticle is part of a sphere with radius of R_g' and height of H (Figure 8.8), the required weight fraction of squeezed nanoparticles for hexagonal packing at the silicon surface is:

$$x = 4.03R_g \times (R_g / R)^2 \times \frac{1}{\text{segregation percentage}} \qquad \text{eq. 8.2}$$

where R is the radius of squeezed nanoparticles at the touching area on silicon wafer in Figure 8.8, which equals $R = (R_g'^2 - (R_g' - H)^2)$. R_g' can be calculated though the following equation:

$$\frac{4}{3}\pi \times R_g^{\,3} = \frac{2}{3} \times R_g'^3 \times 2 \times \arccos((R_g' - H)/R_g') - \frac{\pi}{3} \times (4R_g' \times H - H^2) \times (R_g' - H).$$

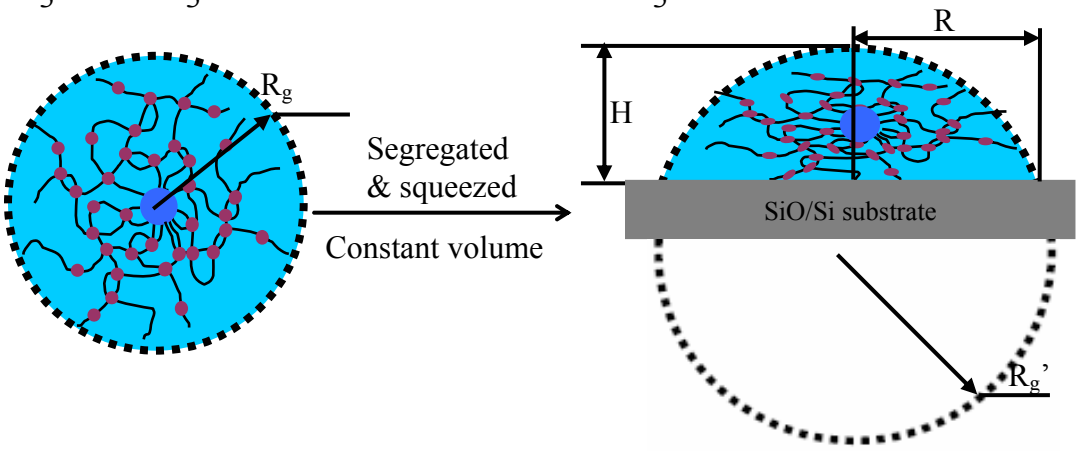

Figure 8.8. Schematic drawing for geometry of squeezed nanoparticles on silicon wafer

Taking the height of the squeezed nanoparticles as the segregation layer thickness based on NR study, and the R_g before squeezed as the values from SANS results, the required weight fraction of squeezed nanoparticles for hexagonal packing (0.906) are calculated based on equation 8.2 (Table 8.2).

Table 8.2. Weight fraction of squeezed nanoparticles for hexagonal packing (0.906)

Nanoparticles	R_g, Å	L, Å	Segregation percentage%	wt% for hexagonal packing
35-BDMS	62.6	114	49.4	23.2
32-BDMS	63.5	62.0	83.0	9.9
35-OH	62.8	62.0	91.4	9.7
32-OH	62.8	52.3	100	8.6

Table 8.2 shows that for hexagonal packing, a concentration of 8-10wt% of nanoparticles is required. However it is worth to note that the model for calculating the weight fraction for a complete coverage is not conclusive, because for example, the shape of the compressed nanoparticles is not exactly a hemisphere.

8.3.3.4 Area coverage vs. dewetting

From Chapter 6, it is also known the stronger the segregation, the higher the concentration, the more effective the suppression of dewetting. All this should be related to the area coverage of nanoparticles at silicon surface.

The area coverage for squeezed nanoparticles normalized to the close packing (0.906) can be calculated by eq.8.3:

$$area\% = \frac{x\%}{4.03 \times R_g} \times (\frac{R}{R_g})^2 \times \text{segregation percentage} \qquad \text{eq. 8.3.}$$

Assuming at low concentrations (1, 2%) the segregation layer has the same parameters as those of films containing 5 wt% of nanoparticles, such as layer thickness, segregation percentage, the calculated area coverage is shown in Table 8.3.

Table 8.3. Calculated area coverage at different concentrations of nanoparticles

Nanoparticles	Area coverage of nanoparticle%			Area dewetting % at 10min 175 °C			
	1%	2%	5%	0%	1%	2%	5%
35-BDMS	2.2	4.4	11.0	61	65	100	80
32-BDMS	8.9	17.8	44.6	61	22	10	5
35-OH	9.9	19.8	49.6	61	19	2	1
32-OH	12.3	24.6	61.5	61	2	1	1

32-OH has the highest area coverage of 61.5% at 5wt% among the four nanoparticles due to the fact that it has the strongest segregation. From Chapter 6, it is also known 32-OH is the most effective for suppression of dewetting. This indicates the higher the area coverage of nanoparticles, the more effective the suppression of dewetting. Obviously, with lower concentrations, the suppression will be less effective due to lower area coverage. For example, with a decrease of area coverage from 44.6% to 8.9% at 1wt% versus 5%, the dewetting area percentage at 10min (175 °C) increased from 5% to 22%. This is again consistent with the conclusion that the higher the area coverage of nanoparticles, the more effective the suppression of dewetting.

Based on the discussion in this chapter and the discussion in Chapter 6 and 7, we conclude: The addition of a small amount of nanoparticles to linear PS thin films can suppress or enhance the dewetting of the films depending on the specifics of the star molecules. The suppression of dewetting in PS films by the nanoparticles is related to

strong segregation of some type of nanoparticles to the polymer/silicon interface as observed by neutron reflection and atomic force microscopy. The stronger the segregation, the more effective the suppression of dewetting. Further investigation on the effects nanoparticle concentration on the dewetting of PS thin film showed the lower the concentration, the less effective the dewetting suppression. This all suggests that the higher the area coverage of nanoparticles, the more effective the suppression of dewetting and a critical coverage of nanoparticles is essential for an effective suppression of dewetting.

However it is worth mentioning that rheology, surface roughness and structural forces could also be important factors that affect the suppression of the dewetting behavior.

CHAPTER 9 RHEOLOGY OF POLYMER BLENDS

9.1 Overview

Dewetting kinetics in high molecular weight samples are generally much slower than in low molecular weight samples due to an increase in viscosity with molecular weight. It is important to study the rheology of the PS blends with nanoparticles in order to understand the viscosity behavior and the dependence of the dewetting.

For blends of linear PS with star-shaped polystyrene nanoparticles and star-shaped polystyrene nanoparticles with intra-crosslinked arms enthalpic interactions are minimized due to the same chemical composition. Further, since the particles and polymer are essentially the same material and have similar refractive indexes, dispersion forces are minimized[157,158]. Classically, it is expected that the viscosity will increase for a suspension of colloidal particles (Einstein[159]). Contrary to this model, Mackay et al.[160] found a 50% decrease in viscosity of PS with the addition of 5% PS based nanoparticles formed by intra-molecular crosslinking of the linear analog, and they attribute the decrease in viscosity to the decrease of T_g, or an increase of the free volume of the blend.

For simple thermo-rheological polymer materials, isotherms of $G'(\omega)$ and $G''(\omega)$ can be superimposed by horizontal shifts along the frequency axis ω: $G'(\omega\, \alpha_T, T_0) = G''(\omega, T)$, where T_0 is the reference temperature and α_T is the horizontal shift factor which can be evaluated by the Williams-Landel-Ferry (WLF) equation (time-temperature supposition)[158]:

$$\log \alpha_T = \frac{-c_1(T - T_0)}{c_2 + (T - T_0)}$$

Where c_1 and c_2 are the WLF parameters. A substantially minor, however not neglectable vertical shift, b_T, of the isotherms normally occurs. The increase of the moduli with temperature can be explained by the entropic nature of the elasticity in entangled polymers.

T_g can provide complementary information for miscibility of the PS/nanoparticle blends. DSC was used to measure the T_g changes as the nanoparticles are added.

9.2 Experiment

Materials

Two nanoparticles were investigated: uncrosslinked 36-BDMS and crosslinked 32-BDMS.

Sample preparation

Star-linear polymer mixtures of different compositions (5-50 wt%) were dissolved in toluene with a solids concentration of ~2 wt%. Solvent was removed by evaporation under nitrogen at room temperature for 4 h, and then the mixture was dried under vacuum at ~70 °C for one day to remove residue solvent, after which the dried powder was molded into a disk and annealed at 150 °C under vacuum for 8 hours to remove bubbles.

Rheology measurements

A Rheometric Scientific RAD III rheometer with 7.9 mm diameter parallel plates was used to study the dynamic response of linear PS and the blends under N_2 from 140 to 175°C. The gap between the plates was about 0.3-0.5 mm and a frequency range of 500–0.1 rad/s was used to obtain viscoelastic spectra of the storage (*G*'') and loss (*G*') moduli. The isotherms were shifted to obtain master curves at a reference temperature of 175 °C.

Differential scanning calorimeter

T_g of the samples were measured using a TA Instruments Q100 DSC over the range of 50-150 °C at a heating rate of 10 °C/min.

9.3 Results and discussion

WLF parameters and α_T

The complex viscosity η*, elastic modulus G'' and viscous modulus G' were measured as a function of frequency at different temperatures of 140, 150, 160,175 °C.

All samples with nanoparticles appear to obey the time-temperature superstition (TTS) principle[158] (Figure 9.1-2). To create master curves of *G*', *G*'' and η* for all measured isotherms in Figure 9.1-2, a reference temperature of 175 °C was used with a vertical shifting factor. Because of the existence of the reactive BCB group, rheology of pure nanoparticles was not obtained due to crosslinking at high temperatures as well as the rheology of blends with higher uncrosslinked 36-BDMS content (≥25%) (Figure 9.3).

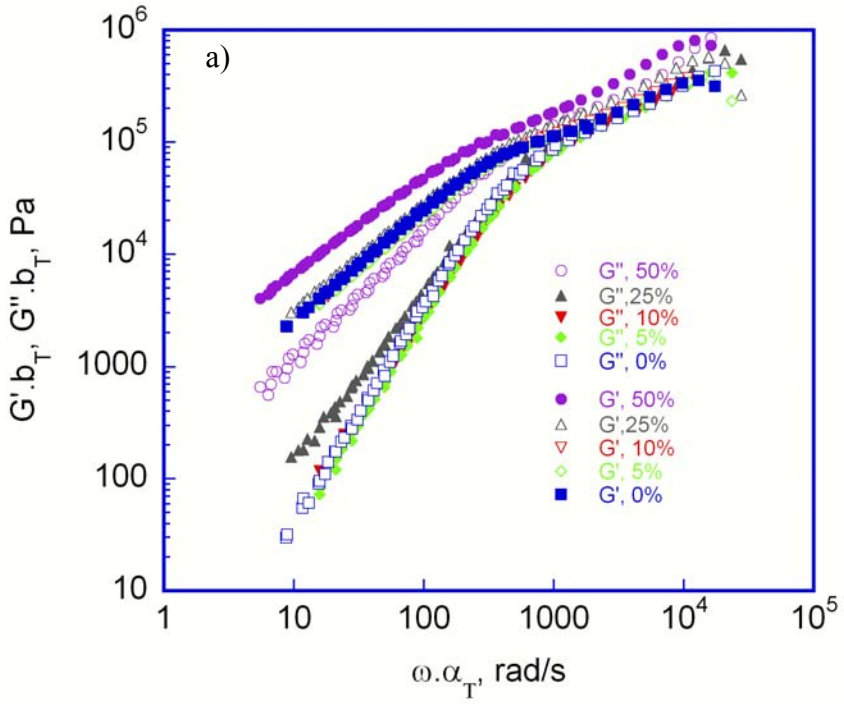

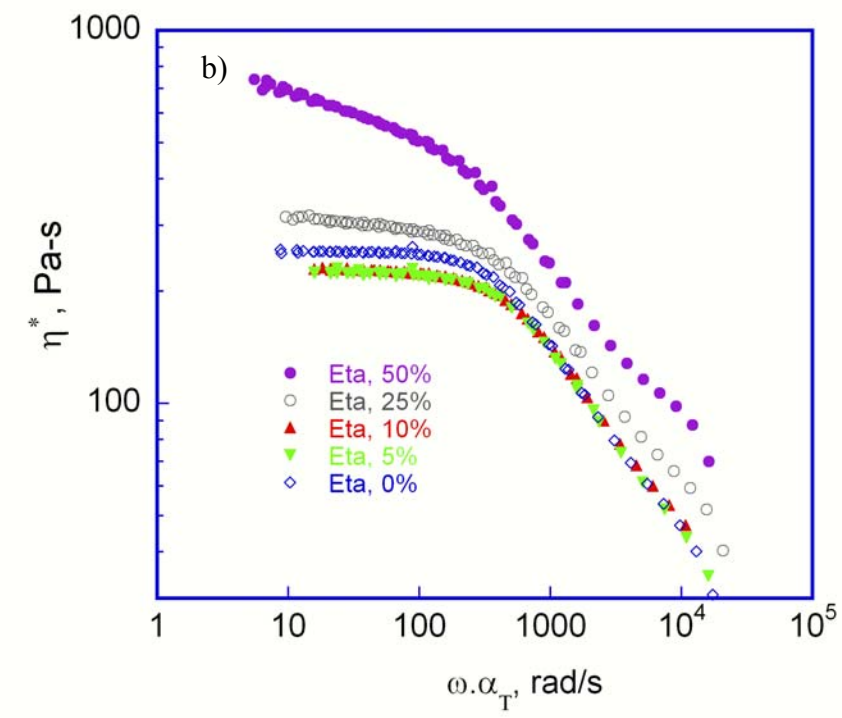

Figure 9.1. Master curves a) G', G'' and b) η* for blends with uncrosslinked 36-BDMS. The reference temperature is 175 °C.

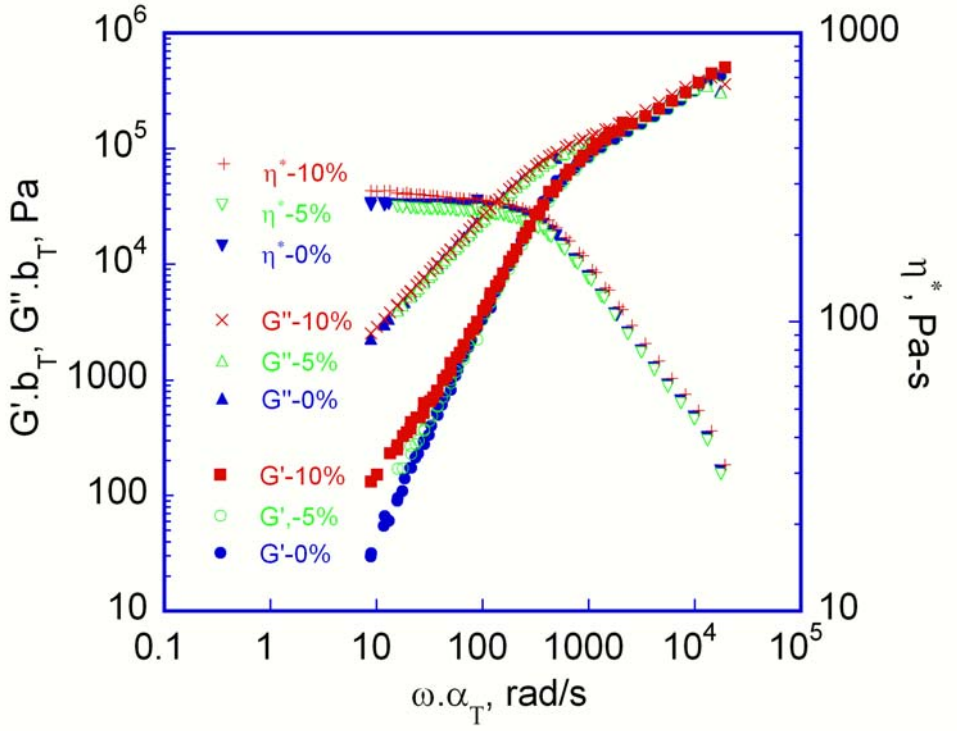

Figure 9.2. Master curves of G', G'' and η* for blends with crosslinked 32-BDMS. The reference temperature is 175 °C.

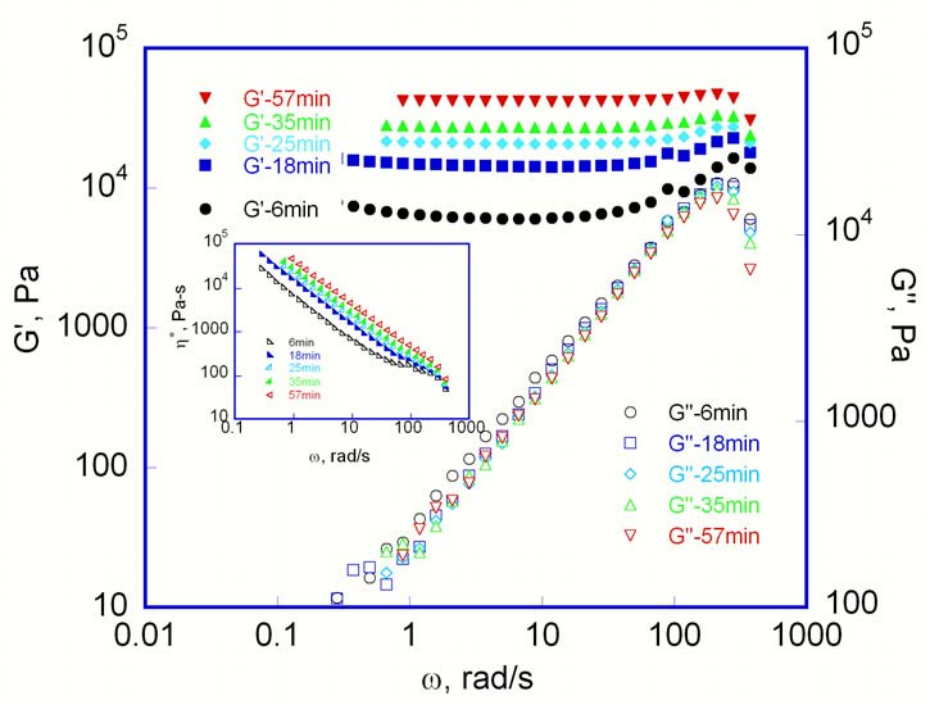

Figure 9.3. Isotherms of G', G'', η*as function of annealing time at 190°C for blends with 25% 36-BDMS

The temperature dependence of the shift factors was evaluated by Williams-Landel-Ferry (WLF) equation. The corresponding WLF parameters for samples with different nanoparticle loading percentages are summarized in Table 9.1.

Table 9.1 WLF parameters for linear polystyrene and its blend with nanoparticles using 175°C as the reference temperature

% nanoparticle	Uncrosslinked 36-BDMS		Crosslinked 32-BDMS	
	C_1	C_2	C_1	C_2
0	1.9	70.3	1.9	70.3
5	1.9	70.9	2.4	80.4
10	2.5	81.9	2.6	84.0
25	-	-	2.9	88.8
50	-	-	1.8	69.1

WLF parameters C_1 and C_2 for linear polystyrene are 1.9, 70.3 K respectively, and the WLF parameters C_1 and C_2 for polystyrene blended with nanoparticles are different from that of linear PS. A different coefficient of thermal expansion of free volume for blends from that of pure PS is assumed since the coefficient of thermal expansion of free volume (α_f) is related to C_1 and C_2 thought equation $\alpha_f = 1/(2.303C_1C_2)$[161]. Between 5-25%, the thermal expansion coefficient decreases, for blends of both uncrossed (5, 10%) and crosslinked nanoparticles (5, 10, 25%). At 50%, for blends with crosslinked nanoparticles it increases to the value of pure PS again. The change of the coefficient of thermal expansion of free volume may due to a different free volume and T_g for star polymers.

Terminal response

From Figure 9.1-2, it can be seen that pure linear PS demonstrates the standard terminal response characteristic of homopolymer melts ($G' \sim \omega^2$, $G'' \sim \omega^1$), while blends with nanoparticles exhibit non-terminal behavior characterized by a decreased terminal frequency dependence from the Rouse-like behavior of the linear polymer. An examination of the concentration (ϕ) dependence of the terminal slope indicates it scales linearly with concentration of nanoparticles (Figure 9.4). The frequency dependence of modulus of uncrosslinked 36-BDMS filled blends ($G' \sim \omega^{-6.60\phi}$; $G'' \sim \omega^{-0.40\phi}$) is stronger than that of crosslinked 32-BDMS filled blends ($G' \sim \omega^{-1.60\phi}$; $G'' \sim \omega^{-0.24\phi}$). Further, the frequency dependence of loss modulus ($G'' \sim \omega^{-0.40\phi}$; $G'' \sim \omega^{-0.24\phi}$) is weaker than that of elastic modulus ($G'' \sim \omega^{-6.60\phi}$; $G'' \sim \omega^{-1.60\phi}$). For example, PS blended with 10 wt% crosslinked 32-BDMS shows a terminal slope of $G' \sim \omega^{1.77}$, $G'' \sim \omega^{0.98}$.

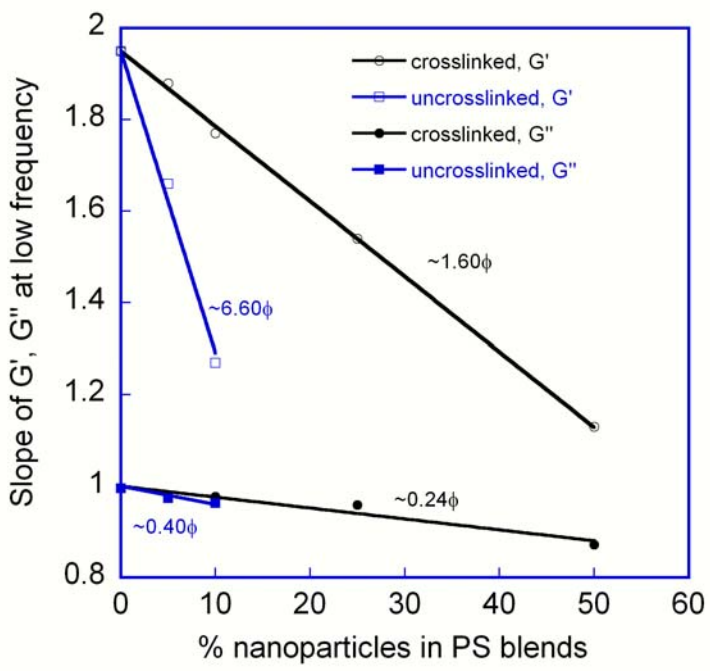

Figure 9.4. Terminal slopes as a function of concentration of nanoparticles

For highly branched polystyrene melts Kharchenko et al.[161] also observed the terminal response deviation from the Rouse model, and found that the effect of architecture on the viscous modulus is less than that the storage modulus. For reference only, dynamic response of our uncrosslinked 36-BDMS at 140°C did show the terminal response deviation from the Rouse model ($G' \sim \omega^{1.15}$; $G'' \sim \omega^{0.80}$) as shown in Figure 9.5. The frequency dependence of G' and G'' on the concentration of nanoparticles in blends indicates the terminal response of our blends may be due to the terminal response of pure nanoparticles.

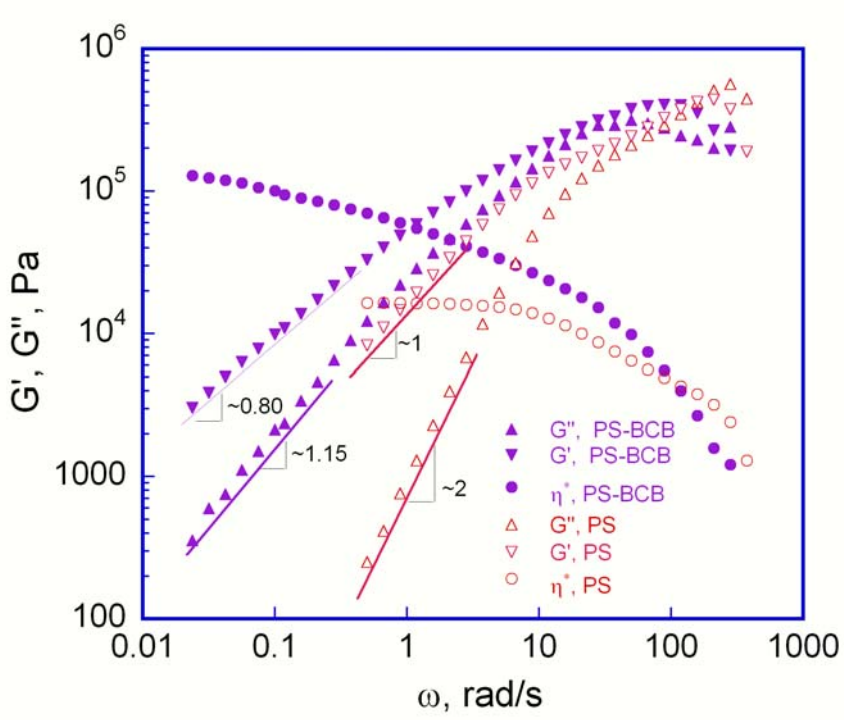

Figure 9.5. Curves of G', G'' and η* for pure uncrosslinked 36-BDMS and pure PS at 140 °C.

Terminal viscosity

Since no terminal viscosity was obtained for PS blends, the complex viscosity at 21 rad/s was compared for pure PS and PS blends as shown in Figure 9.6. If the rheology of the blends in our system follows normal mixing rule or the Einstein prediction[159], continuous increase or decrease of viscosity as a function of nanoparticle content will be observed. In our case, a continuous increase of viscosity of the blends should be observed with an increase in the nanoparticle concentration, since at 140 °C a higher viscosity was observed for pure uncrosslinked 36-BDMS than pure PS (Figure 9.5). Surprisingly, an unchanged viscosity at 5 wt% of nanoparticles followed by a 10% increased viscosity at 10 wt% of nanoparticles was observed for blends with uncrosslinked nanoparticles, while a decreased (~10%) at <10 wt% of nanoparticles followed by an obvious increased viscosity (>21%) at higher nanoparticles content (>25%) was observed for crosslinked

32-BDMS. Apparently, the rheology behavior of the nanoparticle filled PS blends does not follow the simple Einstein prediction. In this system at least two factors that have opposite effects on viscosity are required to account for the rheology behavior of these blends.

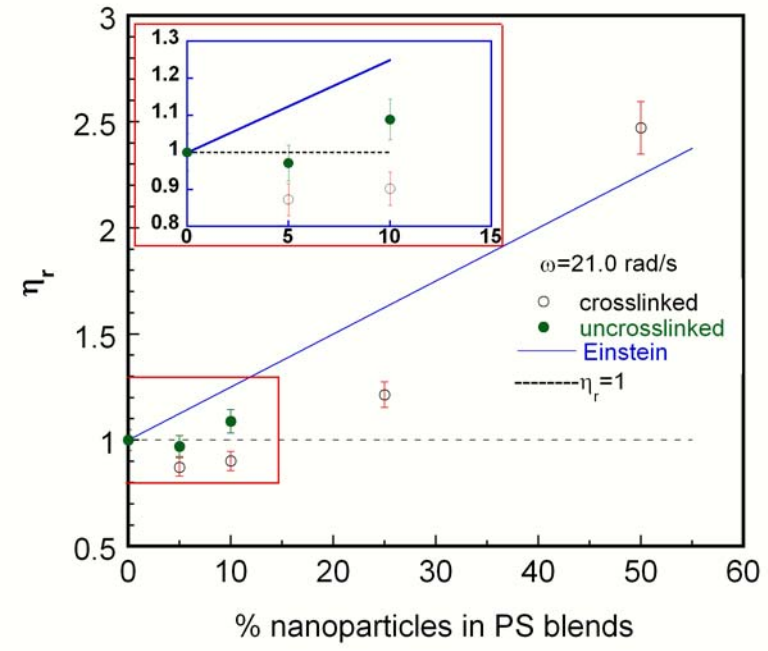

Figure 9.6. Complex viscosities of blends with uncrosslinked 36-BDMS and crosslinked 32-BDMS as a function a loading percentage of nanoparticles at 21 rad/s. The solid line is the fit for Einstein prediction ηr= (1+2.5ϕ), and the dash line is the line for ηr=1. The inset is the magnified area at low concentration.

Similar to Mackay's[160] system, dispersion forces in our system are minimized because of similar refractive indexes and same material for nanoparticles and linear polymer[157,158,]. A slightly decrease in T_g (<2 °C) (Figure 9.7) should account for the decrease of viscosity of crosslinked 32-BDMS filled blends and constant viscosity behavior of blend with 5% uncrosslinked 36-BDMS. The decrease of T_g for blends is probably due to the confinement effect of the nanoparticles as proposed by Mackay et al.[160]. They assumed that nanoparticle confinement effects produced the decrease in T_g and thus the decrease

of the viscosity which is similar to the decrease of T_g with decrease of films thickness in confined thin polymer films[162].

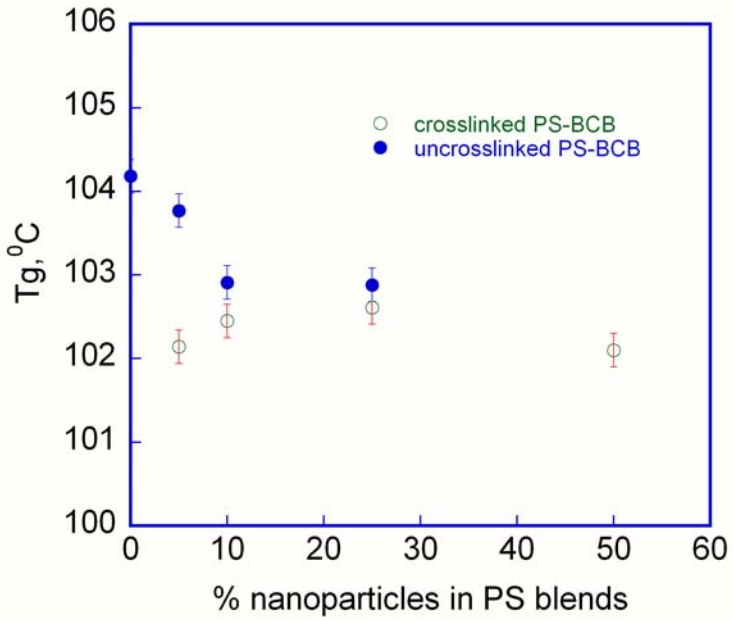

Figure 9.7. Tg of blends of PS and nanoparticles as function of concentration of nanoparticles

The obvious different rheology behavior of uncrosslinked 36-BDMS and crosslinked 32-BDMS filled PS blends indicates crosslinking plays an important role in this system. First, crosslinking lowers the dependence of viscosity on the volume fraction of nanoparticles. The terminal response of crosslinked nanoparticle filled blends show a weaker dependence on concentration of nanoparticles (Figure 9.4). This may due to the fact that crosslinked star nanoparticles are more like a hard sphere after crosslinking and the terminal response of the uncrosslinked star nanoparticles is reduced or lost. Second crosslinking probably increases the role of confinement of the nanoparticles due to the change of the structure of star polymer (more like a hard sphere). This is consistent with

the fact that at the same concentration of nanoparticles blends with uncrosslinked stars showed lower viscosity than blends with crosslinked nanoparticles.

9.4. Discussion and conclusions

The rheology of PS blended with nanoparticles showed uncrosslinked and crosslinked nanoparticles have different rheological behavior due to the crosslinking. Crosslinking decreases the dependence of rheology of blends on the volume fraction of nanoparticles and increases the role of confinement of nanoparticles. Our system is more complicated than Mackay's system in that the rheology has two contributions: the decrease of T_g in the blends due to confinement effect which gives a decrease in viscosity and the hydrodynamic and thermodynamic interactions which contributes an increase in viscosity as in a colloidal system. By controlling the crosslinking and the loading percentage of nanoparticles, the system being studied has potential for a tunable rheology behavior.

The increase of the viscosity obviously accounts for the slower kinetics at lower dewetting temperatures as shown in Chapter 6. For example, at 160 °C the zero shear viscosity (875 Pa.s) of pure PS is 5 times higher than that at 175 °C (176 Pa.s) and 10 times higher than that at 190 °C (81.5 Pa.s, calculated based on the value of C_1 and C_2) as shown in Figure 9.8. The dewetting kinetics of PS at 160 °C is 2 and 4 times slower than that at 175 and 190 °C, respectively (Chapter 6, Figure 6.2).

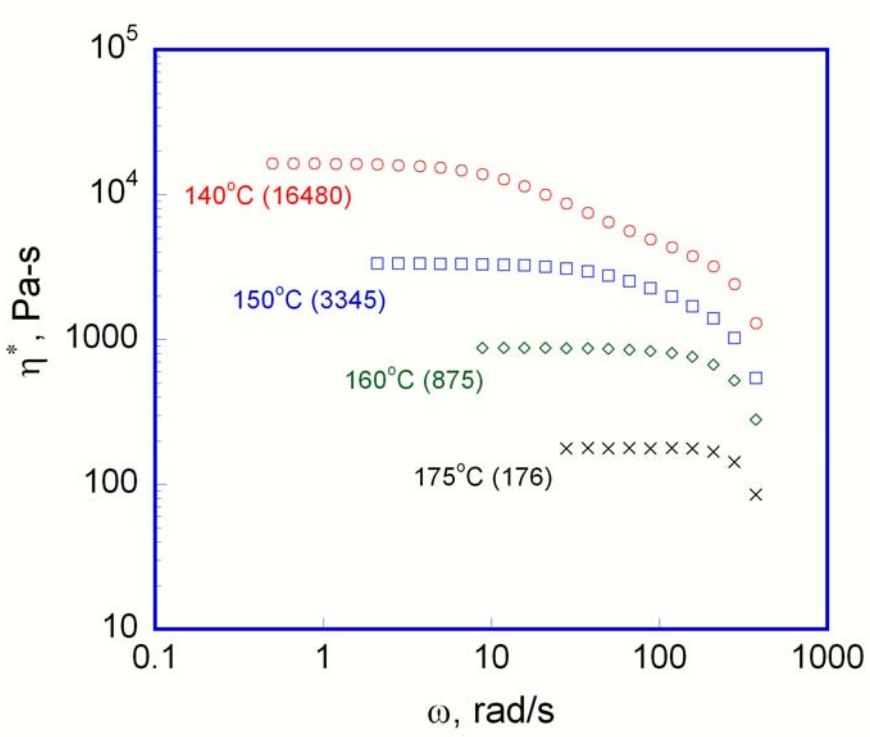

Figure 9.8. Curves of η* for pure PS as function of temperature

If there is any increase of viscosity with an addition of nanoparticles, it will contribute to the suppression of the dewetting of the film. Based on the measurements in this chapter, the rheology of the bulk blends increased only when the concentration of nanoparticle was above 10 wt%. Due to the segregation of nanoparticles to the silicon interface, there will be an increase of viscosity within the segregation layer at 5 wt%. This will make this segregation layer resistant to flow and will increase the suppressed dewetting behavior. However it is worth mentioning that there is no viscosity increase within the top layer at any concentration between 1-5wt%, as well as within the segregation layer at 1wt% concentration. This leads to the conclusion that viscosity is not the major factor that controls the suppression of dewetting in the systems studied in this work.

CHAPTER 10 SUMMARY

The influence of polystyrene star based nanoparticles on the dewetting of linear polystyrene thin films on Si/SiOx has been investigated as a function of temperature, concentration and type of the nanoparticles. The main findings of this work are:

- Small angle neutron scattering / Dynamic light scattering in solution

  Uncrosslinked and crosslinked star molecules have values of Rg in the range of 5-9 nm depending on solvent and the type of nanoparticle as shown by SANS. The Rg/Rh values for both crosslinked and uncrosslinked stars are close to the value for a hard sphere, indicating the particle-like characteristic of the polymers.

- Small angle neutron scattering for blends with linear PS

  SANS data shows the nanoparticles are miscible in the bulk with the linear PS in the temperature range of 25-175 °C. The radii of gyration of nanoparticles in bulk are in the range of 6.0-6.4 nm, which is significantly smaller than in solutions.

- Contact angle measurements

  The contact angle with DI water and methyl iodide for both pure PS film, films containing 5% nanoparticles are about 90° and 34°, respectively. The measured contact angle did not change with addition of 5% nanoparticles. This indicates there is no significant surface energy change at the polymer/air interface upon addition of nanoparticles.

- Optical microscopy

  It has been shown that the addition of a small amount of nanoparticles has a major effect on the dewetting of thin films depending on the specifics of the star molecules: 35-BDMS enhanced the dewetting of the films through increased hole nucleation

density, while the other three nanoparticles (32-BDMS, 35-OH and 32-OH) suppressed the dewetting. With an increase of nanoparticle concentration, more effective suppression behavior was observed for all the three nanoparticles exhibiting suppressed dewetting behavior. Intra-molecular crosslinking and OH end groups favored the suppression of dewetting. Among the three nanoparticles which showed suppressed dewetting behavior, the sequence is 32-OH>35-OH>32-BDMS in order of decreasing suppression effectiveness. The enhanced dewetting for 35-BDMS sample is due to an increased hole nucleation density. The radial hole growth rate for 35-BDMS is similar to that of pure PS. The suppressed dewetting behavior for the other systems is due to the formation of a segregation layer at the PS/Silicon interface. The hole growth kinetics are slowed dramatically due to the presence of this segregation layer. The dewetting behavior changes from hole growth on a silicon substrate to hole growth on a nanoparticle film. The properties of this segregation layer supported by the NR results as discussed below.

- Neutron reflection

Neutron reflectivity shows that all films containing stars have strong segregation (~21-41v%) of the star molecules which occurs during spin casting, except for the uncrosslinked 35-BDMS sample which shows only minor segregation (~7v%). With annealing, films filled with BDMS star molecules showed only minor enhanced segregation, while segregation for the other samples did not change for the samples was essentially segregated completely (100%) during the spin casting process. In terms of both the segregation percentage and the volume fraction of nanoparticles in the segregation layer, the order of segregation extent is 32-OH>35-OH>32-

BDMS>35-BDMS which is the same order for suppression of dewetting. This suggests a strong segregation of the nanoparticles to the polymer/silicon interface is essential for suppression of dewetting and the stronger the segregation, the more effective the suppression of dewetting. The segregation of nanoparticles to the Si surface is not due to immiscibility as shown by SANS, or surface energy changes as shown by contact angle measurements at the air surface. The segregation of the star polymers at the polymer/Si interface is driven by both an attraction between star molecules and the Si/SiOx surface and possibly a relatively small enthalpic penalty resulting from the unfavorable interactions between the star and linear molecules.

- Atomic force microscopy

Characterization of the hole morphology by atomic force microscopy in the films that showed suppressed dewetting behavior indicated there was a layer of nanoparticles left behind on the Si substrate inside the hole, consistent with the segregation layer observed by NR. The concentration dependence of hole depth showed that the less the nanoparticles, the deeper the hole. For nanoparticles which showed suppression dewetting behavior, at 1 wt%, all showed a hole depth of 30 nm (same as film thickness), while at 2wt % only 32-OH showed a hole depth less than 30nm. At 5wt%, 32-OH and 32-BDMS showed a depth of 20 and 24 nm respectively; although 35-OH showed a maximum depth (the lowest point inside the hole to the top flat surface) of 30 nm, there appears to be some polymer remaining inside the hole. This indicates a critical concentration was essential for forming a polymer layer, which remains behind inside the growing hole.

- Rheology

The temperature dependence of the viscosity of the linear matrix polymer and blends containing nanoparticles was measured. The temperature dependent increase of the viscosity accounts for the slower kinetics at lower dewetting temperatures. For example, at 160 °C the zero shear viscosity (875 Pa.s) of pure PS is 5 times higher than that at 175 °C (176 Pa.s). The dewetting kinetics of PS at 160 °C is 2 times slower than that at 175 °C, respectively. Only above 10wt% nanoparticles was a considerable viscosity increase observed for the blends. Due to the segregation of nanoparticles to the silicon interface, an approximately 25% increase of the viscosity within the segregation layer is expected at 5 wt% overall loading of nanoparticles (No viscosity increase is expected at 1 or 2 wt% overall loading of nanoparticles.). The increased viscosity will make the segregation layer resistant to flow. However it is worth mentioning that no viscosity increase in the top layer at 1-5wt% concentration of nanoparticles is expected due to the depletion of nanoparticles to form the segregation layer. This indicates viscosity of the layer which is undergoing dewetting is not the major factor that controls the suppression of dewetting in the systems studied in this work.

In summary, this work has important implications for controlling dewetting in coating materials and forming continuous polymer films on substrates.

CHAPTER 11 FUTURE WORK

11.1 Roughness effect on dewetting

The wettability of thin films on various substrates is related to the surface roughness.[163] Kerle et al.[164] observed that crosslinking induced roughness could enhance the wetting of a random copolymer of ethyl-ethylene and ethylene melt on its crosslinked network. Netz et al[165] also theoretically showed the possibility of a wetting transition induced by geometric roughness of a solid substrate for the case where the flat substrate does not show a wetting layer.

Calcium fluoride (CaF_2) is commonly used as an under layer for artificially roughening surfaces of metallic thin films. The roughness of CaF_2 depends on the amount of deposited CaF_2.

An interesting set of experiments would be to study the dewetting behavior of PS on top of an aluminum surface with different roughness created by a under layer of CaF_2 on Si. Similar to dewetting experiment in Chapter 6, dewetting of PS thin film on aluminum surface with different roughness can be studied *in situ* using an optical microscope in a hot stage under N_2 for different time intervals.

11.2 Structural forces

Another factor that may contribute to the observed suppression of dewetting in polymer thin films by adding nanoparticles is the structural forces. It has been found the ordering of nano-sized polystyrene spheres in water at the interfaces increased the wetting ability of a micellar fluid[166,167] due to the extra disjoining pressure.

According to the DLVO (Derjaguin-Laudau-Verwey-Overbeek) theory, the interaction between the confining surfaces is the sum of effective electrostatic (when surfaces are

charged) and dispersion interactions. When two surfaces or particles approach closer than a few nanometers, continuum theories of attractive van der Waals and repulsive double-layer force often fail to describe their complete interaction. First measurements of such short-range oscillatory forces between two solid surfaces arising from structure in the intervening liquid were done by Israelachvili and his co-workers[168] in 1980.

The oscillatory structural/depletion forces can be described by the evaluation of an extra hard-core-like excluded volume contribution due to the finite size of the confined fluid particles. Simple empirical expressions for the structural/depletion forces contribution to the film disjoining pressure have been made by fitting the theoretical or experimental data[169,170,171]. The simplest analytically solvable theory for a hard-sphere problem is the Percus-Yevick (PY) theory. It has been applied and examined by means of computer simulations for both bulk hard-sphere-like fluid as well as hard-sphere-like fluid under single wall and film confinements. The PY theory has been shown to be reliable in this respect for the majority of applications using hard-sphere modeling.

11.3 Tg of thin films

Although we have studied the changes of T_g in bulk blends due to the addition of nanoparticles, it is worthwhile to mention that the glass transition temperature of thin films is different from its bulk T_g. Computer simulations, theory and experiments reveal chain segments at the free surfaces have a higher mobility than the remainder of the sample due to a larger configurational freedom[172,173,174,175,176], which will cause an decrease of T_g with decreasing film thickness. In the vicinity of the substrate, on the other hand, the chain segment/substrate interaction are such that the mobility of the chains is appreciably lower in the vicinity of the substrate[177,178], which will cause an increase of T_g

with decreasing film thickness. It is argued that the variation of T_g in supported thin films is a manifestation of the fact which dynamics, the one of the surface or interface layer exert a dominant influence on the average glass transition temperature of the film.[179] In cases where the polymer segment–substrate interaction is particularly strong, the relatively immobile layer of polymer in the vicinity of the substrate may exert the dominant influence on the average glass transition temperature of the film[180,179,181,182]. For example, the effective T_g of poly (methyl methacrylate) and poly (vinyl pyridine) thin films on SiO_x/Si substrates are shown to increase with decreasing film thickness.[180,181] This is consistent with the fact that the more polar interactions of the PMMA and PVP chain segments with the oxide layer hydrogen bonds have a sufficiently strong influence on the dynamics of the segments in the vicinity of the substrate. Computer simulations of polymer chains on highly interacting substrates corroborate these findings, T_g increases with increasing film thickness.[182] Brillouin scattering experiments on freely standing PS films reveled that the decrease of Tg with film thickness is more significant than the decrease measured for supported PS films[183,184].

The T_g values of the films can be characterized by several techniques: thermal analysis, ellipsometry, and reflectivity. In the future work ellipsometry or x-ray reflectometry could be used to measure the glass transition of the thin films used for dewetting studies in this thesis.

APPENDIX

Appendix A Additional dewetting data

Due to the similarity of the dewetting data of 35-OH and 32-OH to that of 32-BDMS, and due to the similarity of dewetting data of 32-BDMS at lower concentration (1,2wt%) and lower temperatures (175, 160 °C) to that at 5 wt% and 190 °C, the optical micrographs showing the dewetting and the dewetting kinetics for 35-OH, 32-OH and for 32-BDMS at 1, 2 wt% at 175 and 160 °C are listed in Appendix A (see Table A.1).

Table A.1 Dewetting data listed in Appendix A

Appendix		Concentration, wt%		
Appendix A1: Dewetting of PS thin films containing 35-OH	160 °C	1	2	5
	175 °C	1	2	5
	190 °C	1	2	5
Appendix A1: Dewetting of PS thin films containing 32-OH	160 °C	1	2	5
	175 °C	1	2	5
	190 °C	1	2	5
Appendix A3: Dewetting of PS thin films containing 32-BDMS at lower temperatures and low concentrations	160 °C	1	2	-
	175 °C	1	2	-

Appendix A1 Dewetting of PS thin films containing 35-OH

Optical microscopy also showed clear suppression of dewetting upon addition of uncrosslinked 35-OH. Figures A1.1a-f, A1.3.a-f, A1.4.a-f are optical images of 30 nm thick PS films containing uncrosslinked 35-OH on silicon annealed at two different time scales, three different temperatures (160, 175 and 190 °C) and three different nanoparticle concentrations (1, 2, 5 wt%).

Figures A1.1a & A1.1b are optical images of films containing 5% 35-OH annealed for 3 min and 25 min at 190 °C, respectively. After 3 minutes at 190 °C, the film with 5% 35-

OH also shows the onset of dewetting but with much smaller holes (~2.5 μm) than in polymer (Fig. 6.1a). Further annealing of the film containing 5% 35-OH at 190 °C for 25 min only shows a slow growth of holes (to ~4 μm)(Figure A1.1b) in contrast to a fully dewet of pure PS film (Fig. 6.1b) under the same conditions. In addition, the holes did not continue to evolve and became pinned after reaching a radius of about 4 μm.

a) 190 °C-3min-(10X)

b) 190 °C-25min-(10X)

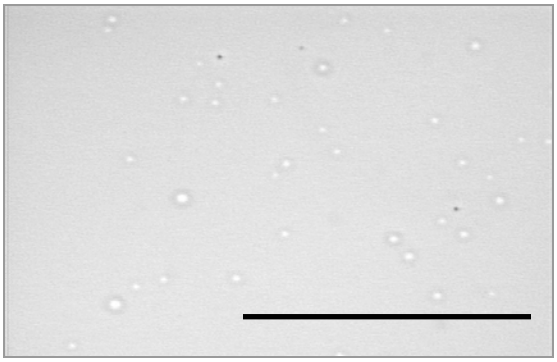

c) 175 °C-3min-(50X)

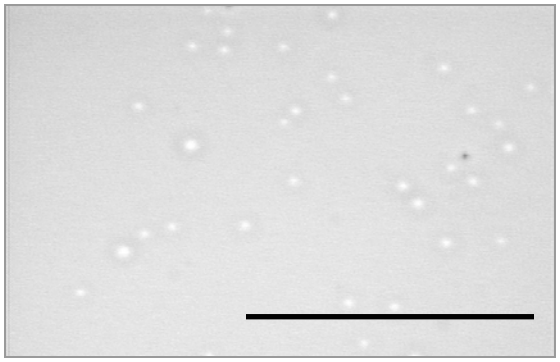

d) 175 °C-25min-(50X)

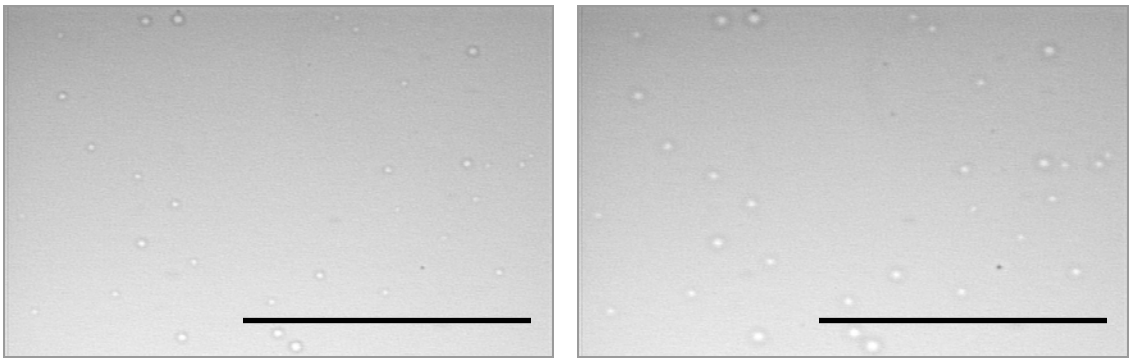

e) 160 °C-3min-(50X) f) 160 °C-25min-(50X)

Figure A1.1. Optical micrographs showing partially dewet thin PS films with 5% uncrosslinked 35-OH at a) 190 °C annealed for 3 min; b) 190 °C annealed for 25 min; c) 175°C annealed for 3 min, d) 175 °C annealed for 25 min; e) 160 °C annealed for 3 min; f) 160 °C annealed for 25min. (scale bar = 100μm)

The dewetting kinetics at different annealing temperatures is shown in Figure A1.2. At lower annealing temperatures, 175°C, 160 °C, the dewetting process was slower. The hole growth in the films containing 35-OH does not show the $t^{2/3}$ power law either. This indicates a strong slippage of polymers melt at the substrate surface is not applicable for this condition.

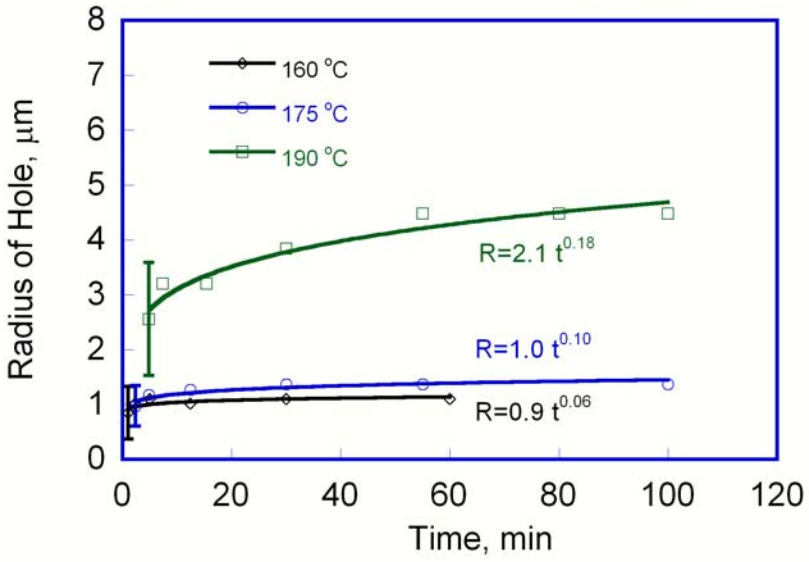

Figure A1.2. Hole growth as function of time for blends with 5 wt% 35-OH.

Micrographs for the dewetting of PS containing 2, 1wt% 35-OH at different annealing temperatures were shown in Figure A1.3 a-f, and Figure A1.4 a-f respectively.

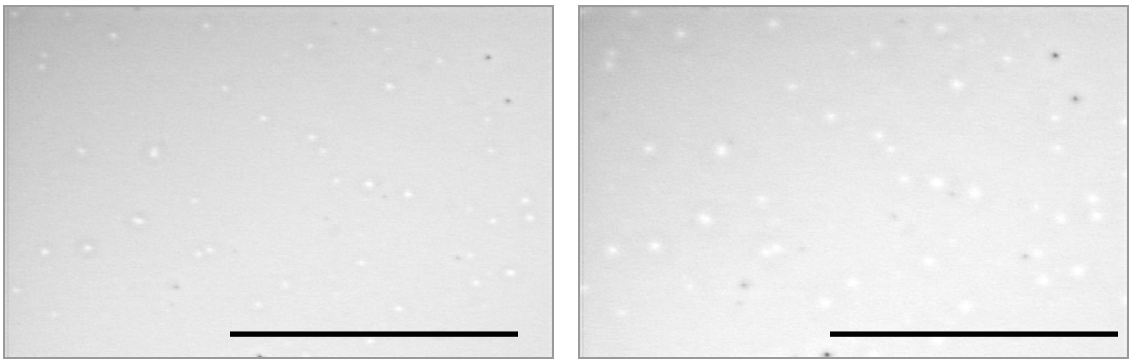

a) 190 °C-3min-(50X)

b) 190 °C-25min-(50X)

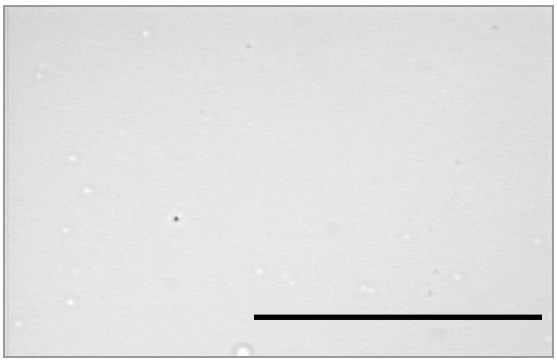

c) 175 °C-3min-(50X)

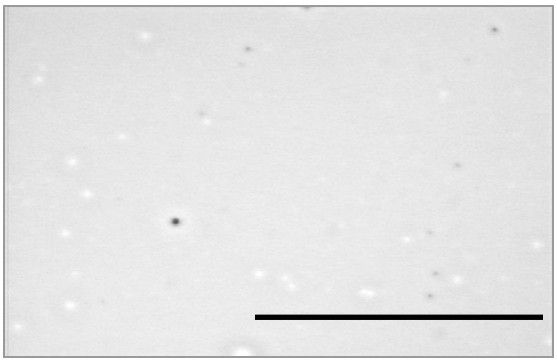

d) 175 °C-25min-(50X)

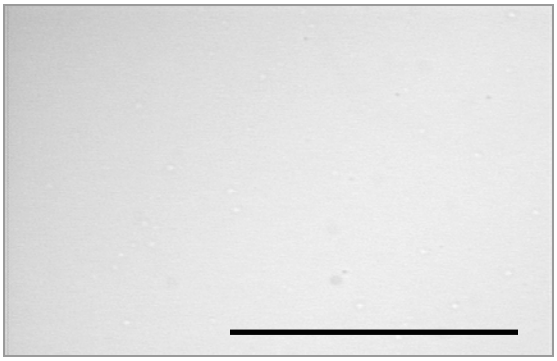

e) 160 °C-3min-(50X)

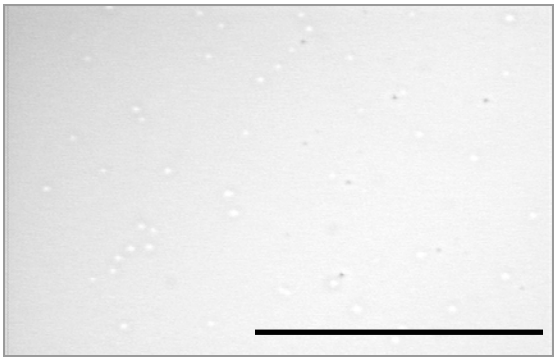

f) 160 °C-25min-(50X)

Figure A1.3. Optical micrographs showing partially dewet thin PS films with 2 wt% uncrosslinked 35-OH at a) 190 °C annealed for 3 min; b) 190 °C annealed for 25 min; c) 175 °C annealed for 3 min, d) 175 °C annealed for 25 min; e) 160 °C annealed for 3 min; f) 160 °C annealed for 25min. (scale bar = 100μm)

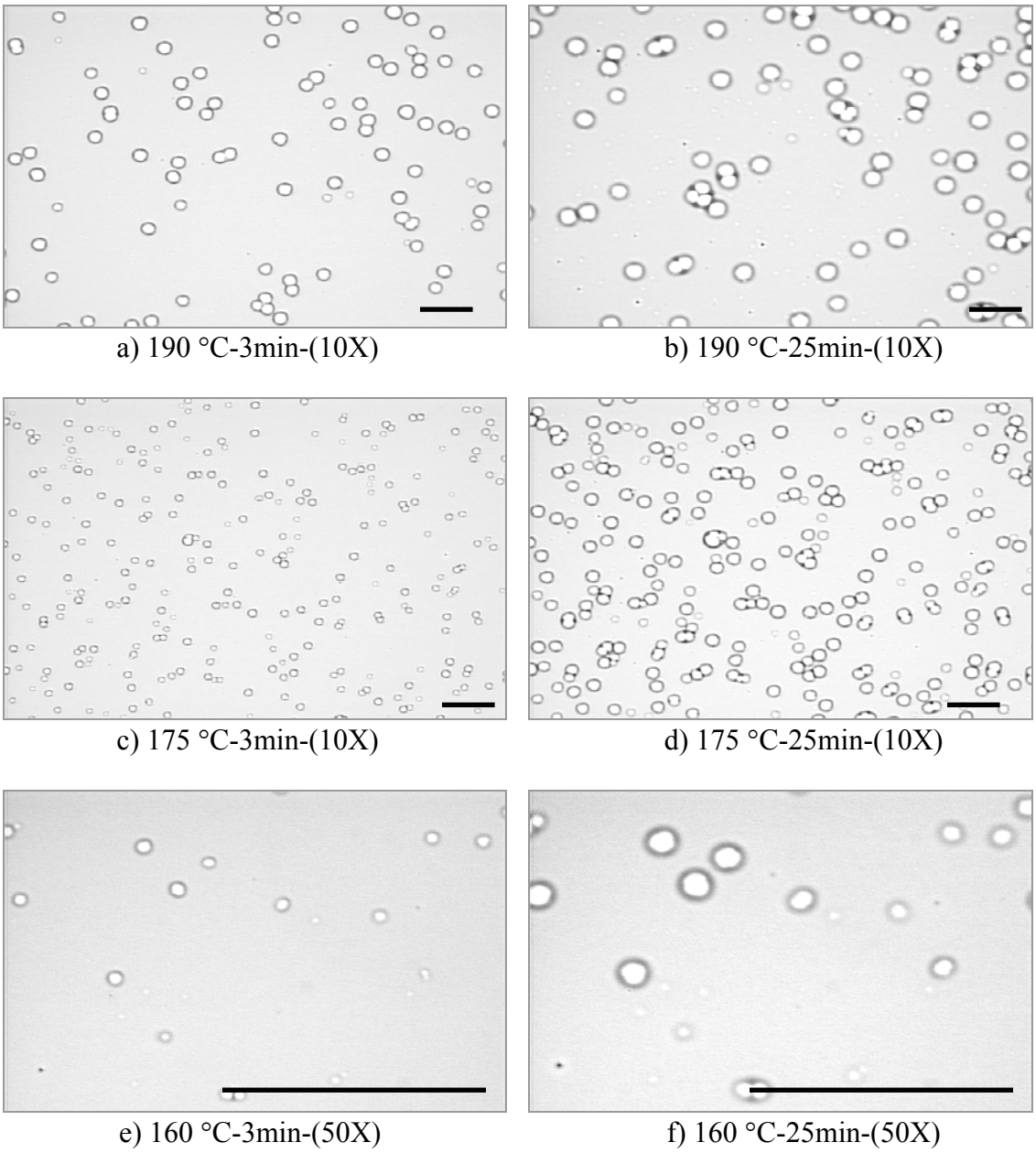

a) 190 °C-3min-(10X)

b) 190 °C-25min-(10X)

c) 175 °C-3min-(10X)

d) 175 °C-25min-(10X)

e) 160 °C-3min-(50X)

f) 160 °C-25min-(50X)

Figure A1.4. Optical micrographs showing partially dewet thin PS films with 1 wt% uncrosslinked 35-OH at a) 190 °C annealed for 3 min; b) 190 °C annealed for 25 min; c) 175 °C annealed for 3 min, d) 175 °C annealed for 25 min; e) 160 °C annealed for 3 min; f) 160 °C annealed for 25min. (scale bar = 100μm).

The growth of hole as function of annealing time was shown in Figure A1.5 and A1.6. Clearly, films with lower concentration of nanoparticles are less effective in suppression of dewetting in PS films.

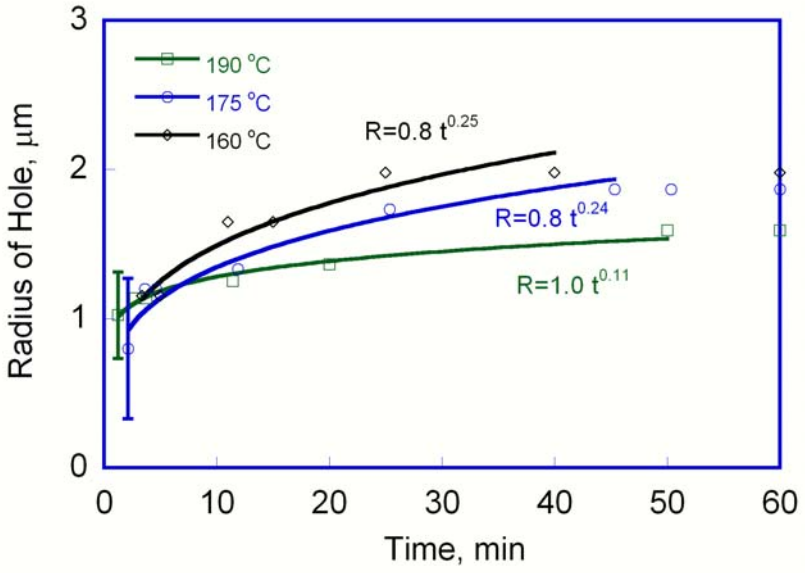

Figure A1.5. Hole growth as function of time for blends with 2 wt% 35-OH.

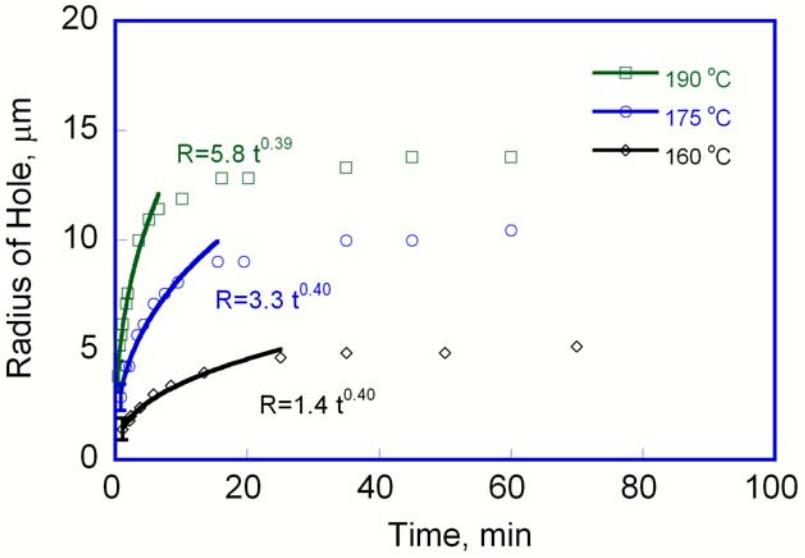

Figure A1.6. Hole growth as function of time for blends with 1 wt% 35-OH.

Appendix A2 Dewetting of PS thin films containing 32-OH

Figures A2.1a-f, A2.3 a-f, A2.4 a-f are optical images of 30 nm thick PS films containing crosslinked 32-OH on silicon annealed at two different time scales, three different temperatures (160, 175 and 190 °C) and three different nanoparticle concentrations (1, 2, 5 wt%).

Thin films of linear PS blended with 5% crosslinked 32-OH also showed clear suppression of dewetting behavior (Figure A2.1 a-f). Figures A2.1a & A2.1b are optical images of films annealed for 3 min and 25 min at 190 °C, respectively. After 3 minutes at 190 °C, the film with 5% crosslinked 32-OH also shows the onset of dewetting but with much smaller holes of ~2.5 μm in radius (Figure A2.1a) than those in the linear polymer film (Fig. 6.1a). Further annealing of this films for 25 min at 190 °C only shows a slow growth of holes (to ~3.5 μm)(Figure A2.1b). In addition, the holes did not continue to evolve and became pinned after reaching a radius of about 4 μm.

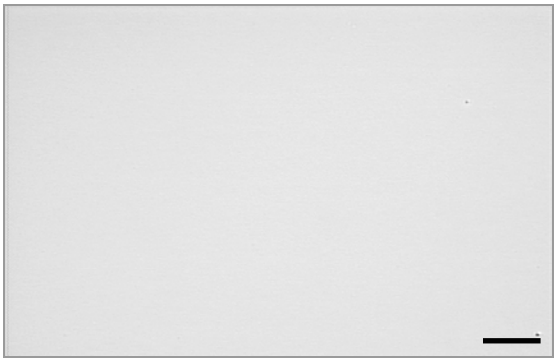

a) 190 °C-3min-(10X)

b) 190 °C-25min-(10X)

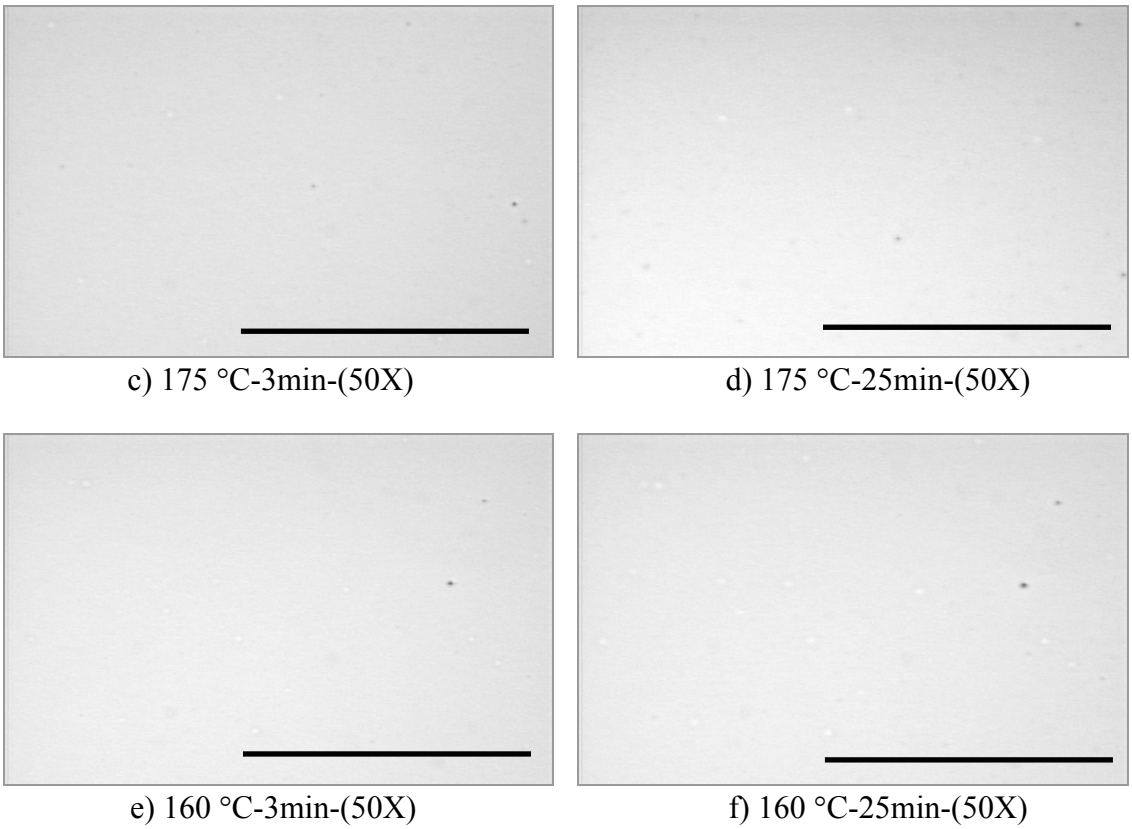

c) 175 °C-3min-(50X) d) 175 °C-25min-(50X)

e) 160 °C-3min-(50X) f) 160 °C-25min-(50X)

Figure A2.1. Optical micrographs showing partially dewet thin PS films with 5 wt% crosslinked 32-OH at a) 190 °C annealed for 3 min; b) 190 °C annealed for 25 min; c) 175 °C annealed for 3 min, d) 175 °C annealed for 25 min; e) 160 °C annealed for 3 min; f) 160 °C annealed for 25min. (scale bar = 100μm)

The dewetting kinetics at different annealing temperatures is shown in Figure A2.2. At lower annealing temperatures, 175°C, 160 °C, the dewetting process was slower.

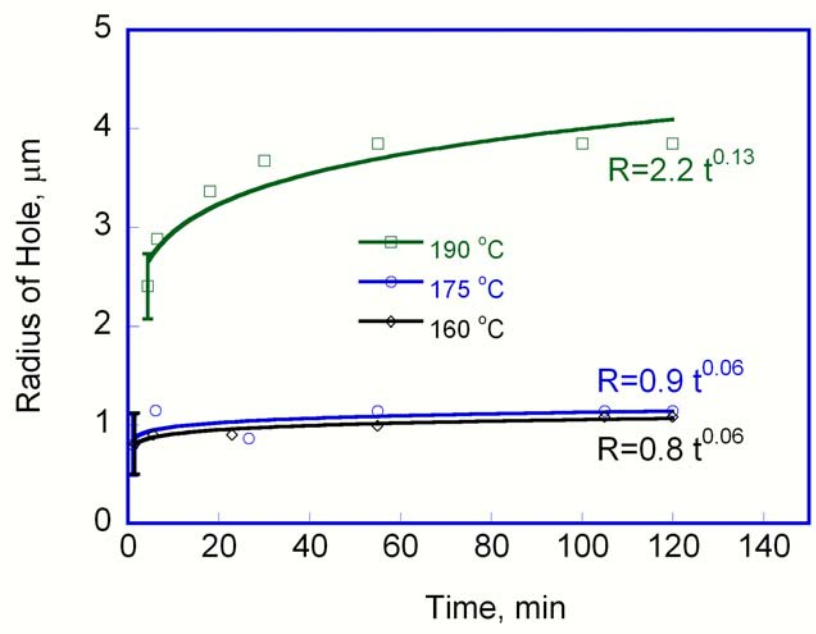

Figure A2.2. The growth of hole as function of time for blends with 5 wt% 32-OH.

The hole growth in polystyrene thin films containing 32-OH does not show the dependence on annealing time as $t^{2/3}$. This indicates a strong slippage of polymers melt at the substrate surface is not applicable for this condition.

Micrographs for the dewetting of PS filled with different concentrations of 32-OH at different annealing temperature are shown in Figure A2.3a-f, and Figure A2.4a-f.

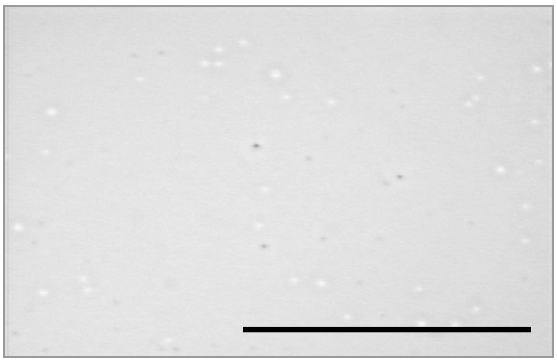

a) 190 °C-3min-(50X)

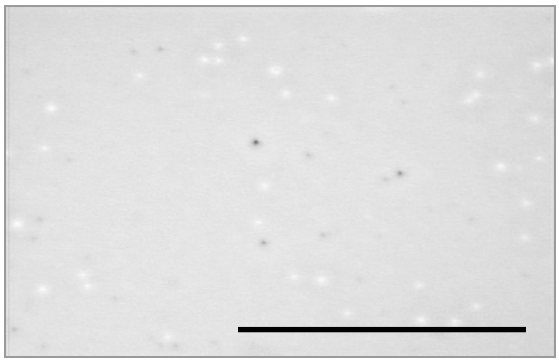

b) 190 °C-25min-(50X)

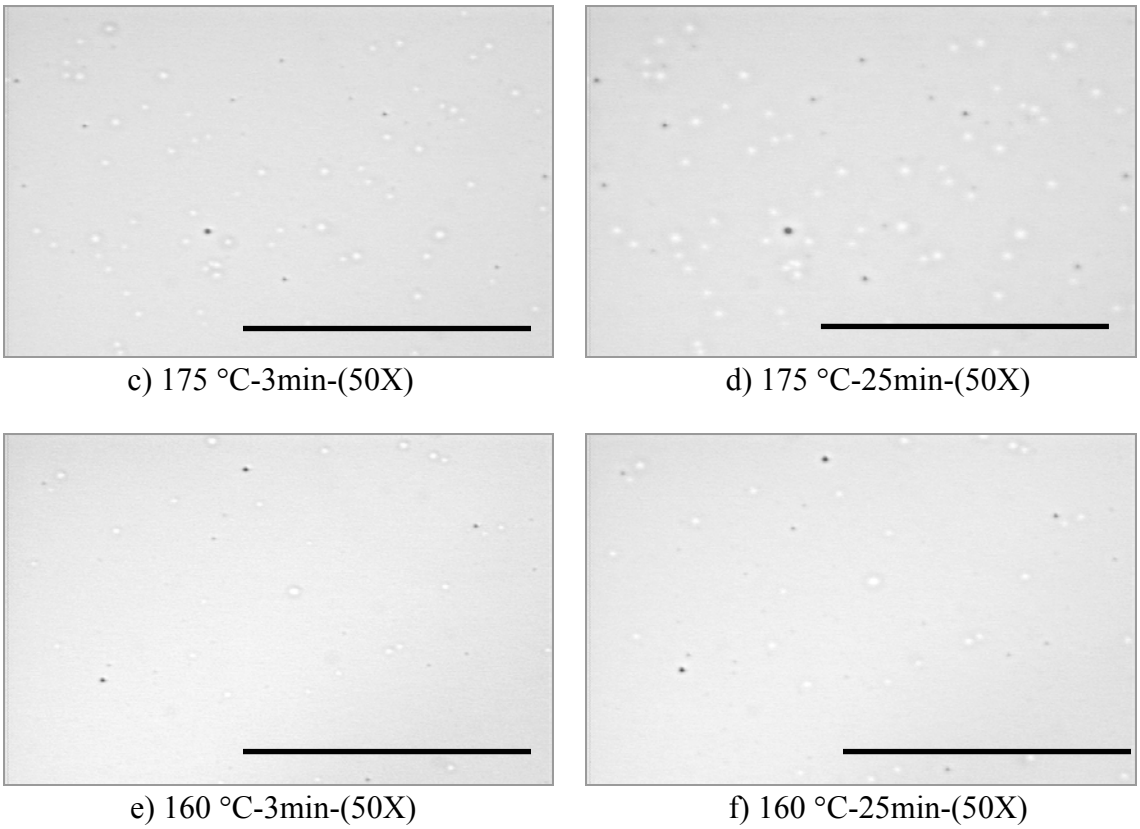

c) 175 °C-3min-(50X) d) 175 °C-25min-(50X)

e) 160 °C-3min-(50X) f) 160 °C-25min-(50X)

Figure A2.3. Optical micrograph showing partially dewet thin PS films with 2% crosslinked 32-OH at a) 190 °C annealed for 3 min; b) 190 °C annealed for 25 min; c)175 °C annealed for 3 min, d) 175 °C annealed for 25 min; e) 160 °C annealed for 3 min; f) 160 °C annealed for 25min. (scale bar = 100μm)

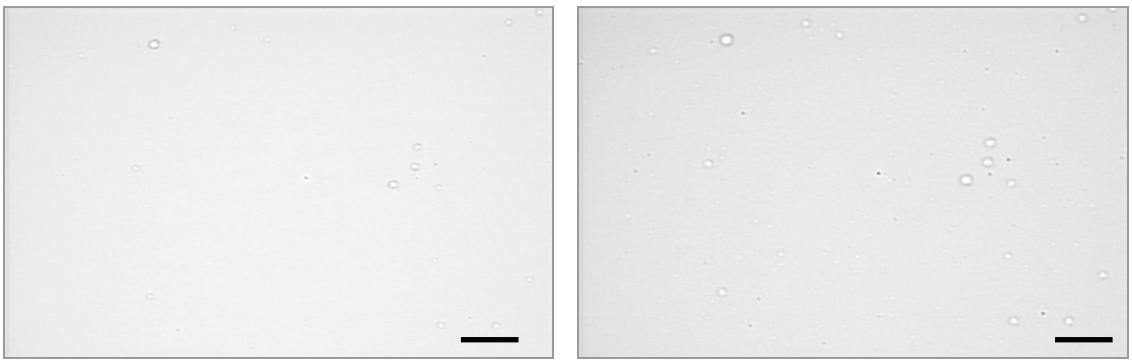

a) 190 °C-3min-(10X) b) 190 °C-25min-(10X)

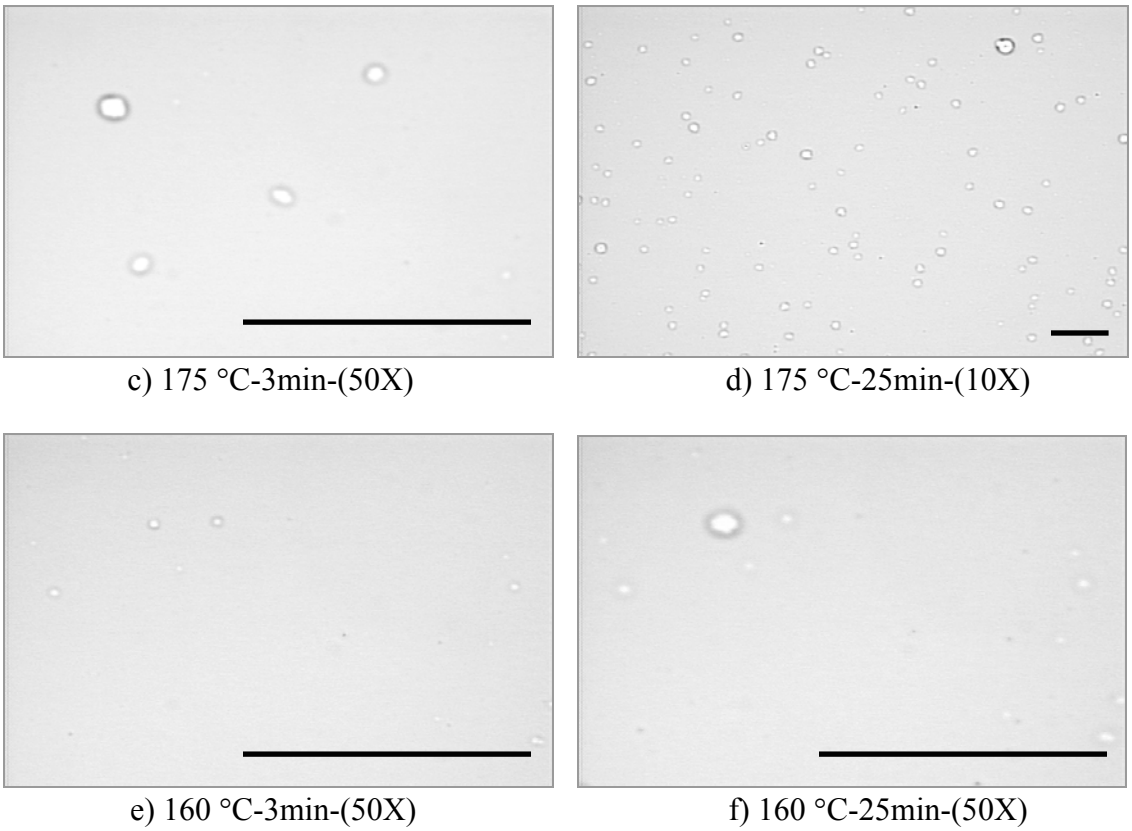

c) 175 °C-3min-(50X) d) 175 °C-25min-(10X)

e) 160 °C-3min-(50X) f) 160 °C-25min-(50X)

Figure A2.4. Optical micrographs showing partially dewet thin PS films with 1 wt% crosslinked 32-OH at a) 190 °C annealed for 3 min; b) 190 °C annealed for 25 min; c) 175 °C annealed for 3 min; d) 175 °C annealed for 25 min; e) 160 °C annealed for 3 min; f) 160 °C annealed for 25min. (scale bar = 100μm)

Clearly, films with lower concentrations of nanoparticles also showed obvious suppression dewetting behavior but it was less effective than films with 5 wt% nanoparticles. The hole growth as function of annealing time is shown in Figure A2.5 and A2.6.

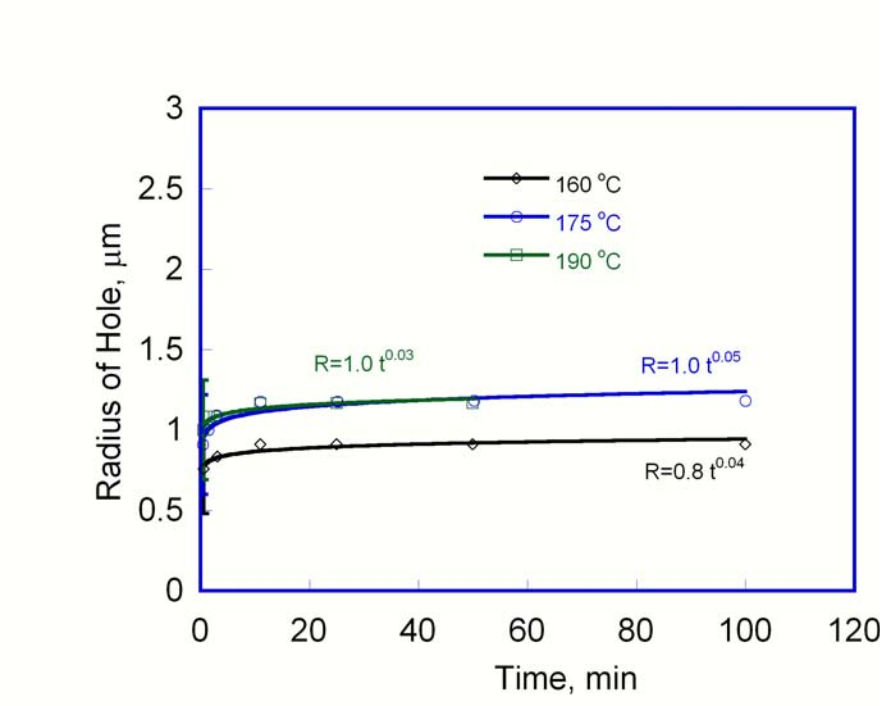

Figure A2.5. Hole growth as function of time for blends with 2 wt% 32-OH.

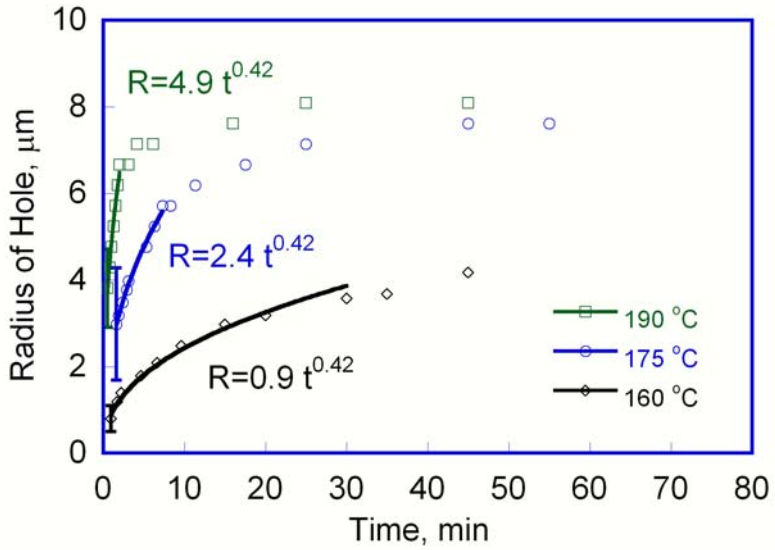

Figure A2.6. Hole growth as function of time for blends with 1 wt% 32-OH.

Appendix A3 Dewetting of PS thin films containing 32-BDMS at lower temperatures and low concentrations

Figure A3.1a-d and A3.2a-d are micrographs showing dewetting of PS films containing 2 and 1 wt % 32-BDMS respectively.

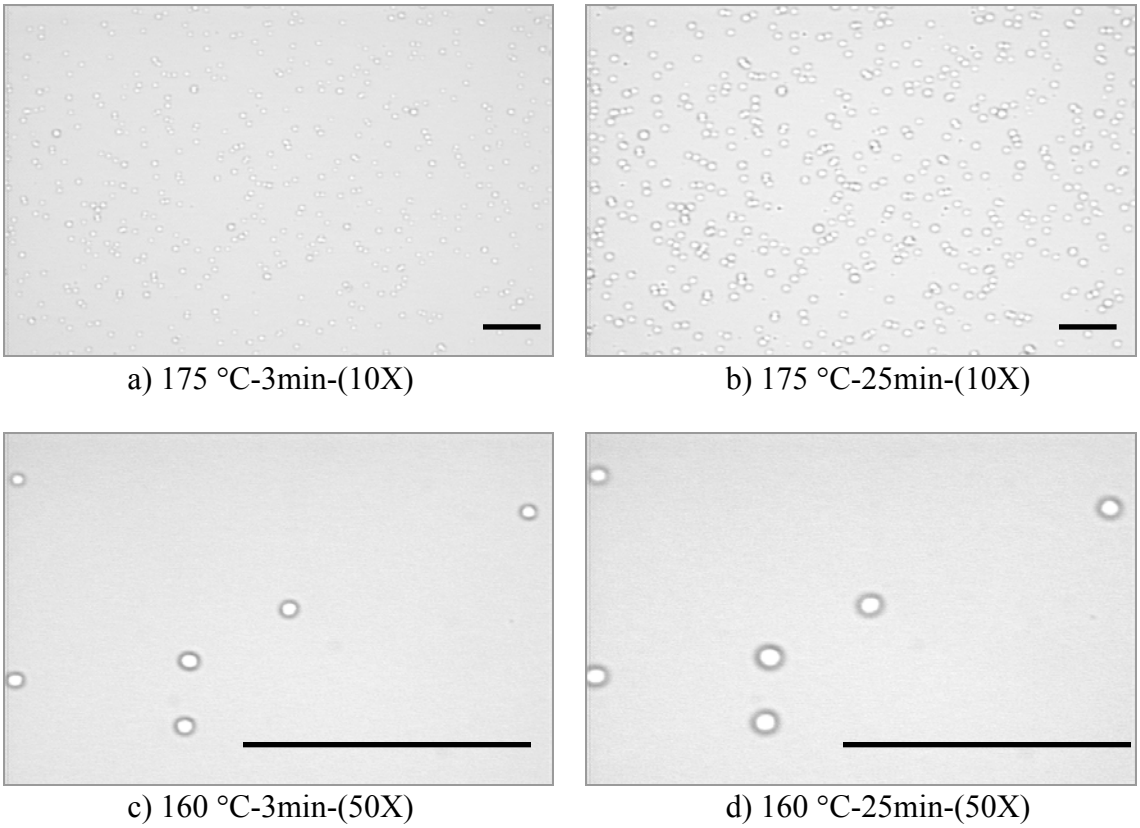

a) 175 °C-3min-(10X) b) 175 °C-25min-(10X)

c) 160 °C-3min-(50X) d) 160 °C-25min-(50X)

Figure A3.1 Optical micrographs showing partially dewet thin PS films with 2 wt% crosslinked 32-BDMS at a) 175 °C annealed for 3 min, b) 175 °C annealed for 25 min; c) 160 °C annealed for 3 min; d) 160 °C annealed for 25min. (scale bar = 100μm)

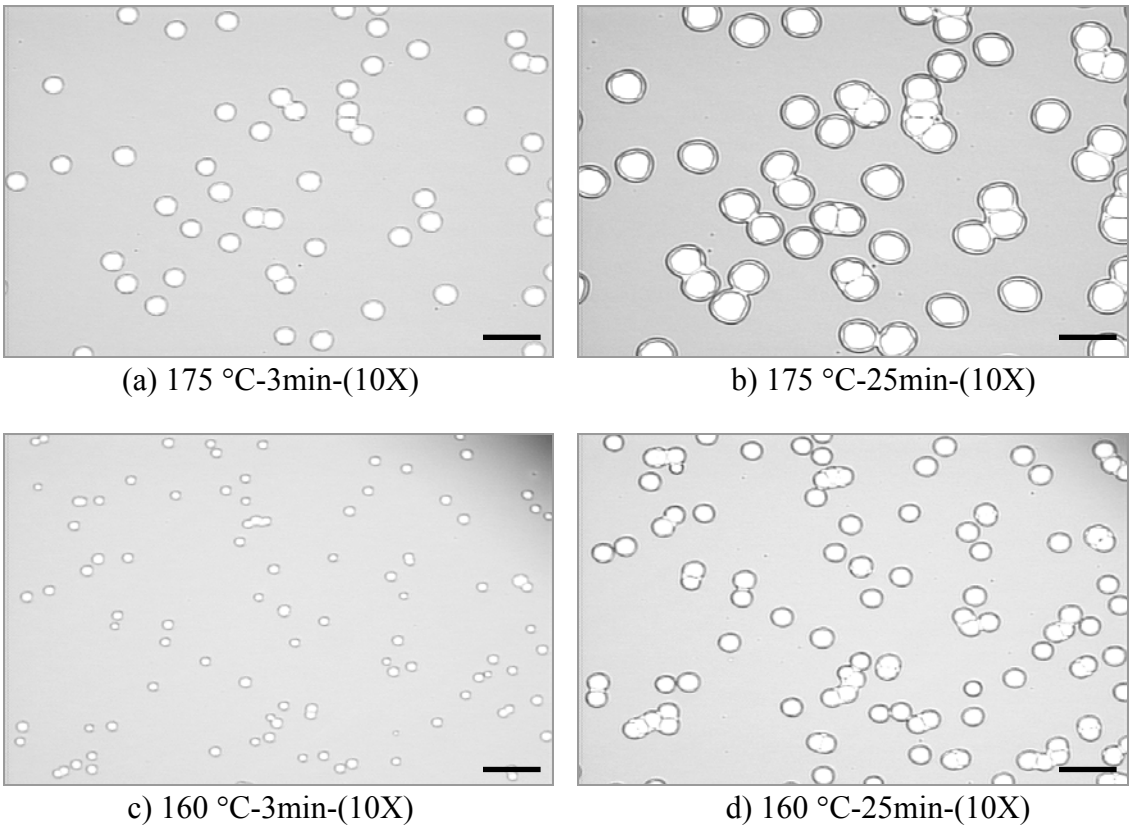

(a) 175 °C-3min-(10X) b) 175 °C-25min-(10X)

c) 160 °C-3min-(10X) d) 160 °C-25min-(10X)

Figure A3.2 Optical micrographs showing partially dewet thin PS films with 1 wt% crosslinked 32-BDMS at a) 175 °C annealed for 3 min, b) 175 °C annealed for 25 min; c) 160 °C annealed for 3 min; d) 160 °C annealed for 25min. (scale bar = 100μm)

The growth of hole as function of annealing time at different concentration of nanoparticles is shown in Figure A3.3 and A3.4.

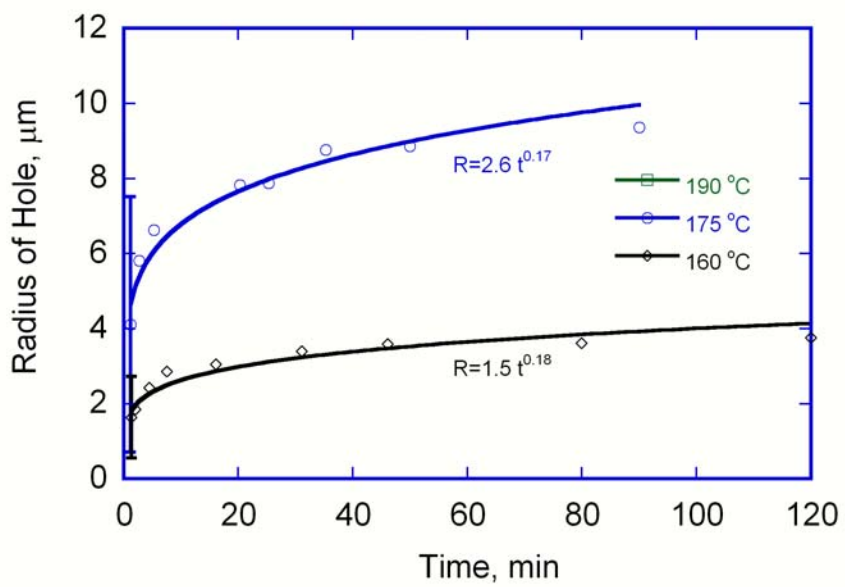

Figure A3.3 Hole growth as function of time for blends with 2 wt% 32-BDMS.

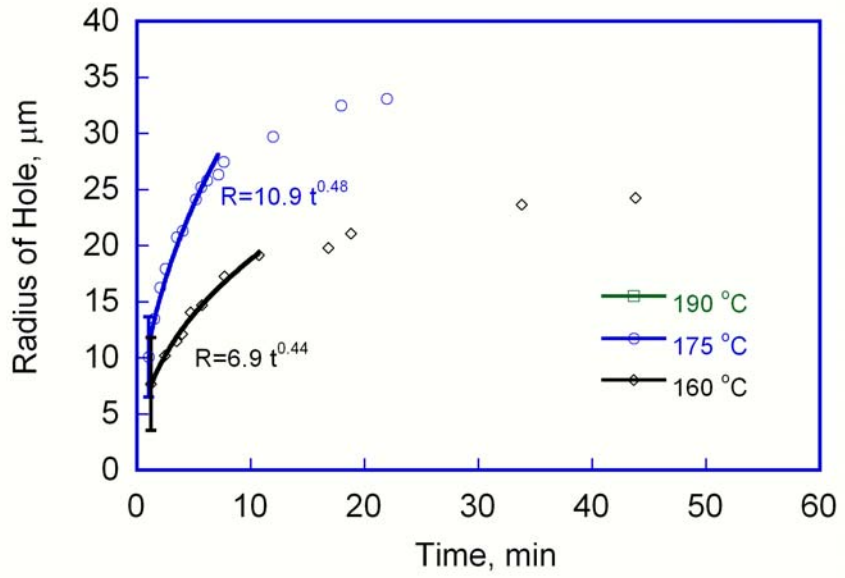

Figure A3.4 Hole growth as function of time for blends with 1 wt% 32-BDMS.

APPENDIX B ADDITIONAL NR DATA

Due to the similarity of the NR profiles of films containing 16-OH, 32-OH and 35-OH to that of 29-OH, the NR profile and its fitting for films containing other nanoparticles are listed in Appendix B (see Table B.1).

Table B.1 NR data listed in Appendix B

Appendix B
Reflectivity profile for films containing 16-OH
Reflectivity profile for films containing 32-OH
Reflectivity profile for films containing 35-OH
Reflectivity profile for films containing 32-BDMS

Reflectivity profiles for films containing 16-OH

Reflectivity profiles for samples with 5 wt% uncrosslinked 16-OH as prepared, annealed 5 min at 140 °C with additional annealing at 175 °C for 5 min are shown in Figure B.1. The overall neutron reflectivity curve in Figure B.1 did not change with additional annealing which indicates there is no much change of the distribution of nanoparticles within the experimental annealing conditions. The dampening of fringes at higher q implies increased roughness at the interfaces.

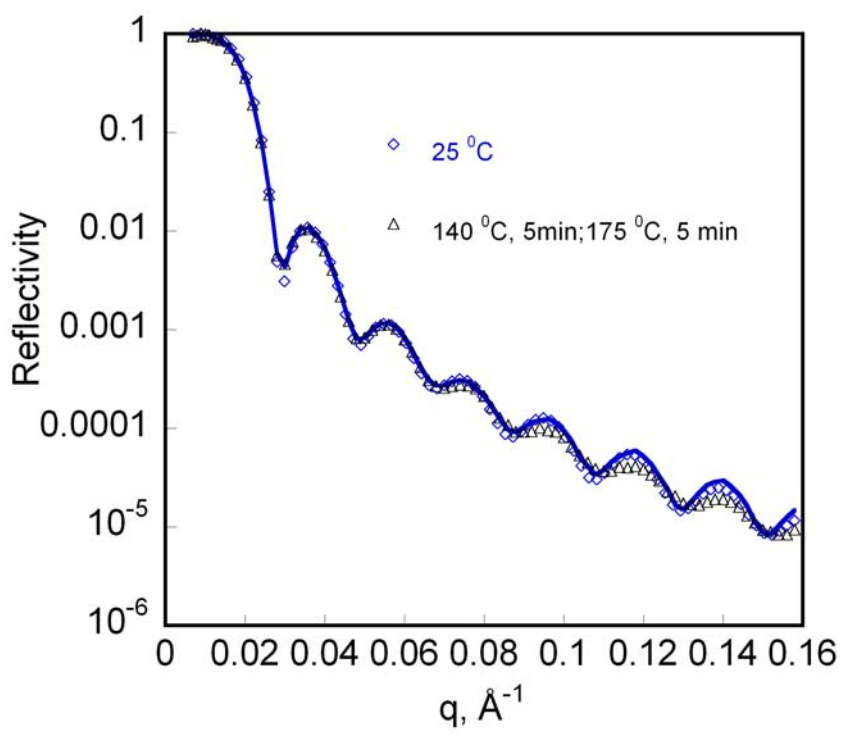

Figure B.1. Neutron reflectivity for PS blends with 5 wt% crosslinked 16-OH under different annealing conditions.

The solid line in Figure B.1 is the fit to the NR data for the as-prepared film which shows a 4.6 nm segregation layer of uncrosslinked 16-OH nanoparticles in thicknesses at Si/SiO surface with the scattering length density profile shown in Figure B.2. The SLD values for deuterated PS (dPS), silicon, silicon oxide are (6.65×10^{-6} Å^{-2}), (2.10×10^{-6}) Å^{-2} and (2.80×10^{-6}) Å^{-2} respectively, and the stars are assumed to have the same scattering length density as PS (1.42×10^{-6} Å^{-2}). The volume fraction in the segregation layer was calculated as ~34% and the segregation percentage was calculated as 100%. This indicates a strong and complete segregation of uncrosslinked 16-OH to the Si/SiO surface during spin casting. No detectable segregation to the polymer/air interface was observed.

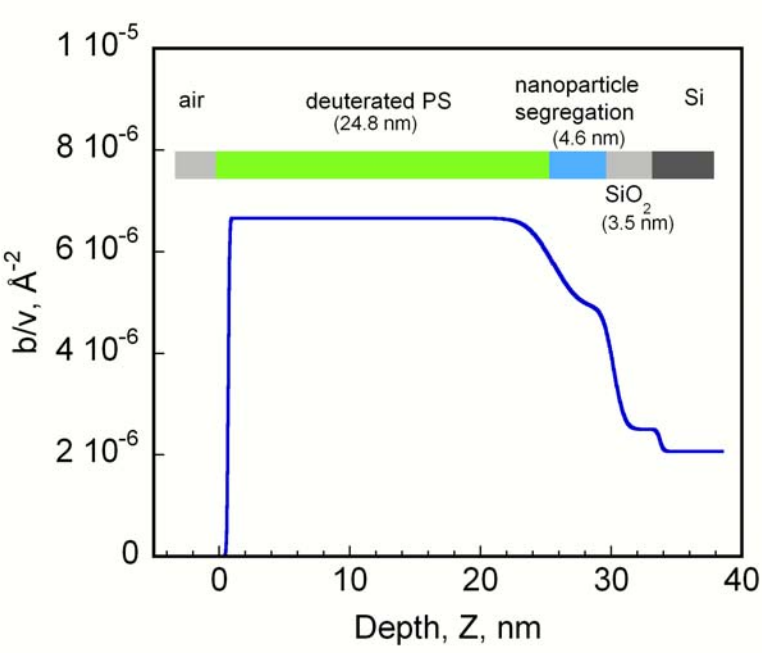

Figure B.2. Scattering length density profile for neutron reflectivity of as-cast PS film (30 nm) with 5 wt% uncrosslinked 16-OH showing a 4.6 nm segregation layer of the star at the Si/polymer interface. There was no detectable segregation to the polymer/air interface.

Reflectivity profiles for films containing 32-OH

Reflectivity profiles for samples with 5 wt% crosslinked 32-OH as prepared, annealed 5 min at 140 °C with additional annealing at 175 °C for 5 min are shown in Figure B.3. The overall neutron reflectivity curve in Figure B.3 did not change with additional annealing which indicates there is no much change of the distribution of nanoparticles within the experimental annealing conditions. The dampening of fringes at higher q implies increased roughness at the interfaces.

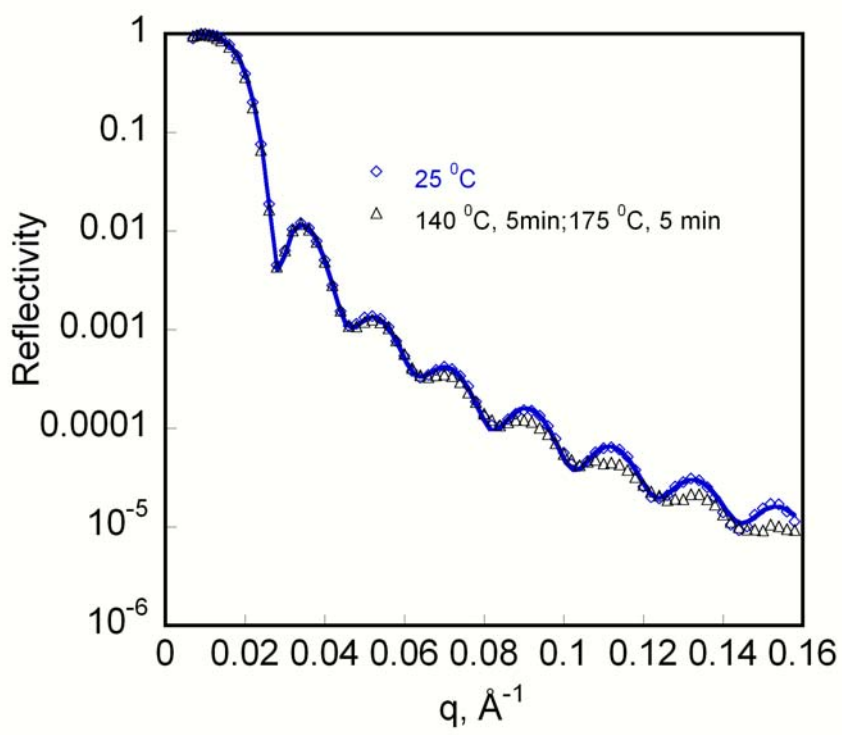

Figure B.3. Neutron reflectivity for PS blends with 5 wt% crosslinked 32-OH under different annealing conditions.

The solid line in Figure B.3 is the fit to the NR data for the as-prepared film which shows a 5.3 nm segregation layer of crosslinked 32-OH nanoparticles in thicknesses at Si/SiO surface with the scattering length density profile shown in Figure B.4. The SLD values for deuterated PS (dPS), silicon, silicon oxide are (6.65×10^{-6} Å^{-2}), (2.10×10^{-6}) Å^{-2} and (2.80×10^{-6}) Å^{-2} respectively, and the stars are assumed to have the same scattering length density as PS (1.42×10^{-6} Å^{-2}). The volume fraction in the segregation layer was calculated as ~33% and the segregation percentage was calculated as 100%. This indicates a strong and complete segregation of crosslinked 32-OH to the Si/SiO surface during spin casting. No detectable segregation to the polymer/air interface was observed.

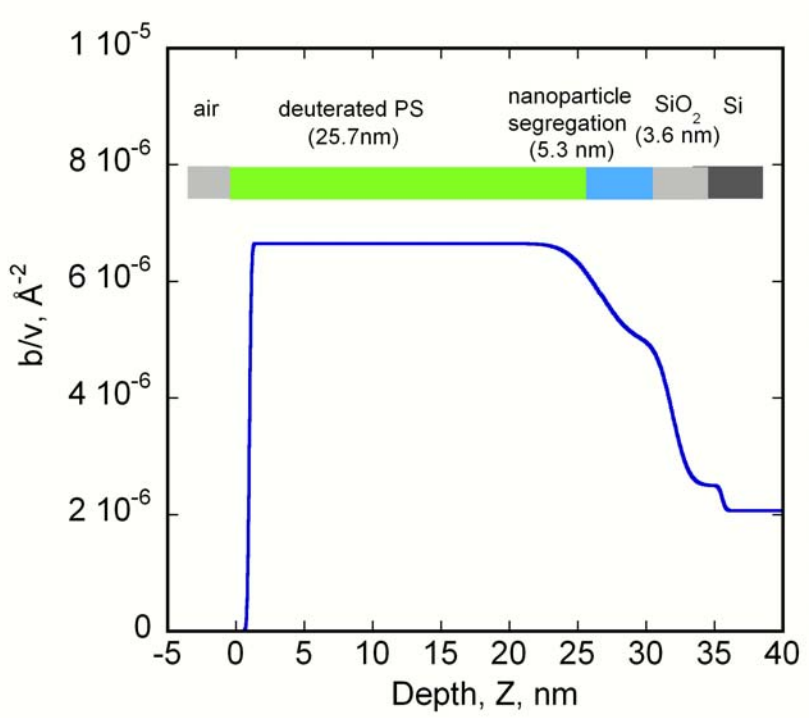

Figure B.4. Scattering length density profile for neutron reflectivity of as-cast PS film (30 nm) with 5 wt% crosslinked 32-OH showing a 5.3 nm segregation layer of the star at the Si/polymer interface. There was no detectable segregation to the polymer/air interface.

Reflectivity profiles for films containing 35-OH

Reflectivity profiles for samples with 5 wt% uncrosslinked 35-OH as prepared, annealed 5 min at 140 °C with additional annealing at 175 °C for 5 min are shown in Figure B.5. The overall neutron reflectivity curve in Figure B.5 did not change much with additional annealing which indicates there is no much change of the distribution of nanoparticles within the experimental annealing conditions. The dampening of fringes at higher q implies increased roughness at the interfaces.

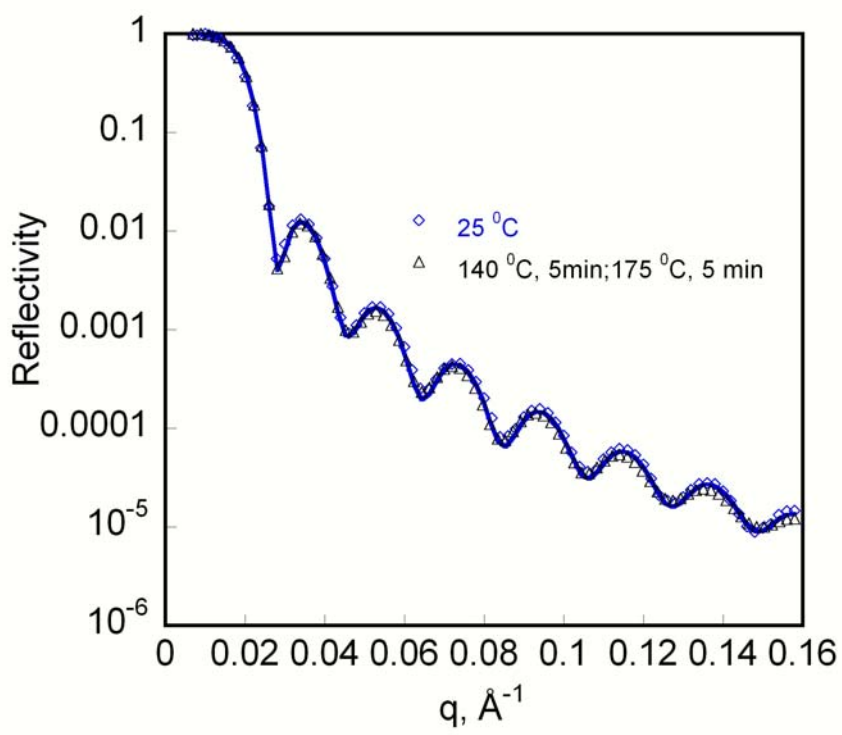

Figure B.5. Neutron reflectivity for PS blends with 5 wt% uncrosslinked 35-OH under different annealing conditions.

The solid line in Figure B.5 is the fit to the NR data for the as-prepared film which shows a 6.2 nm segregation layer of uncrosslinked 35-OH nanoparticles in thicknesses at Si/SiO surface with the scattering length density profile shown in Figure B.6. The SLD values for deuterated PS (dPS), silicon, silicon oxide are (6.65×10^{-6} $Å^{-2}$), (2.10×10^{-6}) $Å^{-2}$ and (2.80×10^{-6}) $Å^{-2}$ respectively, and the stars are assumed to have the same scattering length density as PS (1.42×10^{-6} $Å^{-2}$). The volume fraction in the segregation layer was calculated as ~24% and the segregation percentage was calculated as 91%. This indicates a strong segregation of uncrosslinked 35-OH to the Si/SiO surface during spin casting. No detectable segregation to the polymer/air interface was observed.

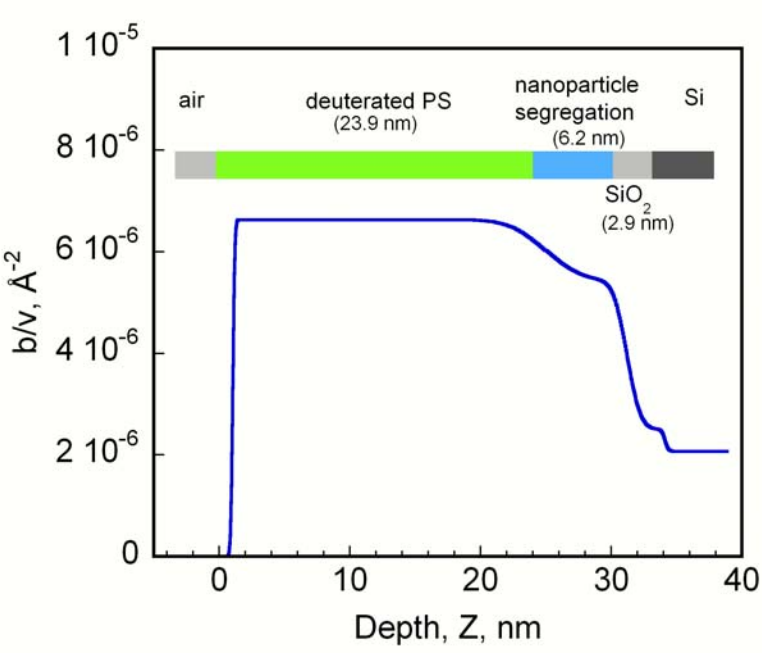

Figure B.6. Scattering length density profile for neutron reflectivity of as-cast PS film (30 nm) with 5 wt% uncrosslinked 35-OH showing a 6.2 nm segregation layer of the star at the Si/polymer interface. There was no detectable segregation to the polymer/air interface.

Reflectivity profiles for films containing 32-BDMS

Reflectivity profiles for samples with 5 wt% crosslinked 32-BDMS as prepared, annealed 5 min at 140 °C with additional annealing at 175 °C for 5 min are shown in Figure B.7. The overall neutron reflectivity curve in Figure B.7 did not change much with additional annealing which indicates there is no much change of the distribution of nanoparticles within the experimental annealing conditions. The dampening of fringes at higher q implies increased roughness at the interfaces.

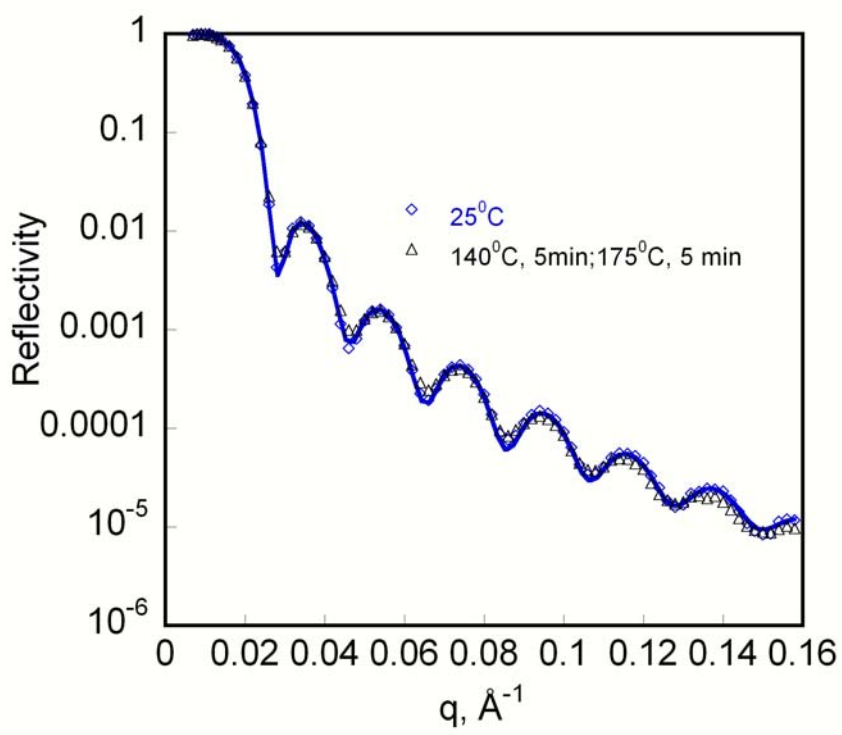

Figure B.7. Neutron reflectivity for PS blends with 5 wt% crosslinked 32-BDMS under different annealing conditions.

The solid line in Figure B.7 is the fit to the NR data for the as-prepared film which shows a 6.2 nm segregation layer of crosslinked 32-BDMS nanoparticles in thicknesses at Si/SiO surface with the scattering length density profile shown in Figure B.8. The SLD values for deuterated PS (dPS), silicon, silicon oxide are (6.65×10^{-6} Å^{-2}), (2.10×10^{-6}) Å^{-2} and (2.80×10^{-6}) Å^{-2} respectively, and the stars are assumed to have the same scattering length density as PS (1.42×10^{-6} Å^{-2}). The volume fraction in the segregation layer was calculated as ~22% and the segregation percentage was calculated as 83%. This indicates a strong of crosslinked 32-BDMS to the Si/SiO surface during spin casting. No detectable segregation to the polymer/air interface was observed.

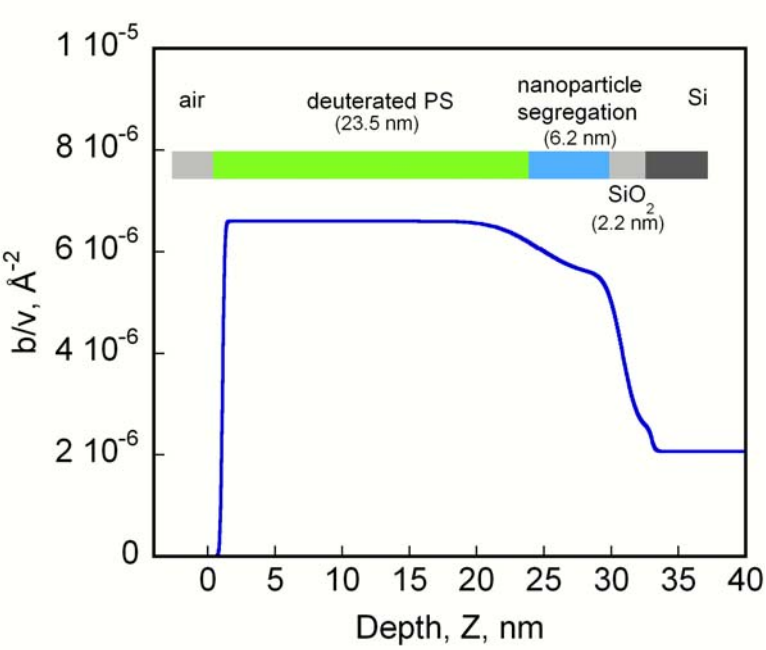

Figure B.8. Scattering length density profile for neutron reflectivity of as-cast PS film (30 nm) with 5 wt% crosslinked 32-BDMS showing a 6.2 nm segregation layer of the star at the Si/polymer interface. There was no detectable segregation to the polymer/air interface.

APPENDIX C ADDITIONAL AFM DATA

Due to the similarity of the AFM data of films containing 35-OH and 32-OH to that of 32-BDMS, the hole morphology for holes in films containing 35-OH and 32-OH are listed in Appendix C (see Table C.1).

Table C.1 AFM data listed in Appendix C

Appendix		Concentration, wt%		
Appendix C1: Hole morphology of films containing 35-OH	160 °C	1	2	5
	175 °C	1	2	5
	190 °C	1	2	5
Appendix C2: Hole morphology of films containing 32-OH	160 °C	1	2	5
	175 °C	1	2	5
	190 °C	1	2	5

Appendix C1 Hole morphology of films containing 35-OH

AFM images of hole morphology in PS films containing 1, 2, 5% 35-OH annealed at 190 °C for 120 min all showed a hole depth of approximately 30 nm (Figure C1.1-3). However, there are still some polymers inside the hole with more for films containing 5% 35-OH than films containing 2 and 1wt% 35-OH.

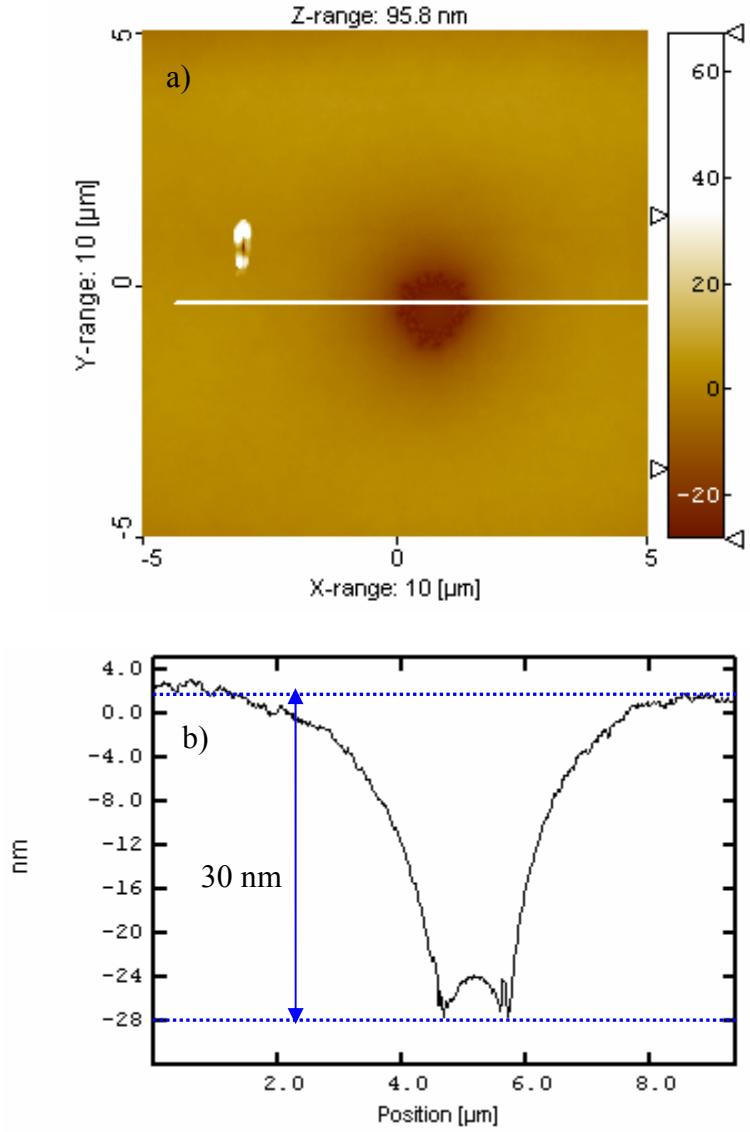

Figure C1.1. a) AFM topography image showing a 2 µm diameter hole in a 30 nm PS film containing 5 wt% of uncrosslinked 35-OH annealed 120 min at 190 °C; **b)** the section analysis of the hole in Figure C1.1a showing hole depth of 30 nm.

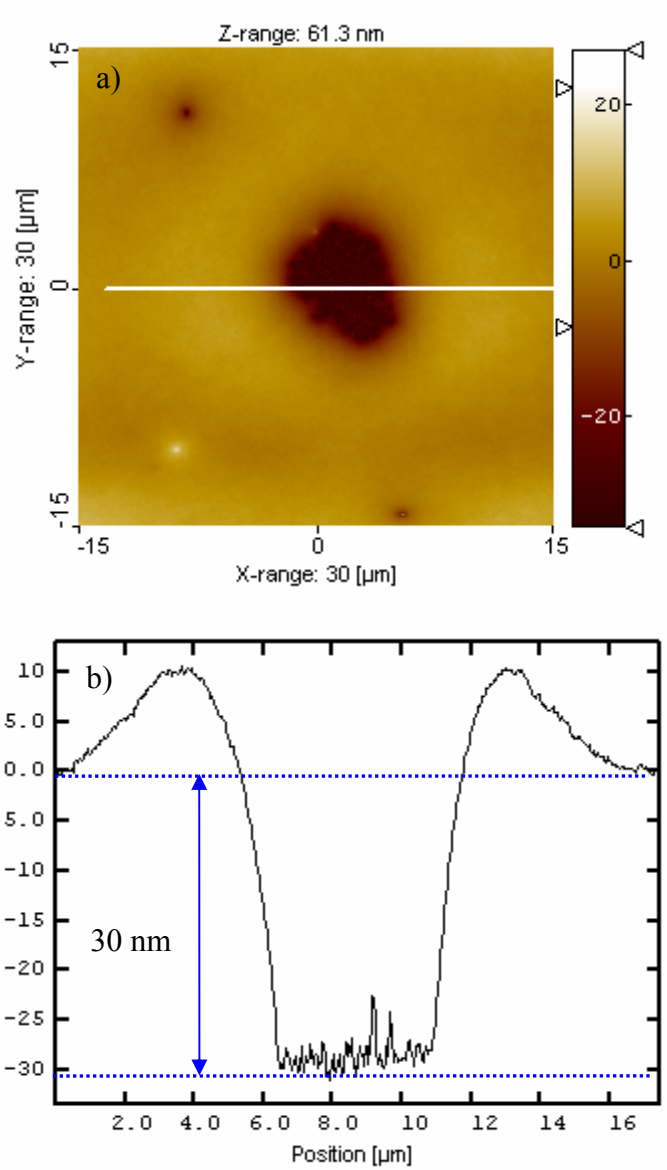

Figure C1.2 a) AFM topography image showing a 5 µm diameter hole in a 30 nm PS film containing 2 wt% of uncrosslinked 35-OH annealed 120 min at 190 °C; **b)** the section analysis of the hole in Figure C1.2a showing hole depth of ~30 nm.

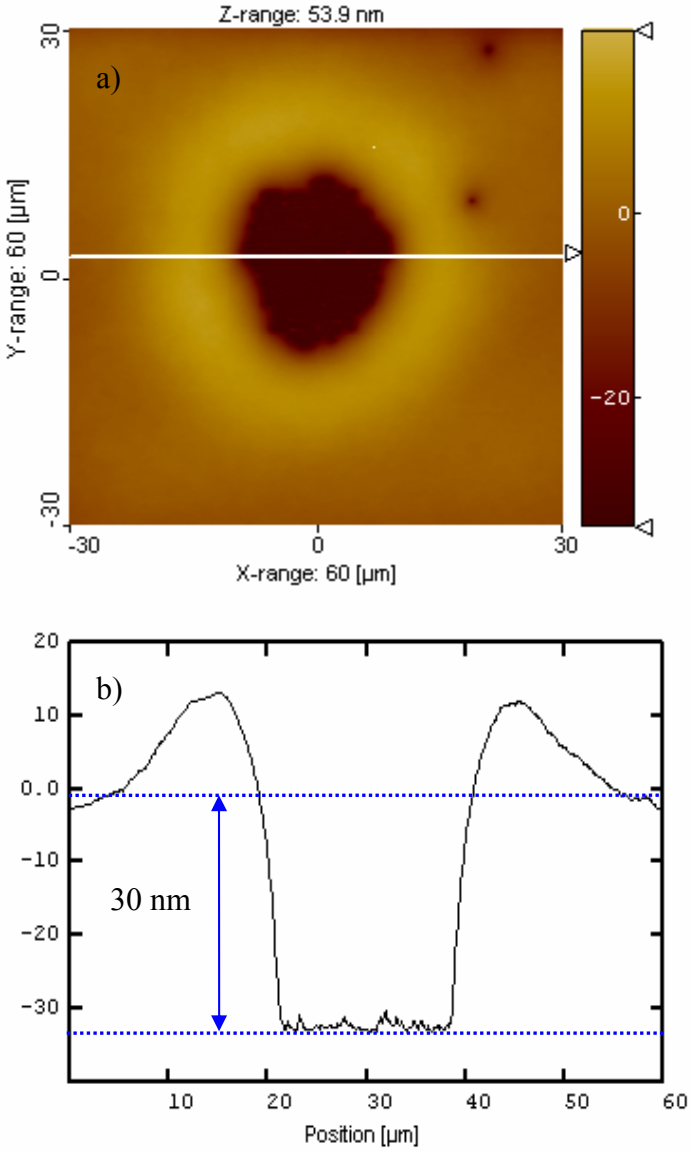

Figure C1.3 a) AFM topography image showing a 18 µm diameter hole in a 30 nm PS film containing 1 wt% of uncrosslinked 35-OH annealed 120 min at 190 °C; **b)** the section analysis of the hole in Figure C1.3a showing hole depth of 30 nm.

Appendix C2 Hole morphology of films containing 32-OH

Figure C2.1a shows a ~40 μm diameter hole in a PS film containing 5% 32-OH annealed at 190°C for 120 min. The section analysis of this hole (Figure C2.1b) shows a hole depth of ~20 nm indicating there is still a ~10 nm layer of polymer on the Si substrate.

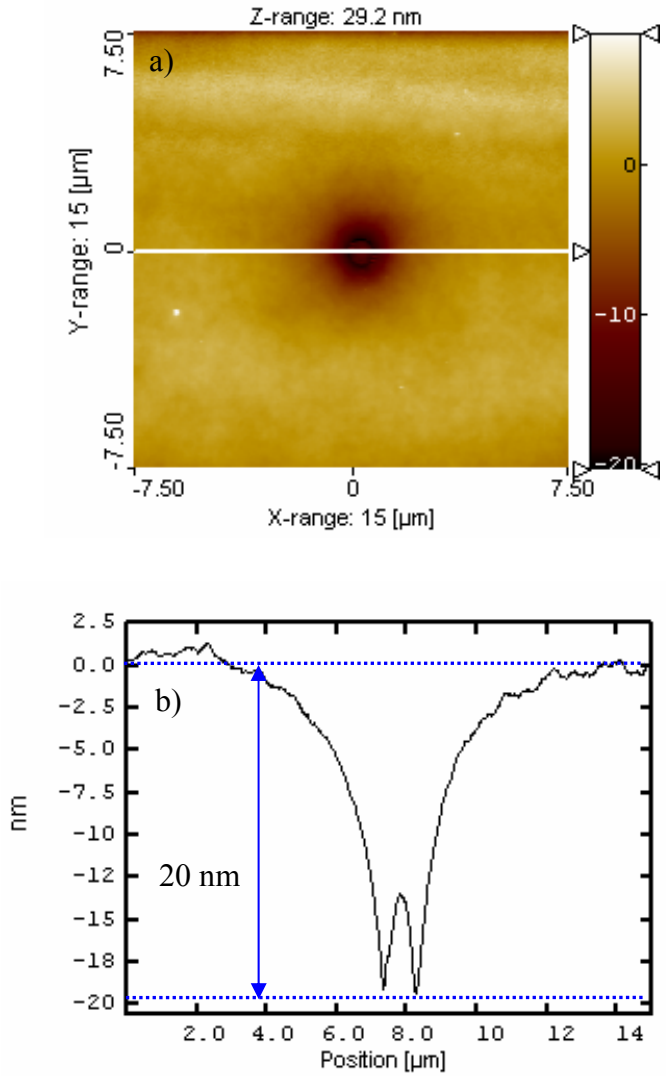

Figure C2.1. a) AFM topography image showing a 2 μm diameter hole in a 30 nm PS film containing 5 wt% of crosslinked 32-OH annealed at 190 °C for 120 min; **b)** the section analysis of the hole in Figure C2.1a showing hole depth of 20 nm and a 10 nm layer of polymer still covering the Si substrate.

This is also an indication of autophobic dewetting behavior and is consistent with the observed different dewetting kinetic from that of pure PS.

The bump inside the hole may be due to the pinning effect of nanoparticles, further annealing the same sample for additional 8 hrs at 190 °C shows the bump inside a hole became flattened as shown in Figure C2.2.

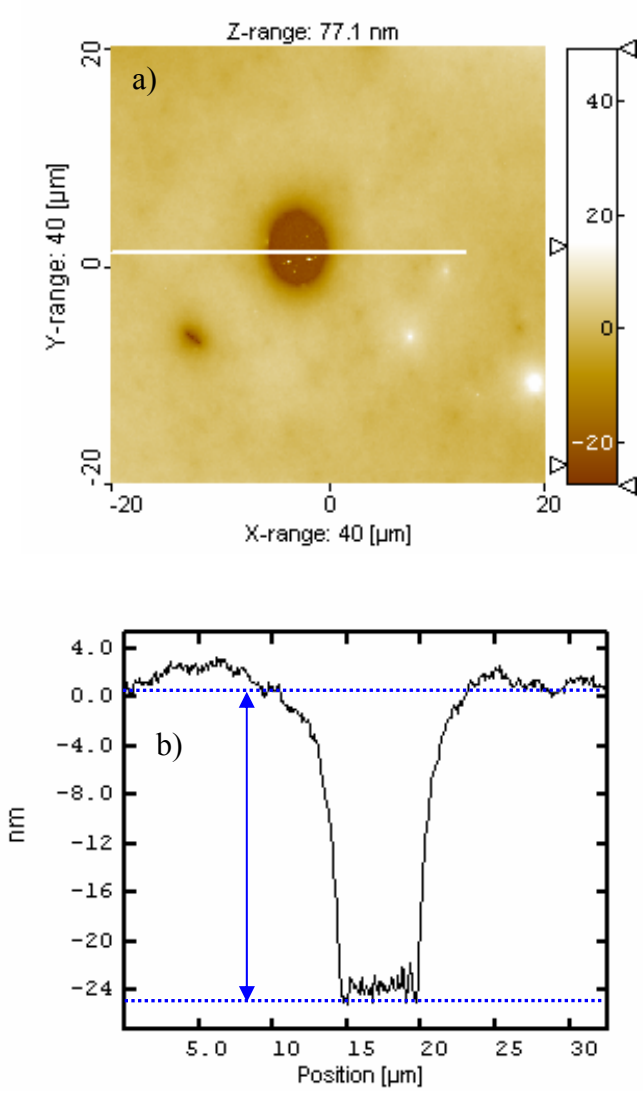

Figure C2.2. a) AFM topography image showing a 5 µm diameter hole in a 30 nm PS film containing 5 wt% of crosslinked 32-OH annealed at 190 °C for 10 hr; **b)** the section analysis of the hole in Figure C2.2a showing hole depth of 26 nm and a 4 nm layer of polymer still covering the Si substrate.

AFM images of hole morphology in PS films containing 2% 32-OH annealed at 190 °C for 120 min also showed there is a layer of star polymer on the Si substrate after dewetting but with much larger size and bigger hole depth (Figure B2.3).

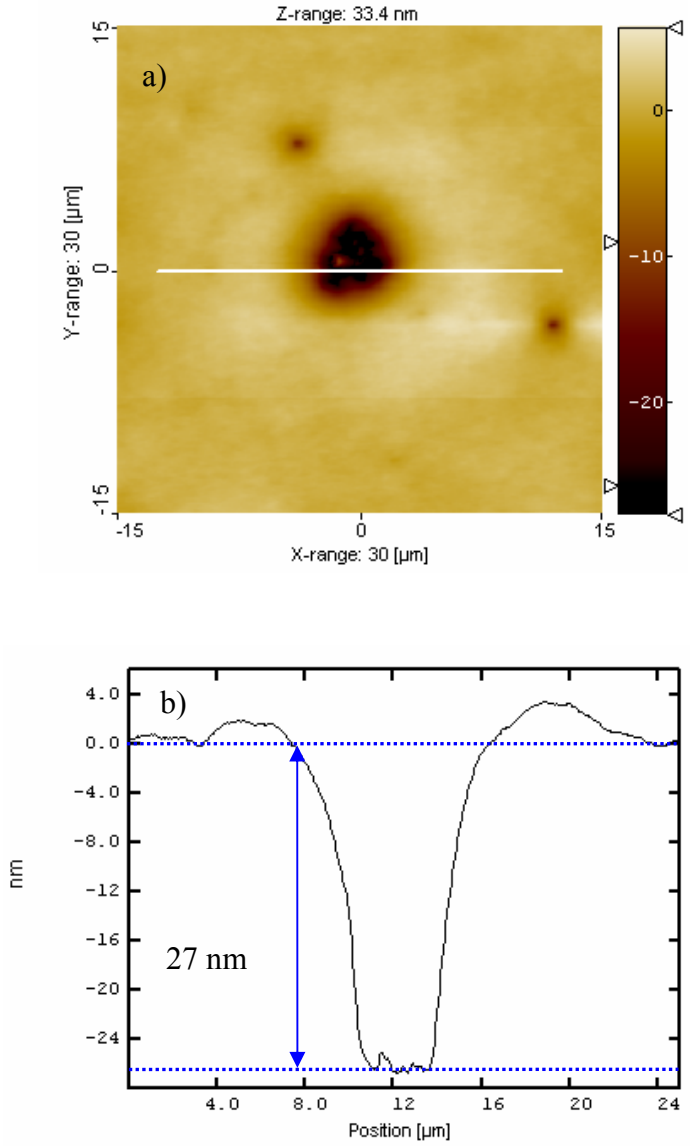

Figure C2.3. a) AFM topography image showing a 7 µm diameter hole in a 30 nm PS film containing 2 wt% of crosslinked 32-OH annealed at 190 °C; **b)** the section analysis of the hole in Figure C2.3a showing hole depth of 27 nm and a 3 nm layer of polymer still covering the Si substrate.

Similar to the hole morphology in pure PS films, holes in PS film containing 1% 32-OH annealed at 190 °C for 120 min show the hole depth is about 30 nm. This indicates the hole goes though to the Si substrate (Figure C2.4 and C2.5) due to less coverage of nanoparticles on Si surface.

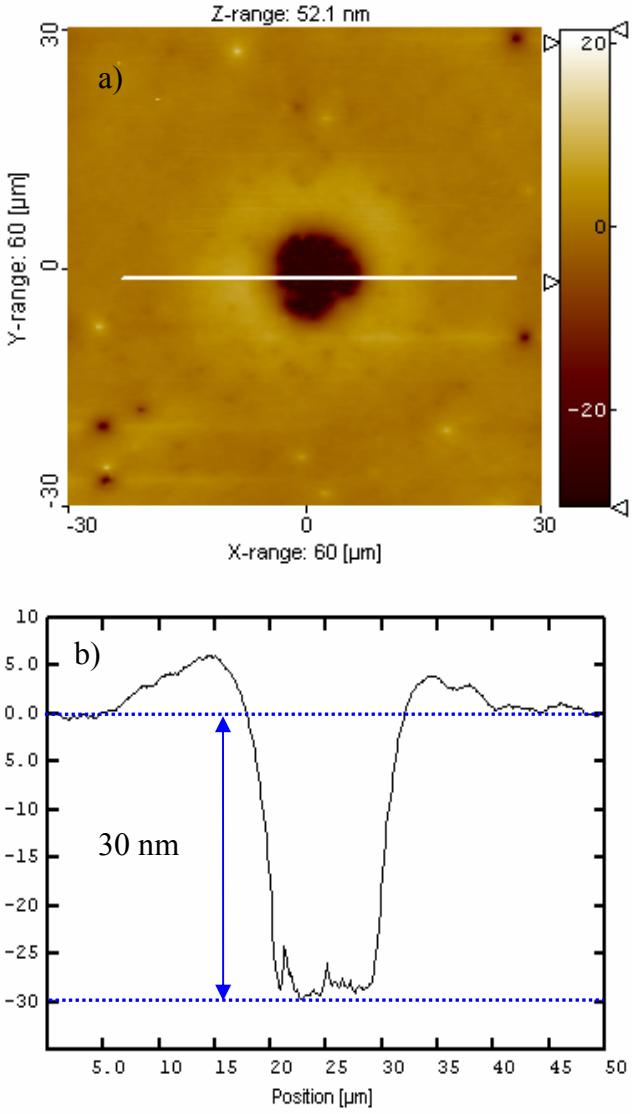

Figure C2.4. a) AFM topography image showing a 12 µm diameter hole in a 30 nm PS film containing 1 wt% of crosslinked 32-OH annealed 120 min at 190 °C; **b)** the section analysis of the hole in Figure C2.4a showing hole depth of 30 nm.

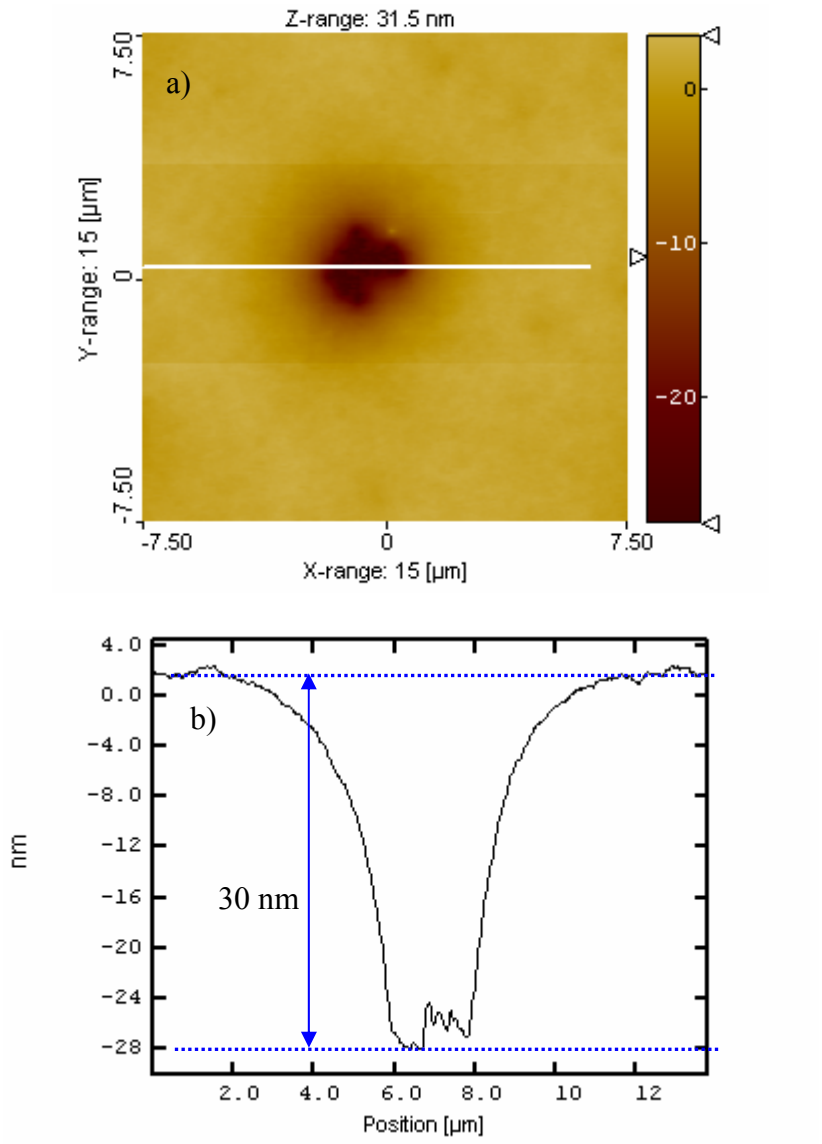

Figure C2.5. a) AFM topography image showing a 3 µm diameter hole in a 30 nm PS film containing 1 wt% of crosslinked 32-OH annealed 120 min at 190 °C; **b)** the section analysis of the hole in Figure C2.5a showing hole depth of 30 nm.

BIBLIOGRAPHY

(1) Tomalia, D. A.; Hedstrand, D. M.; Wilson, L. R. *Encyclopedia of Polymer Science and Engineering*, Index Volume, John Wiley and Sons, New York, 1990

(2) Young, J. R. J.; Lovell, P. A. *Introduction to Polymers*, Chapman and Hall, 1991.

(3) Odian, G. *Principles of Polymerization*, John & Sons, Inc., 1991

(4) Mourey, T. H.; Tuner, S. R.; Rubinstein, M.; Fréchet, J. M. J.; Hawker, C. J.; Wooley, K. L. *Macromolecules*, **1992**, 25, 2401.

(5) Tuner, S. R.; Voit, B. I.; Mourey, T. H. *Macromolecules*, **1993,** 26, 4617.

(6) Gauthier, M.; Li, W.; Tichagwa, L. *Polymer*, **1997**, 38, 6262.

(7) Flory, P. J. *Principles of Polymer Chemistry*, Cornell University Press, New York, 1953

(8) Joel H. Hildebrand, Robert L. Scott, *Regular solutions*, Englewood Cliffs, N.J., Prentice-Hall, 1962

(9) de Gennes, P. G., *Scaling concepts in polymer physics*, Cornell University: New York, 1979.

(10) Boyd, R. H.; Philips, P. J. *The Science of Polymer Molecules*, Cambridge University Press: New York, 1993.

(11) Higgins, J. S. and Benoit, H. C. *Polymers and Neutron Scattering*, Oxford University Press, Inc., New York, 1994.

(12) Roe, R. J. *Methods of X-Ray and Neutron Scattering in Polymer Science*, New York, Oxford, 2000

(13) Sears, V. F. *Neutron News* **1992**, 3, 26.

(14) Russell, T. P., *Mater. Sci. Rep.* **1990**, 5, 171.

(15) Http://www.ncnr.nist.gov.

(16) de Gennes, P. G. *Rev. Mod. Phys.* **1985**, 57, 827.

(17) Israelachvili, J. N. *Intermolecular and surface forces*. London: Academic Press; 1991.

(18) Brochard-Wyart, F.; de Gennes, P.G.; Hervert, H.; Redon, C. *Langmuir* **1994**, 10, 1566.

(19) Redon, C.; Brzoska, J. B.; Brochard-Wyart, F. *Macromolecules* **1994**, 27, 468.

(20) Reiter, G. Unstable Thin Polymer Films: Rupture and Dewetting Process, *Langmuir* **1993**, 9, 1344.

(21) Kerle, T.; Yerushalmi-Rozen, R.; Klein, J.; Fetters, L. J. *Europhys. Lett.* **1998**, 44, 484.

(22) Brochard-Wyart, F.; Dimeglio, J.M.; Quéré, D.; de Gennes, P. G. *Langmuir* **1991**, 7, 335.

(23 Sharma A.; Khanna, R. *Phys. Rev. Lett.* **1998**, 81, 3463.

(24 Sharma A.; Jameel, A. T. *J. Colloid Interface Sci.* **1993**, 161, 190.

(25) Sharma A. and Reiter G., *J. Colloid Interface Sci.* **1996,** 178, 383.

(26) French R. H., *J. Amm. Ceram Soc.* **2000**, 83, 2117.

(27) Mougin K.; Haidara, H. *Europhys. Lett.* **2003**, 61, 660.

(28) Visser J. *Adhesion of colloidal particles*. *In: Matijevic E.(ed), Surface and Colloid Science* John Wiley & Sons, Inc., 3, 1976.

(29) Seemann, R.; Hermingghaus, S.; Jacobs, K. *Phycial Review Letters*, **2001**, 86, 5534.

(30) Reiter, G.; Sharma, A.; Casoli, A.; David, M.-O.; Khanna, R.; Auroy, P. *Langmuir* **1999**, 15, 2551.

(31) Muller-Buschbaum, P., *J. Phys.: Condens. Matter* **2003**, 15, R1549.

(32) Vrij, A., *Faraday Soc.* **1966**, 42, 23.

(33) Brochard-Wyart, F.; Daillant, J. *Can J Phys* **1990**, 68, 1084.

(34) Ruckenstein E.; Jain R. K. *Faraday Trans. II*, **1974**, 70, 132.

(35) Suh, K. Y.; Park, J.; Lee H. H., *J. Chem. Phys.* **2002**,116, 7714.

(36) Konnur, R.; Kargupta, K.; Sharma, A. *Phys. Rev. Lett.*, **2000,** 84, 931.

(37) Jacobs, K.; Herminghaus, S.; Mecke, K.R. *Langmuir* **1998**, 14, 965.

(38) Stange, T. G.; Evans, D. F. *Langmuir* **1997**, 13, 4459.

(39) Neto, C; Jacobs, K. *Physica A* **2004**, 339, 66.

(40) Brochard-Wyart, F.; Debregeas, G.; Fondecave, R.; Martin, P. *Macromolecules* **1997**, 30, 1211

(41) Jacobs, K.; Seemann, R.; Schatz, G.; Herminghaus, S. *Langmuir* **1998**, 14, 4961.

(42) Liu, Y.; Rafailovich, M. H.; Sokolov, J.; Schwarz, S. A.; Zhong, X.; Eisenberg, A.; Kramer, E. J.; Sauer, B. B.; Satija, S. K. *Phys Rev Lett* **1994**;73, 440.

(43) Reiter, G.; Auroy, P.; Auvray, L. *Macromolecules* **1996**, 29, 2150.

(44) Voronov, A.; Shafranska, O. *Langmuir* **2002**, 18, 4471.

(45) Kerle, T.; Yerushalmi-Rozen, R.; Klein, J. *Europhys Lett* **1997**, 38, 207.

(46) Kerle, T.; Yerushalmi-Rozen, R.; Klein, J. *Macromolecules* **1998**, 31, 422.

(47) Henn, G.; Bucknall, D. G.; Stamm, M.; Vanhoorne, P.; Jérôme, R. *Macromolecules*, **1996**, 29, 4305.

(48) Zhao, W; Rafailovich, M. H.; Sokolov, J.; Fetters, L.J.; Plano, R.; Sanyal, M. K.; Sinha, S. K.; Sauer, B. B. *Phys Rev Lett* **1993**, 70, 1453.

(49) Brûlet, A.; Boué, F.; Menelle, A.; Cotton, J. P. *Macromolecules* **2000**, 33, 997.

(50) Jones, R. L.; Kumar, S. K.; Ho, D. L.; Briber, R. M.; Russell, T. P. *Nature* **1999**, 400,146.

(51) Jones, R. L.; Kumar, S. K.; Ho, D. L.; Briber, R. M.; Russell, T. P. *Macromolecules* **2001**, 34, 559.

(52) Kraus, J.; Mu¨ller-Buschbaum, P.; Kuhlmann, T.; Schubert, D. W.; Stamm, M. *Europhysics Letters* **2000**, 49, 210.

(53) Shuto, K., Oishi, Y.; Kajiyama, T. *Polymer* **1995**, 36, 549.

(54) Yerushalmi-Rozen, R.; Kerle, T.; Klein, J. *Science* **1999**, 285,1254.

(55) de Crevoisier, G.; Fabre, P.; Corpart, J-M.; Leibler, L. *Science* **1999**, 285, 1246. See also Russell T.P.; Kim H. C. *Science* **1999**, 285, 1219.

(56) Yerushalmi-Rozen, R.; Klein, J.; Fetters, L. J., *Science* **1994**, 263, 793.

(57) Feng, Y; Karim, A; Weiss, R. A.; Douglas, J. F.; Han, C. C. *Macromolecules* **1998**, 31, 484.

(58) Barnes, K. A.; Karim, A.; Douglas, J. F.; Nakatani, A. I.; Gruell, H.; Amis, E. J., *Macromolecules* **2000**, 33, 4177.

(59) Mackay, M. E.; Hong. S.; Russell, T. P.; Hawker, C. J.; Vestberg, R.; Douglas, J. F., *Langmuir* **2002**, 18, 1877.

(60) IUPAC, *Pure and Applied Chemistry* **1996**, 68, 2287.

(61) Huber, K.; Burchard, W.; Fetters, L. J. *Macormolecules* **1984**, 17, 541.

(62) Richter, D.; Stuhn, B.; Ewen, B.; Nerger, D. *Phys. Rev. Lett.* **1987**, 58, 2462.

(63 Richter, D.; Farago, B.; Huang, J. S.; Fetters, L. J.; Ewen, B. *Macromolecules* **1989**, 22, 468.

(64) Bauer, B.; Fetters, L. J.; Graessley, W.; Hadjichristidis, N.; Quack, G. *Macromolecules* **1989**, 22, 2337.

(65) Boothroyd, A. T.; Squires, G. L.; Fetters, L. J.; Rennie, A. R.; Horton, J. C.; de Vallera, A. M. B. G. *Macromolecules* **1989**, 22, 3130.

(66) Daoud, M.; Cotton, J. P. *Journal de Physique* **1982**, 43, 531.

(67) Burchard, W. *Adv. Poly. Sci.* **1983**, 48, 1.

(68) Whittington, S. G.; Lipson, J .E.G.; Wilkinson, M. K.; Gaunt, D. S. *Macromolecules* **1986**, 19, 1241.

(69) Freire, J. J.; Pla, J., Rey, A.; Prats, R. *Macromolecules*, **1986**, 19, 452.

(70) Grest, G.; Kremer, K.; Witten T. A. *Macromolecules* **1987**, 20, 1376.

(71) Batoulis, J.; Kremer, K. *Macromolecules* **1989**, 22, 4277.

(72 Croxton, C. *Macromolecules* **1988**, 21, 2269.

(73) Miyake, A.; Freed, K. F. *Macromolecules* **1983**, 16, 1228.

(74) Sogah, D. Y.; Hertler, W. R.; Webster, O. W.; Cohen, G. M. *Macromolecules* **1987**, 20, 1473.

(75) Zilliox, J. G.; Decker, D.; Rempp, P. *C. R. Hebd. Séances Acad. Sci., Ser. C* **1966**, 262, 726.

(76) Worsfold, D. J.; Zilliox, J. G.; Rempp, P. *Can. J. Chem.* **1969**, 47, 3379.

(77 Zilliox, J. G. *Makromol. Chem*. **1972**, 156, 121.

(78) Young, R. N.; Fetters, L. J. *Macromolecules* **1978**, 11, 899.

(79) Eschwey, H.; Hallensleben, M. L.; Burchard, W. *Makromol. Chem.* **1973**, 173, 235.

(80) Eschwey, H.; Burchard, W. *Polymer* **1975**, 16,180.

(81 Tsitsilians, C.; Chaumont, P.; Rempp, P. *Makromol. Chem.* **1990**,191, 2319.

(82) Tsitsilians, C.; Graff, S.; Rempp, P. *Eur. Polym. J.* **1991**, 27, 243.

(83) Martin, N.;Seone, C.; Hanack, M. *Org. Prepr. Znt.* **1991**, 23, 237.

(84) Harth, E.; Van Horn, B.; Lee, V. Y.; Germack, D. S.; Gonzales, C. P.; Miller, R. D.; Hawker, C. J. *J. Am. Chem. Soc.*, **2002**, 124, 8653.

(85 Daoud, M.; Cotton, J. P. *J. Phys.* **1982**, 43, 531.

(86) Berne, B.J.; Pecora, R. *Dynamic Light Scattering with Applications to Chemistry, Biology, and Physics*; Wiley Interscience: New York, 1976; 376.

(87 Burchard, W. *Adv. Polym. Sci.* **1999**, 143, 113.

(88)Tande, B. M.; Wagner, N. J.; Mackay, M. E.; Hawker, C. J.; Jeong, M. *Macromolecules* **2001**, 34, 8580.

(89) Roovers, J.; Martin J. E. *Journal of Polymer Science: Part B-Polymer Physics* **1989**, 27, 2513.

(90) Yamakawa, H. *Modern Theory of Polymer Solutions*; Harper and Row: New York, 1971.

(91) Ishizu, K.; Ono, T.; Uchida, S. *Macromolecular Chemistry and Physics* **1997**, 198, 3255.

(92) Sakurai, S.; Hasegawa, H.; Hashimoto, T.; Han, C. C. *Polym. Comm.* **1990**, 31, 99.

(93) Maconnachie, A.; Kambour, R. P.; White, D. M.; Rostami, S.; Walsh, D. J. *Macromolecules*, **1984**, 17, 2645.

(94) Guinier, A.; Fournet, G. *Small Angle Scattering of X-rays*; Wiley: New York, 1955.

(95) Guinier, A. *X-ray diffraction*; W. H. Freeman and Company: San Francisco, 1963

(96) Choi S.; Briber R. M.; Bauer B. J.; Topp A.; Gauthier M.; Tichagwa L. *Macromolecules* **1999**, 32, 7879.

(97) Strazielle, C.; Benoit, H. *Macromolecules* **1975**, 8, 203.

(98) Willner, L.; Jucknischke, O.; Richter, D., Roovers, J.; Zhou, L. L.; Toporowski, P.M.; Fetters, L. J.; Huang, J. S.; Lin, M. Y.; Hadjichristidis, N. *Macromolecules* **1994**, 27, 3821.

(99) Trollsas, M.; Atthof, B.; Würsch, A.; Hedrick, J. L.; Pople, J. A.; Gast, A. P. *Macromolecules* **2000**, 33, 6423.

(100) Antonietti, M; Bremser, W.; Schmit, M. *Macromolecules* **1990**, 23, 3796.

(101) Roovers J.; Zhou L. L.; Toporowski P. M.; Vanderzwan M.; Iatrou H. *Macromolecules* **1993,** 26, 4324.

(102) Roovers, J. *Macromol. Symp.* **1997**, 121, 89.

(103) Richter, D.; Jucknischke, O.; Willner, L.; Fetters, L. J.; Lin, M.; Huang, J. S.; Roovers, J.; Toporowski, C.; Zhou, L. L. *J. Phys. (Paris),* **1993**, 3, 3.

(104) Owens, D. K. *Journal of Applied Polymer Science* **1969**, 13, 1741.

(105) Wu, S. *J. Polymer. Sci.: Part C* **1971**, 34, 19-30.

(106) Fowkes, F. M. *Ind. Engr. Chem.*, **1964**, 56, 40.

(107) Sakurai, S.; Hasegawa, H.; Hashimoto, T.; Hargis, I. G.; Aggarwal, S. L.; C. C. Han. *Macromolecules* 1990, **23**, 451.

(108) Sakurai, S.; Jinnai, H.; Hasegawa, H.; Hashimoto, T.; Han, C. C. *Macromolecules* **1991**, 24**,** 4839.

(109) Rhee, J.; Crist, B. *Macromolecules* **1991**, 24, 5663.

(110) Beaucage, G.; Stein, R. S.; Hashimoto, T.; Hasegawa, H. *Macromolecules* **1991**, 24, 3443.

(111) Graessley, W. W.; Krishnamoorti, R.; Balsara, N.; Fetters, L. J.; Lohse, D. J.; Schulz D. N.; Sissano. J. A. *Macromolecules* **1993**, 26, 1137.

(112) Fredrickson, G. H.; Liu, A.; Bates, F. S. *Macromolecules* **1994**, 27, 2503.

(113) Garas G.; Kosmas. M. *Macromolecules* **1994**, 27, 6671.

(114) Gujrati. P. D. *J Chem Phys* **1998**, 108, 5104.

(115) Faust, A. B.; Sremcieh, P. S.; Gilmer, J. W.; Mays. J. W. *Macromolecules* **1989**, 22, 1250

(116) Russell, T. P.; Fetters, L. J.; Clark, J. C.; Bauer, B. J.; Han. C. C. *Macromolecules* **1990**, 23, 654.

(117) van Aert, H. A. M.; van Genderen M. H. P.; Meijer. E. W. *Polym Bull* **1996**, 37, 273.

(118) Greenberg, C. C.; Foster, M. D.; Turner, C. M.; Corona-Galvan, S.; Cloutet, E.; Butler, P. D.; Hammouda, B.; Quirk, R. P. **1999**, 40, 4713.

(119) Bauer, B. J.; Briber, R. M.; Han, C. C. *Macromolecules*, **1989**, 22, 940-948.

(120) Benoit, H. *Journal of Polymer Science*, **1953**, 11, 507.

(121) Alessandrini, J. L.; Carignano, M. A. *Macromolecules* **1992**, 25, 1157.

(122) Dozier, D. W.; Huang, J. S.; Fetters, L. J. *Macromolecules* **1991**, 24, 2810.

(123 Joanny J. F., *Comptes Rendus Hebdomadaires des Seances de l Acad. des Sci. Ser. B*, **1978**, 286, 89-91

(124) Wu, D. T.; Fredrickson, G. H. *Macromolecules* **1996**, 29, 7919.

(125) Debye, P. *Journal of Physical and Colloid Chemistry* **1947**, 51, 18.

(126) Londono, J. D.; Narten, A. H.; Wignall, G. D.; Honnell, K. G.; Hsieh, E. T.; Johnson, T. W.; Bates, F. S. *Macromolecules* **1994**, 27, 2864.

(127) Adamson, A. W. *Physical Chemistry of Surfaces*, 4th ed.; John Wiley & Sons: New York, 1982; Chapter 3.

(128) Thomas, H. R.; O'Malley, J. J. *Macromolecules* **1981**, 14, 1316.

(129) Pan, D. H.; Prest, W. M. *J. Appl. Phys.* **1985**, 58, 2861.

(130) Schmitt, R. L.; Gardella, J. A., Jr.; Salvati, L., Jr. *Macromolecules* **1986**, 19, 648.

(131) Bhatia, Q. S.; Pan, D. H.; Koberstein, J. T. *Macromolecules* **1988**, 21, 2166.

(132 Schmidt, J. J.; Gardella, J. A., Jr.; Salvati, L., Jr. *Macromolecules* **1989**, 22, 4489.

(133) Yethiraj, A. *Phys. Rev. Lett.* **1995**, 74, 2018.

(134) Freed, K. F. *Journal of Chemical Physics* **1996**, 105, 10572.

(135) Sikka, M.; Singh, N.; Karim, A.; Bates, F. S.; Satija, S. K.; Majkrzak, C. F. *Phys. Rev. Lett.* **1993**, 70, 307.

(136) Donley, J. P.; Wu, D. T.; Fredrickson, G. H. *Macromolecules* **1997**, 30, 2167.

(137) Wu, D. T.; Fredrickson, G. H.; Carton, J. P. *J. Chem. Phys.* **1996**, 104, 6387.

(138) Yethiraj, A.; Kumar, S. K.; Hariharan, A.; Schweizer, K. S. *J. Chem. Phys.* **1994**, 100, 4691.

(139) Kumar, S. K.; Yethiraj, A.; Schweizer, K. S.; Leermakers, A. M. *J. Chem. Phys*. **1995**, 103, 10332.

(140) Carignano, M. A.; Szleifer, I. *Europhys. Lett.* **1995**, 30, 525.

(141) Hariharan, A.; Kumar, S. K.; Russell, T. P. *J. Chem. Phys.* **1993**, 98, 4163.

(142) Tanaka, K.; Kajiyama, T.; Takahara, A.; Tasaki, S. *Macromolecules* **2002**, 35, 4702.

(143) Hariharan, A.; Kumar, S. K.; Russell, T. P. *J. Chem. Phys.* **1993**, 99, 4041.

(144) Jones, R. A. L.; Richards, R. W. *Polymers at Surfaces and Interfaces*; Oxford University Press: London, 1995.

(145) Zhao, W.; Zhao, X.; Rafailovich, M. H.; Sokolov, J.; Composto, R. J.; Smith, S. D.; Satkowski, M.; Russell, T. P.; Dozier, W. D.; Mansfield, T. *Macromolecules* **1993**, 26, 561.

(146) Elman, J. F.; Johs, B. D.; Long, T. E.; Koberstein, J. T. *Macromolecules* **1994**, 27, 5341.

(147) Tanaka, K.; Kawaguchi, D.; Yokoe, Y.; Kajiyama, T.; Takahara, A.; Tasaki, S. *Polymer* **2003**, 44, 4171.

(148) Foster, M. D.; Greenberg, C. C.; Teale, D. M.; Turner, C. M.; Corona-Galvan, S.; Cloutet, E.; Butler, P. D.; Hammouda, B.; Quirk, R. P. *Macromolecular Symposia* **2000**, 149, 263.

(149) http://www.ncnr.nist.gov/programs/reflect/data_reduction/software/index.html.

(150) http://physics.nist.gov/Divisions/Div846/Gp3/NIOF/polysty.html.

(151) Freed, K. F.; Pesci, A. I. *Macromolecules* **1989**, 22, 4048.

(152) Genzer, J.; Composto, R. J. *Europhysics Letters* **1997**, 38, 171.

(153) Flebbe, T.; Dunweg, B.; Binder, K. *Journal de Physique II* **1996**, 6, 665.

(154) Zhao, X.; Zhao, W.; Sokolov, J.; Rafailovich, M. H.; Schwarz, S. A.; Wilkens, B. J.; Jones, R. A. L.; Kramer, E. J. *Macromolecules* **1991**, 24, 5991.

(155) Jones, R. A. L.; Kramer, E. J.; Sokolov, J.; Rafailovich, M. H.; Schwarz, S. A. *Phys. Rev. Lett.* **1989**, 62, 280.

(156) Sheiko, S. S.; Gauthier, M.; Moller, M. *Macromolecules* **1997**, 30, 2343.

(157) Krishnamoorti, R.; Ren, J.; Silva, A. S. *J. Chem. Phys.* **2001**, 114, 4968.

(158) Ferry, J. D., *Viscoelastic Properties of Polymers*, 3rd ed. Wiley, New York, 1980.

(159) Einstein, A. *Ann. Phys. (Leipz.)* **1906**, 19, 371.

(160) Mackay, M. E.; Dao, T. T.; Tuteja, A.; Ho, D. L.; Horn, B. V.; Kim, H-C; Hawker, C. J. *Nature Materials* **2003**, 2, 762.

(161) Kharchenko, S. B. ; Kannan, R. M. *Macromolecules* **2003**, 36, 407.

(162)Varnik, F.; Baschnagel, J.; Binder, K. Phys. Rev. E., **2002**, 65, 021507.

(163) Wenzel, R. N. *J. Phys. Colloid Chem.* **1949**, 53, 1466.

(164) Kerle, T.; Yerushalmi-Rozen, R.; Klein, J. *Europhys. Lett.,* **1997**, 38, 207.

(165) Netz, R. R.; Andelman, D. *Physical Review E*, **1997**, 55, 687.

(166) Wasan, D. T.; Nikolov, A. D. *Nature* **2003**, 423, 156.

(167) Chaudhury, M. K. *Nature* **2003**, 423, 131.

(168) Horn, R. G.; Israelachvili, J. N. *Chem. Phys. Lett* **1980**, 71, 192.

(169) Kralchevsky, P. A.; Denkov, N. D. *Chem. Phys. Letters* **1995**, 240, 385.

(170) Marinova, K. G.; Gurkov, T. D. ; Dimitrova, T. D. ; Alargova, R. G. ; Smith, D. *Langmuir* **1998**, 14, 2011-2019.

(171) Chu, X. L.; Nikolov, A. D.; Wasan, D. T. *Langmuir* **1994**, 10, 4403.

(172) Wallace, W. E.; Fischer, D. A.; Efimenko, K.; Wu, W. L.; Genzer, J. *Macromolecules* **2001**, 34, 5081.

(173) de Gennes, P. G. ; *Eur. Phys. J. E.* **2000**, 12, 201.

(174) Lin, E. K.; Kolb, R.; Satija, S.; Wu, W. *Macromolecules* **1999**, 32, 3753.

(175) Mansfield, K. F.; Theodorou, D. N. *Macromolecules* **1991**, 24, 6283.

(176) Baschnagel, J.; Binder, K. *Macromolecules* **1995**, 28, 6808.

(177) Torres, J. A.; Nealy, P. F.; de Pablo, J. J. *Phys. Rev. Lett.* **2001**, 85, 3221.

(178) Lin, E. K.; Wu, W.; Satija, S. *Macromolecules* **1997**, 30, 7224.

(179) Pham J. Q.; Green, P. F. *Journal of Chemical Physics* **2002**,116, 5801.

(180) Keddie, J. L.; Jones, R. A.; Cory, R. A. *Faraday Discuss.* **1994**, 98, 219

(181) van Zanten, J. H.; Wallace, W. E.; Wu, W. *Phys. Rev. E* **1996**, 53, R2053.

(182) Torres, J. A.; Nealy, P. F.; de Pablo J. J. *Phy. Rev. Lett.* **2001,** 85, 3221.

(183) Forrest, J. A.; Dalnoki-Veress, K.; Stevens, J. R.; Dutcher, J. R. *Phys. Rev. Lett.* **1996,** 77, 2002.

(184) Forrest, J. A.; Mattsson, *J. Phys. Rev. E*, **2000,** 61, R53.